Title
The Interface Energy and Particle Size Effects on Nanocomposites

Author
Zhu, Yinghui

Publication Date
2019

Peer reviewed|Thesis/dissertation

UNIVERSITY OF CALIFORNIA

Los Angeles

The Interface Energy and Particle Size Effects on Nanocomposites

A dissertation submitted in partial satisfaction of the

requirements for the degree Doctor of Philosophy

in Civil Engineering

by

Yinghui Zhu

2019

ABSTRACT OF THE DISSERTATION

The Interface Energy and Particle Size Effects on Nanocomposites

by

Yinghui Zhu

Doctor of Philosophy in Civil Engineering

University of California, Los Angeles, 2019

Professor Jiann-Wen Ju, Chair

Currently, the advancement of nanotechnology provides new insights into the structures with the characteristic length in the nanometer scale. Due to their large specific area, the nano-structures may possess desirable features. Therefore, scientists attempt to employ the nano-structures as the reinforcements in the composite materials; i.e., nanocomposites, to achieve improved properties. It is well known that the local atomic environment at the matrix-reinforcement interface is different from its setting associated with the interior due to the accommodation of two different materials. As a consequence, the free energy associated with the interface is different from that associated with the interior. Since the nanocomposites have much larger interface area than the traditional

composites, the interface energy effect becomes one of the main factors that determine the mechanical properties. The objective of the present study is to research on the effective (overall) elastic, elastoplastic and elastoplastic damage behavior of nanocomposites by considering the interface energy effect. Firstly, a nanomechanical framework is proposed in Chapter 3 to investigate the effective elastic behavior of nanocomposites containing randomly distributed spherical particles. The interface energy effect is simulated by the zero-thickness membrane interphase between the matrix and the reinforcement together with the interface stress. In addition, classical micromechanical homogenization procedures are incorporated to determine the volume averaged effective properties. Secondly, the elastic nanomechanical framework in Chapter 3 is extended to consider the more sophisticated spheroidal particle reinforced nanocomposites in Chapter 4. The spheroidal particles are assumed to be aligned and randomly distributed in the matrix. Thirdly, the effective elastoplastic behavior of the spherical particle reinforced nanocomposite is studied in Chapter 5. The effective secant moduli are obtained for the nanocomposite with the elastoplastic matrix and the elastic reinforcements. In Chapter 6, the elastoplastic damage performance of the continuous fiber reinforced nanocomposites is investigated. Interface debonding is considered as the damage type that occurs in the nanocomposites. The progressive debonding of the interface and the volume fraction evolution of debonded fibers are presented. The results show that the effective mechanical properties of nanocomposites are dependent upon the total interface area. The interface energy effect increases with the rising total interface area in the composite and becomes negligible when the dimensions

of the reinforcements are in micrometer scale. Further, classical micromechanical solutions can be obtained when the interface energy effect is neglected.

The dissertation of Yinghui Zhu is approved.

Ertugrul Taciroglu

Jian Zhang

Ajit K. Mal

Jiann-Wen Ju, Committee Chair

University of California, Los Angeles

2019

TABLE OF CONTENTS

LIST OF FIGURES

Chapter 1

Chapter 2

Chapter 3

Chapter 4

Chapter 5

Chapter 6

LIST OF TABLES

Acknowledgments

First of all, I would like to express my gratitude to all who kindly gave me the opportunity to work on this doctoral research. The first person to thank is my academic advisor, Prof. Jiann-Wen Woody Ju, whose continuous support, stimulating suggestions and encouragement helped me during the time of my research and life. Thanks are also given to Prof. Ertugrul Taciroglu, Prof. Jian Zhang in the Civil and Environmental Engineering Department, and Prof. Ajit Mal from the Mechanical and Aerospace Engineering Department for serving on my Ph.D. dissertation committee. Each of the committee members has provided me extensive professional guidance and educated me substantially on scientific research.

I am also grateful to all of those with whom I have had the pleasure to work during these years. I would never forget their assistance and all enjoyable times during the research and the daily life in UCLA. Certainly, there are countless people whose advice and guidance helped to shape who and what I am today.

No one has been more important to me during the pursuit of the Ph.D. degree than my family members. I am deeply indebted to my parents for their great support and devotion. Their love and guidance are always with me in whatever I do. Most importantly, I would like to express my deepest gratitude to my wife, Edith, and my son, Lucas. Without their endless love, encouragement and dedication, my doctoral study at UCLA would not have ever come true.

VITA

09/2009-06/2013	B.S., Department of Mechanics and Engineering Southwest Jiaotong University, Chengdu, China
09/2013-06/2014	M.S., Department of Civil & Environmental Engineering University of California, Los Angeles, Los Angeles, USA
09/2014-11/2019	Graduate Student Researcher, Teaching Asistant Department of Civil & Environmental Engineering University of California, Los Angeles, Los Angeles, USA

PUBLICATIONS AND PRESENTATIONS

Yinghui Zhu and J.W. Ju (2019), "Interface energy effect on effective elastic moduli of spheroidal particle reinforced nanocomposites", submitted to *Acta Mechanica*.

Yinghui Zhu and J.W. Ju (2019), "Interface energy effect on effective elastoplastic behavior of spherical particle reinforced metal matrix nanocomposites", to be submitted for publication.

Yinghui Zhu and J.W. Ju (2019), "Effective elastoplastic damage mechanics for fiber reinforced nanocomposites with evolutionary interface debonding", to be submitted to *International Journal of Damage Mechanics*.

Yinghui Zhu and J.W. Ju (2019), “Effective elastoplastic damage mechanics for fiber reinforced nanocomposites with evolutionary interface debonding”, *Symposium on Multiscale Behavior of Damage and Failure Mechanics, Engineering Mechanics Institute Conference 2019*, Pasadena, California, USA.

- Chapter 1 -

INTRODUCTION

Abstract

The concept of composite materials has been around since ancient history. After the long development process, composite materials have already been widely applied in diverse engineering fields, and the exploration of new composite materials never ends. Currently, the composite materials with micrometer scaled or even nanometer scaled reinforcements draw significant attention. Micromechanics theories are proposed to predict the mechanical properties of composite materials with the size of reinforcements in micrometer or larger length scale. However, classical micromechanics frameworks neglect the effect of interface energy and are not capable to determine the mechanical behavior of nanocomposites. Therefore, a theory that considers the interface energy effect are of great importance in predicting the mechanical properties of nanocomposites. In this chapter, composite material is introduced based on its definition, classifications and applications. Furthermore, the micromechanics theories are discussed. At the end, the concept of the interface energy is introduced.

1.1 Composite Materials

In this section, composite materials are introduced in detail. The definitions, the structures, the developments, the classifications and the applications of composite are shown sequentially.

1.1.1 Definitions

A composite material is a solid material that consists two or more distinct phases or materials. Although the components in a composite material are mixed together, they have clear interfaces between the phases that are in contact. Commonly, composite materials have the following characteristics:

1) The components and their volume fractions of a composite are designed for certain purpose;
2) Composite materials are artificial materials with different properties from natural materials;
3) Different from compounds and alloys, the components in composite materials keep their original physical and chemical properties;
4) The overall effective properties of composite materials depend upon the joint effect of all the components and are better than, sometimes totally different from, the properties of any of its component.

1.1.2 Structures of composite materials

A composite material is consisted of the main components and the interfaces. The main components include the matrix and the reinforcements. The matrix and reinforcements have

distinct physical properties, chemical properties and structures. Due to the uniqueness of the structures and constituents, the interfaces are also regarded as one of the phases in the composite material under some occasions. Reinforcements, which are generally fibers, particles or thin films, usually have higher strength and stiffness than the matrix and take most of the loading in the composite. Matrix, on the other hand, is the medium that transfers the loading to the reinforcements through the interface.

In the composite materials, the surface that connects the matrix and the reinforcement is named as the interface. Through the interface, loadings and deformations can be transferred from the matrix to the reinforcement. Due to the different local atomic environment at the interface, the mechanical properties at or near the interface are affected. Further, it is well known that the specific area increases as the volume decreases. The interface renders larger effect on the composite with the reinforcements in smaller sizes. Therefore, the development of nanotechnology draws significant attention on the study of the interface effect both experimentally and theoretically.

The overall properties of a composite material are mainly depending on the physical and chemical properties of the component materials, the distribution of reinforcements, the manufacturing process and the environment of usage. By properly considering these factors, composite materials can be designed to achieve new properties while keeping the main features of its components.

1.1.3 Development of composite materials

In terms of the development process, composite materials can be generally divided into the early-stage composite materials and the modern composite materials. The early use of composite materials can be dated back to the ancient times when the straw reinforced clay, which shares the similar concept of concrete, was utilized in the building walls. Other famous examples of the early-stage composite materials include lacquer wares, bronze wares, etc.

The development of the modern composite materials can be traced back to 1940s. In 1940, the glass fiber reinforced unsaturated polyester resin was firstly employed in the radomes for the military aircrafts. In 1942, glass fiber reinforced plastic (GFRP) is adopted in building a fishing ship. After that, GFRP was widely used in aviation, chemistry, and construction industry during 1960s and 1970s, and is recognized as the first generation of the composite material. The volume fraction of the glass fibers in GFRP varies from 30% to 60%, and the matrix material is generally unsaturated polyester resin, epoxy resin or phenolic resin. Compared with steel, GFRP presents higher specific strength (strength/density) and better corrosion resistance. Since 1980s, the development in the design skills and the manufacturing techniques of composite materials greatly improve the performances of GFRP. However, the respectively low modulus and usage temperature limit the applications GFRP. Hence, GFRP doesn't belong to the advanced composite materials (ACM), where the requirements of ACM are: high specific strength, high specific stiffness, high shear strength and modulus, good high-temperature performance, etc.

To increase Young's modulus in the composite, people started to use the 'advanced fibers' (e.g., boron fibers, carbon fibers and aramid fibers) as the reinforcements instead of the glass fibers in 1950s. Moreover, in contrast to the poor heat resisting property of GFRP, the boron fiber reinforced plastic (BFRP), the carbon fiber reinforced plastic (CFRP) and the kevlar fiber reinforced composite (KFRP) display high operating temperature, which can be higher than *150* Celsius degrees. Therefore, BFRP, CFRP and KFRP are usually termed as the second generation of composite materials.

Advanced fiber reinforced polyimide matrix composites exhibit the operating temperature at about *200* Celsius. If metal is employed as the matrix material, the operating temperature can be increased to *175–900* Celsius. When ceramic is employed as the matrix material, the operating temperature can be *1000–2000* Celsius. In 1970s, the applications of the aluminum oxide fibers and the silicon carbide fibers contribute the properties of heat resisting, high toughness and multifunction in ACM. These composite materials are called the third generation of composite materials. The second and the third generations of composite materials are also referred to as the high-performance composite materials. They are composed of the high-performance reinforcements and the polymer, metal, carbon or ceramic matrix. High-performance composite materials usually possess one or more of the following properties: high specific modulus, high specific strength, good high temperature performance and multi-functional abilities.

1.1.4 Classification of composite materials

Composite materials can be classified according to various aspects. Depending on the applications, composite materials can be classified into structural composite materials and functional composite materials. Structural composite materials are utilized in load-bearing structures. In the structural composites, the reinforcements take most of the loading, and the matrix distributes and transfers the loading to the reinforcements. Functional composite materials possess special physical or chemical properties, such as noise reduction, heat resistance, corrosion resistance, etc. In the functional composite materials, the functional properties always come from the reinforcements, and the matrix material, which integrates the reinforcements, can also enhance the effect.

According to the geometry of the reinforcements, composite materials can be classified into fiber reinforced composites, particle reinforced composites and slice reinforced composites, etc. The fiber reinforced composites include the continuous fiber reinforced composites and discontinuous fiber reinforced composites. The continuous fiber reinforced composites are highly anisotropic and desirable when directionality is considered. The properties of the discontinuous fiber reinforced composites are similar to the particle reinforced composites. Although the particle reinforcing in composites is a less effective mean in strengthening, it is widely used due to the low cost and the ease of production. The main functions of the particle reinforcements in composite materials are adjusting the electric and heat conductivity, decreasing the thermal expansion

coefficient, improving the temperature tolerance and changing the density of the composite, etc. The reinforcements in slice reinforced composites are the slices with similar length and width. When the slices are closely stacked, they can effectively prevent fluid leakage and protect the composite from damaging along the normal direction to the slices. The slice reinforced composites are applied in various fields, including corrosion protection, leakage protection, heat insulation and electrical insulation.

According to the types of matrix material, high-performance composite materials can be classified into metal matrix composites (MMCs) and non-metallic matrix composites. Further, the non-metallic matrix composites include the polymer matrix composites (PMCs) and the ceramic matrix composites (CMCs). The matrix materials of MMCs include aluminum, magnesium, copper, titanium, superalloy, intermetallic compound, refractory metal composite, etc. On the other hand, resin is the most commonly used matrix material of PMCs. Fiber reinforced PMCs, which have high strength and high modulus, are usually adopted as the structural materials. Particle or slice reinforced PMC can be employed as structural and functional materials. CMCs, including aluminum oxide CMCs, silicon carbide CMCs, zirconia CMCs, silicon nitride CMCs, are designed to improve the brittleness of ceramic materials.

1.1.5 Applications of composite materials

Composite materials are used in a wide variety of fields, including aerospace, ground transportation, water transportation, civil engineering, chemical engineering, sports equipment,

energy and environmental protection, medical apparatus, electrical engineering, etc. In aerospace, the manufactures such as Boeing and Airbus have applied the composite materials as the major structural parts in the aircrafts. In architecture, composites offer the designers and the civil engineers materials with better performance in the large-scale projects. In automotive industry, the use of composites makes the vehicles lighter and safer. For sports equipment, carbon fiber reinforced composites provide the features including good durability and lightweight. Moreover, the composites enable the use of the new energies and can improve the efficiency of the traditional energies. Figs. 1–1 to Fig. 1–6 presents several examples of the applications of composite materials.

Figure 1–1 Fairing of the rocket

Figure 1–2 Hall of the speedboat

Figure 1–3 Body of the fighter aircraft

Figure 1–4 Shell of the sports car

Figure 1–5 Bicycle

Figure 1–6 Fishing Rod

1.2 Micromechanics of Composite Materials

Micromechanics is a relatively new branch of continuum mechanics, which studies the deformation of bodies under forces. Traditionally, continuum mechanics assumes homogeneity of the material, which are acceptable macroscopically. However, microscopically, it is found that the microscopic structure of a solid material contains a lot of defects (Qu and Cherkaoui 2006). Although the traditional assumptions hold for the overall properties, they are not valid when the micro-scale ingredient is considered. Micromechanics considers the microstructural characteristics of the materials and homogenizes the microscopic properties to predict the macroscopic properties, which provides the basis for the design and the manufacture. In micromechanics, the studies are typically based on the representative volume element (RVE). The RVE is an element in the composite material that is able to present all the micro-structural information, which is sufficient to characterize the properties of the composite. Within an RVE, the mechanical behavior of the composite can be obtained through solving the boundary value problems following the continuum mechanics theories. The mechanical properties of the constituent phases together with the volume fractions, shapes and orientations of the reinforcements determine the overall properties of the composites.

The origin of micromechanics may be dated back to the Eshelby's work in 1957. Eshelby proved that when a stress-free strain, eigenstrain, is given in an ellipsoidal inclusion in the composite, the strain and stress fields inside the inclusion are uniform. The strain field can be

determined by the celebrated Eshelby tensor. Further, Eshelby (1961) proposed the equivalent principle that an inhomogeneity in the composite can be equivalented into an inclusion with uniform eigenstrain. Here, an inclusion denotes a volume inside a homogeneous material that is of the same material as the matrix, while an inhomogeneity in the composite has different material properties with the matrix. Based on the Eshelby's studies, various micromechanics theories are developed.

The overall properties of a composite material are of important consideration in micromechanics. Hashin and Shtrikman (1963) determined the upper and lower bounds of the effective properties in a composite material. Self-consistent method (Hershey 1954, Budiansky 1965, Hill 1965) and Mori-Tanaka (1973) method extend Eshelby's solution on a single inclusion problem and consider each reinforcement as a single inhomogeneity in the effective medium. Ju and Chen (1994) considers the pairwise particle interactions in the composite. The micromechanics theories enable people to predict the effective mechanical properties of materials and are powerful tools in the design and analysis of new materials.

1.3 Interface Energy and Nanocomposites

Interface is the surface between the matrix and the inhomogeneity in composite materials. Due to the accommodation of two distinct materials, the local atomic environment at interface is different from it associated with the interior. Therefore, the free energy related to the molecules at the matrix-inhomogeneity interface and the molecules in the interior are different. Interface/surface

energy is the excess free energy of the molecules at the interface/surface relative to the molecules in the bulk material. Interface/surface energy was firstly proposed in fluid mechanics and numerically equals to the surface tension (Gibbs 1906). For liquid, interface/surface energy exhibits an elastic tendency of keeping the least surface area, and the interface/surface is under tension, which can resist external forces to some extent. Fig. 1–7 is an example of the effect of interface/surface energy, where a paper clip is held by the water.

Figure 1–7 A paper clip on the water surface

The interface energy effect on overall properties is neglected in the micromechanics theories due to the low specific interface area in consideration. However, when focusing on the nanostructures in a material, the interface energy effect cannot be neglected. Researchers have shown that as the size of the inhomogeneity become smaller, the interface energy effect increases, and one has to take the interface energy into account for the nano-sized inhomogeneities. Therefore,

for nanocomposites, whose reinforcement phase has one or more dimensions in nanometer scale, the effective properties are dependent upon the interface energy. To determine the effective properties of nanocomposites, the interface energy effect can be considered on the classical micromechanics theories.

1.4 Scope and Delimitations

The main focus of the present work is formulating the nanomechanical frameworks that considers the interface energy effect to predict the effective mechanical properties of composite materials. The interface energy effect is simulated by including the in-plane interface stress in the idealized zero-thickness membrane interphase between the matrix and the inhomogeneity, from which the interfacial stress discontinuity conditions are formulated. Further, the effective elastic fields are related between the matrix and the reinforcement by following the homogenization procedures in classical micromechanics theories. As a consequence, the effective mechanical properties that considers the effect of interface energy are obtained for the composites.

Chapter 2 presents the micromechanics theories and the nanomechanics theories. First of all, the basic concepts in classical micromechanics theories are introduced, and the Eshelby's work is explained. Additionally, the micromechanics theories, including the direct Eshelby method, the Mori-Tanaka method, the self-consistent method and the direct particle interaction method, are discussed. Next, the nanomechanical treatment of the interface is introduced. The interface models, the interface constitutive equations and the interface equilibrium equations are discussed. Further,

the available nanomechanics theories are presented.

In Chapter 3, an elastic nanomechanical framework is proposed to determine the effective elastic moduli of the multiphase spherical particle reinforced composites. Instead of applying the Eshelby's solution in classical micromechanics theories, the strain inside of the inhomogeneity is determined through the interfacial stress discontinuity equations. Further, following the effective medium assumption in the Mori-Tanaka method, the effective elastic moduli that considers the interface energy effect are obtained. The results reveal that the interface energy effect induces the size dependence terms on the effective moduli.

Based on the study in Chapter 3, Chapter 4 presents a nanomechanical framework that predicts the effective elastic moduli of the multiphase spheroidal particle reinforced composites. We assume that the spheroidal particles are aligned and randomly distributed in the composite. Further, the similar approaches in Chapter 3 are followed. It is demonstrated that the solutions in Chapter 3 can be obtained by assuming identical semi-axes in the spheroidal particles, and the micromechanics solutions can be recovered by either neglecting the interface energy related terms or considering the large reinforcement particles (in micrometer or larger length scale) in the proposed nanomechanical framework.

In Chapter 5, an elastoplastic nanomechanical framework is proposed to predict the effective elastoplastic properties of the *two*-phase spherical particle reinforced metal matrix nanocomposites (MMNCs). The ductile metal matrix is assumed to be elastoplastic and the spherical reinforcement particles are elastic. Additionally, the continuously weakening restraint of the matrix material

during plastic deformation is considered by the secant moduli.

Chapter 6 presents an elastoplastic damage nanomechanical framework for the *two*-phase continuous fiber reinforced composites. Similar to Chapter 5, the elastoplastic matrix and the elastic reinforcements are assumed. Progressive interface debonding is considered, and the debonded isotropic fibers are equivalented into the perfectly bonded anisotropic fibers. Further, the interfacial stress discontinuity equations, which are induced by the interface energy, are solved for the equivalented fibers, and the effective secant moduli of the composite are derived.

Finally, Chapter 7 concludes the present dissertation of the interface energy effect on the nanocomposites, and the future work is discussed.

1.5 References

Budiansky, Bernard. "On the elastic moduli of some heterogeneous materials." *Journal of the Mechanics and Physics of Solids* 13.4 (1965): 223-227.

Chuang, C. W. "Interface energy and particle size effects on effective properties and damage energy dissipation in nanocomposites." Ph.D. Dissertation at University of California, Los Angeles, CA, 2014.

Eshelby, John D. "The determination of the elastic field of an ellipsoidal inclusion, and related problems." Proceedings of the Royal Society of London A: Mathematical, Physical and Engineering Sciences. Vol. 241. No. 1226. The Royal Society, 1957.

Eshelby, J. D. "Elastic inclusions and inhomogeneities." Progress in solid mechanics 2.1 (1961): 89-140.

Gibbs, Josiah Willard. The scientific papers of J. Willard Gibbs. Vol. 1. Longmans, Green and Company, 1906.

Hashin, Zvi, and Shmuel Shtrikman. "A variational approach to the theory of the elastic behaviour of multiphase materials." Journal of the Mechanics and Physics of Solids 11.2 (1963): 127-140.

Hershey, A. V. "The elasticity of an isotropic aggregate of anisotropic cubic crystals." Journal of Applied mechanics-transactions of the ASME 21.3 (1954): 236-240.

Hill, R1. "A self-consistent mechanics of composite materials." Journal of the Mechanics and

Physics of Solids 13.4 (1965): 213-222.

Hull, Derek, and T. W. Clyne. An introduction to composite materials. Cambridge university press, 1996.

Ju, J. W., and T. Mv Chen. "Micromechanics and effective moduli of elastic composites containing randomly dispersed ellipsoidal inhomogeneities." Acta Mechanica 103.1-4 (1994): 103-121.

Ju, J. W., and T. M. Chen. "Effective elastic moduli of two-phase composites containing randomly dispersed spherical inhomogeneities." Acta Mechanica 103.1-4 (1994): 123-144.

Mori, Tanaka, and K. Tanaka. "Average stress in matrix and average elastic energy of materials with misfitting inclusions." Acta metallurgica 21.5 (1973): 571-574.

Mura, Toshio. Micromechanics of defects in solids. Springer Science & Business Media, 2013.

Nemat-Nasser, Sia, and Muneo Hori. Micromechanics: overall properties of heterogeneous materials. Vol. 37. Elsevier, 2013.

Qu, Jianmin, and Mohammed Cherkaoui. Fundamentals of micromechanics of solids. Hoboken: Wiley, 2006.

Sun, L. Z. "Micromechanics and overall elastoplasticity of discontinuously reinforced metal matrix composites." Ph.D. Dissertation at University of California, Los Angeles, CA, 1998.

Wang, Jianxiang, et al. "Surface stress effect in mechanics of nanostructured materials." Acta Mechanica Solida Sinica 24.1 (2011): 52-82.

Yanase, K. "Micromechanics and effective thermo-mechanical damage and deformation responses of composite materials." Ph.D. Dissertation at University of California, Los Angeles, CA,

2009.

- Chapter 2 -

LITERATURE REVIEW

In this chapter, the micromechanics theories are introduced firstly, in which the Eshelby's inclusion theory, equivalent inclusion principle and the micromechanical approaches in determining the overall effective mechanical properties of composites are explained in detail. The basic assumptions and the homogenization methods of the classical micromechanical approaches are emphasized and are the foundations of the nanomechanics formulations. Second, the main concepts in nanomechanics are introduced, in which the interface models, the interface constitutive equations and the *generalized* Young-Laplace equations are applied in the following chapters.

2.1 Micromechanics of Heterogeneous Materials

2.1.1 Eigenstrain

The definition of eigenstrain is firstly proposed by Eshelby (1957). Eigenstrain is defined as the stress-free stain that corresponds to *zero* stress. The examples of eigenstrain include the thermal strain, the plastic strains and the transformation strain, etc. Before the further explanations on the eigenstrain in the micromechanical formulations are provided, distinguishing the terms inhomogeneity and inclusion are needed. For a domain D, the inclusion is defined as a subdomain

Ω in the domain *D* and the matrix is *D*–Ω. The inclusion and the matrix are of the same material. The eigenstrain $\boldsymbol{\varepsilon}^*$ equals to *zero* in the matrix but *nonzero* in the inclusion; see Figure 2-1. By contrast, the inhomogeneity is defined as a subdomain Ω, which has the different material properties from the matrix *D*–Ω (Qu and Cherkaoui 2006); see Figure 2-2.

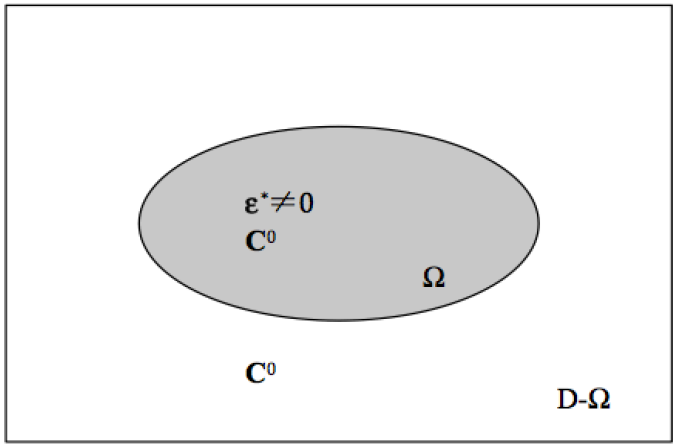

Figure 2–1 An inclusion in the matrix

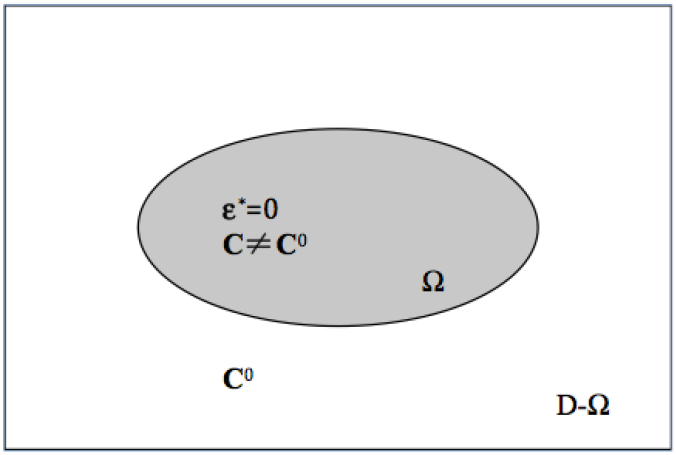

Figure 2–2 An inhomogeneity in the matrix

Now consider the eigenstrain $\boldsymbol{\varepsilon}^*$ prescribed in an inclusion Ω. D is the total domain with the uniform elastic stiffness tensor $\mathbf{C}^0$. The total strain in D is $\boldsymbol{\varepsilon}$ and the elastic strain is $\mathbf{e}$. According to the definition of the eigenstrain, the relation of the total strain, the elastic strain and the eigenstrain can be displayed as

$$e_{ij} = \varepsilon_{ij} - \varepsilon^*_{ij} \tag{2.1}$$

The total strain is related to the displacement through

$$\varepsilon_{ij} = \frac{1}{2}(u_{i,j} + u_{j,i}) \tag{2.2}$$

Therefore, the stress-strain relation can be expressed as

$$\sigma_{ij} = C^0_{ijkl} e_{kl} = C^0_{ijkl}(\varepsilon_{kl} - \varepsilon^*_{kl}) = C^0_{ijkl}(u_{k,l} - \varepsilon^*_{kl}) \tag{2.3}$$

Further, the equilibrium equations render

$$\sigma_{ij,j} = C^0_{ijkl}(u_{k,lj} - \varepsilon^*_{kl,j}) = 0 \tag{2.4}$$

which leads to

$$C^0_{ijkl} u_{k,lj} = C^0_{ijkl} \varepsilon^*_{kl,j} \tag{2.5}$$

If no traction is applied on the boundary, the boundary conditions are

$$\sigma_{ij} n_j = 0 \tag{2.6}$$

Substituting Eq. (2.3) into Eq. (2.6) gives

$$C^0_{ijkl} u_{k,l} n_j = C^0_{ijkl} \varepsilon^*_{kl} n_j \tag{2.7}$$

In Eq. (2.5), $-C^0_{ijkl}\varepsilon^*_{kl,j}$ can be regarded as a body force F_i, and therefore, the Eq. (2.5) turns to be the equilibrium equation for a homogeneous domain under the body force F_i. Similarly, Eq. (2.7) can be regarded as the new boundary condition that a surface traction $C^0_{ijkl}\varepsilon^*_{kl} n_j$ is applied on the

boundary of the domain *D*. As a consequence, the elastic fields of the homogeneous domain, which contains an inclusion, can be solved when the eigenstrain ε_{ij}^{*} is specified.

2.1.2 Eshelby inclusion theory and equivalent principle principle

Consider an ellipsoidal inclusion Ω in an infinite domain *D* with the elastic stiffness tensor $\mathbf{C}_0$. *D* is subjected to a far-field strain $\boldsymbol{\varepsilon}_0$. The eigenstrain $\boldsymbol{\varepsilon}^*$ is uniform in the inclusion and *zero* in the matrix. Eshelby proved that the stress and the strain fields are uniform in the inclusion. In addition, he proposed a constant fourth-order tensor **S**, which is referred to as the Eshelby tensor, to determine the strain field in the inclusion. According to Eshelby, the perturbed strain $\boldsymbol{\varepsilon}'$ due to the eigenstrain is

$$\boldsymbol{\varepsilon}' = \mathbf{S} : \boldsymbol{\varepsilon}^* \qquad \mathbf{x} \in \Omega \tag{2.8}$$

and the stress in the inclusion is,

$$\boldsymbol{\sigma} = \mathbf{C}_0 : \left(\boldsymbol{\varepsilon}_0 + \boldsymbol{\varepsilon}' - \boldsymbol{\varepsilon}^*\right) = \mathbf{C}_0 : \left(\boldsymbol{\varepsilon}_0 + \mathbf{S} : \boldsymbol{\varepsilon}^* - \boldsymbol{\varepsilon}^*\right) \qquad \mathbf{x} \in \Omega \tag{2.9}$$

When the problem of the infinite body *D* containing an ellipsoidal inhomogeneity Ω is considered, the Eshelby's equivalence principle can be applied to equivalent the inhomogeneity into an inclusion with the uniform eigenstrain. Assume that the elastic stiffness tensors of the matrix and the inhomogeneity are $\mathbf{C}_0$ and $\mathbf{C}_1$, respectively, and a strain $\boldsymbol{\varepsilon}_0$ is applied at the far field. The Eshelby's equivalence principle reads

$$\mathbf{C}_0 : \left(\boldsymbol{\varepsilon}_0 + \boldsymbol{\varepsilon}' - \boldsymbol{\varepsilon}^*\right) = \mathbf{C}_1 : \left(\boldsymbol{\varepsilon}_0 + \boldsymbol{\varepsilon}'\right) \tag{2.10}$$

where $\boldsymbol{\varepsilon}^*$ is the uniform eigenstrain. Through Eshelby's equivalence principle, the heterogeneous

body *D* is transformed into a homogeneous body with uniform eigenstrain in Ω. Substitution of Eqs. (2.8) into (2.10) renders

$$\mathbf{C}_0 : \left(\boldsymbol{\varepsilon}_0 + \mathbf{S} : \boldsymbol{\varepsilon}^* - \boldsymbol{\varepsilon}^*\right) = \mathbf{C}_1 : \left(\boldsymbol{\varepsilon}_0 + \mathbf{S} : \boldsymbol{\varepsilon}^*\right) \tag{2.11}$$

from which the eigenstrain can be determined explicitly,

$$\boldsymbol{\varepsilon}^* = -\left(\mathbf{A} + \mathbf{S}\right)^{-1} : \boldsymbol{\varepsilon}_0 \tag{2.12}$$

where $\mathbf{A} = \left(\mathbf{C}_1 - \mathbf{C}_0\right)^{-1} : \mathbf{C}_0$.

Eshelby made a great contribution to the micromechanics, and his work is the foundation of many classical micromechanics theories, including the direct Eshelby method, the Mori-Tanaka method and the self-consistent method, etc.

2.1.3 Determination of the effective moduli

Consider a composite material subjected to the displacement boundary condition as follows,

$$\mathbf{u}\big|_S = \boldsymbol{\varepsilon}_0 \mathbf{x} \tag{2.13}$$

Due to the perturbation of the inhomogeneities in composite material, the elastic fields are not uniform. Typically, the micromechanics theories consider each inhomogeneity as a single inhomogeneity surrounded by the effective matrix with the effective elastic modulus $\hat{\mathbf{C}}_0$ and the effective strain $\hat{\boldsymbol{\varepsilon}}_0$. Therefore, the multi-inhomogeneity problem is simplified into a single-inhomogeneity problem. For the simplified problem, the equivalent inclusion principle leads to

$$\hat{\mathbf{C}}_0 : \left(\hat{\boldsymbol{\varepsilon}}_0 + \hat{\mathbf{S}} : \boldsymbol{\varepsilon}_r^* - \boldsymbol{\varepsilon}_r^*\right) = \mathbf{C}_r : \left(\hat{\boldsymbol{\varepsilon}}_0 + \hat{\mathbf{S}} : \boldsymbol{\varepsilon}_r^*\right) \tag{2.14}$$

where $\mathbf{C}_r$ is the elastic stiffness tensor of the inhomogeneity. The eigenstrain $\boldsymbol{\varepsilon}_r^*$ can be solved

from Eq. (2.14) that

$$\boldsymbol{\varepsilon}_r^* = \left[\left(\mathbf{C}_r - \hat{\mathbf{C}}_0\right) : \hat{\mathbf{S}} + \hat{\mathbf{C}}_0\right]^{-1} : \left(\mathbf{C}_r - \hat{\mathbf{C}}_0\right) : \hat{\boldsymbol{\varepsilon}}_0 \tag{2.15}$$

Furthermore, the total strain in the inhomogeneity can be expressed as

$$\boldsymbol{\varepsilon}_r = \hat{\boldsymbol{\varepsilon}}_0 + \hat{\mathbf{S}} : \boldsymbol{\varepsilon}_r^* = \hat{\mathbf{T}}_r : \hat{\boldsymbol{\varepsilon}}_0 \tag{2.16}$$

where $\hat{\mathbf{T}}_r$ is the local strain concentration tensor, which can be expressed as

$$\hat{\mathbf{T}}_r = \left[\mathbf{I} + \hat{\mathbf{S}} : \hat{\mathbf{C}}_0^{-1} : \left(\mathbf{C}_r - \hat{\mathbf{C}}_0\right)\right]^{-1} \tag{2.17}$$

It is observed from Eq. (2.17) that the total stress is related to the effective strain $\hat{\boldsymbol{\varepsilon}}_0$ and the effective elastic stiffness $\hat{\mathbf{C}}_0$. To explicitly determined the local strain concentration tensor and the effective elastic stiffness tensor, researchers have made various assumptions on the effective matrix. In the following sections, several categories of micromechanical theories are introduced and the corresponding assumptions on the effective matrix are presented.

Furthermore, a global strain concentration tensor $\mathbf{A}_r$ is defined as

$$\boldsymbol{\varepsilon}_r = \mathbf{A}_r : \bar{\boldsymbol{\varepsilon}} \tag{2.18}$$

where $\bar{\boldsymbol{\varepsilon}}$ is the overall effective strain of the composite. Once $\hat{\boldsymbol{\varepsilon}}^0$ and $\hat{\mathbf{C}}^0$ are specified, the relation between $\mathbf{A}_r$ and $\hat{\mathbf{T}}_r$ can be determined, and the overall effective elastic stiffness tensor reveals to be

$$\bar{\mathbf{C}} = \mathbf{C}_0 + \sum_{r=1}^{n} \phi_r (\mathbf{C}_r - \mathbf{C}_0) : \mathbf{A}_r \tag{2.19}$$

where n denotes the number of total reinforcement phases in the composite. Based on the formulation in this section, the direct Eshelby method, the Mori-Tanaka method and the self-

consistent method are discussed sequentially in the following sections.

2.1.4 Direct Eshelby method

The direct Eshelby method assumes dilute reinforcement concentration of inhomogeneities, in which the interactions between the inhomogeneities and between the matrix and the inhomogeneity are neglected. Therefore, the effective matrix yields

$$\hat{\mathbf{C}}^0 = \mathbf{C}^0 \quad \text{and} \quad \hat{\boldsymbol{\varepsilon}}^0 = \boldsymbol{\varepsilon}^0 = \overline{\boldsymbol{\varepsilon}} \tag{2.20}$$

As a consequence, the strain in the inhomogeneity is related to the overall volume-averaged strain,

$$\boldsymbol{\varepsilon}_r = \left[\mathbf{I} + \mathbf{S} : \left(\mathbf{C}_0\right)^{-1} : \left(\mathbf{C}_r - \mathbf{C}_0\right)\right]^{-1} : \overline{\boldsymbol{\varepsilon}} \tag{2.21}$$

where the global and the local strain concentration tensors are identical,

$$\mathbf{A}_r = \mathbf{T}_r = \left[\mathbf{I} + \mathbf{S} : \left(\mathbf{C}_0\right)^{-1} : \left(\mathbf{C}_r - \mathbf{C}_0\right)\right]^{-1} \tag{2.22}$$

According to Eq. (2.19), the effective elastic stiffness tensor equals to

$$\begin{aligned} \overline{\mathbf{C}} &= \mathbf{C}_0 + \sum_{r=1}^{n} \phi_r (\mathbf{C}_r - \mathbf{C}_0) : \mathbf{A}_r \\ &= \mathbf{C}_0 + \sum_{r=1}^{n} \phi_r (\mathbf{C}_r - \mathbf{C}_0) : \left[\mathbf{I} + \mathbf{S} : \left(\mathbf{C}_0\right)^{-1} : \left(\mathbf{C}_r - \mathbf{C}_0\right)\right]^{-1} \end{aligned} \tag{2.23}$$

It is noted that the multi-inhomogeneity problem, in the direct Eshelby method, is regarded as the problem of one inhomogeneity in an otherwise homogeneous matrix material with the original matrix material properties, see Fig. 2-3.

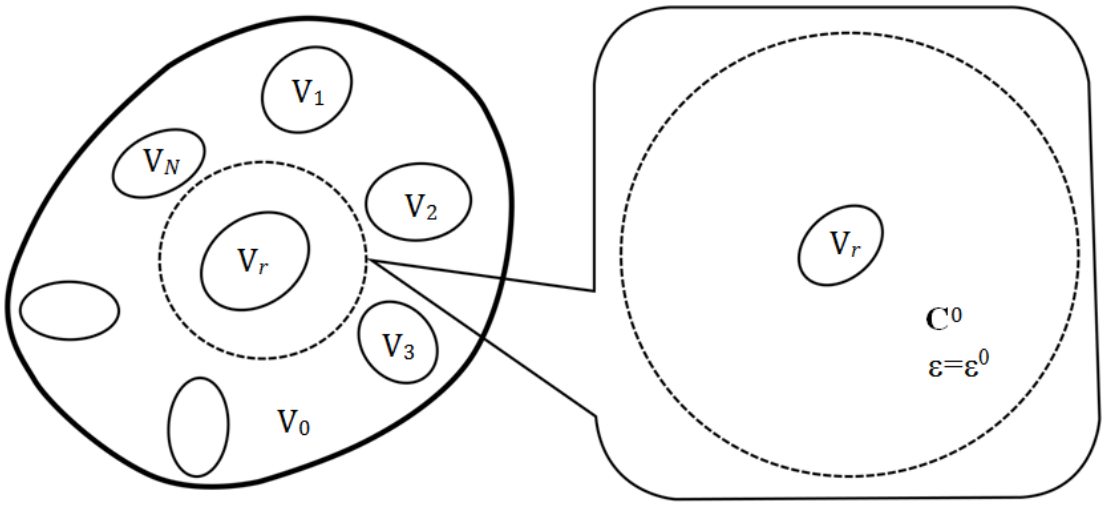

Figure 2–3 The *r*th phase inhomogeneity in the composite following the direct Eshelby method

2.1.5 Mori-Tanaka method

The Mori-Tanaka method is based on the assumption that taking out one inhomogeneity from the composite will not influence the overall effective elastic field. Therefore, an inhomogeneity can be reviewed as the single reinforcement in the uniform matrix of the stiffness tensor $\mathbf{C}_0$, which is subjected to the uniform strain $\bar{\boldsymbol{\varepsilon}}_0$, which implies that

$$\hat{\boldsymbol{\varepsilon}}_0 = \bar{\boldsymbol{\varepsilon}}_0 \quad \text{and} \quad \hat{\mathbf{C}}_0 = \mathbf{C}_0 \tag{2.24}$$

where $\bar{\boldsymbol{\varepsilon}}_0$ is the volume-averaged strain in the matrix when all the inhomogeneities are present.

Based on the assumptions made by Mori and Tanaka, the relation between the strain in *r*th phase inhomogeneities and the volume-averaged strain in matrix becomes

$$\boldsymbol{\varepsilon}_r = \mathbf{T}_r : \bar{\boldsymbol{\varepsilon}}_0 \tag{2.25}$$

where the local strain concentration tensor $\mathbf{T}_r$ is

$$\mathbf{T}_r = \left[\mathbf{I} + \mathbf{S} : \left(\mathbf{C}_0\right)^{-1} : \left(\mathbf{C}_r - \mathbf{C}_0\right)\right]^{-1} \tag{2.26}$$

and the volume-averaged strain in matrix is related to the overall averaged strain through

$$\overline{\boldsymbol{\varepsilon}}_0 = \left[\phi_0 \mathbf{I} + \sum_{r=1}^{n} \phi_r \mathbf{T}_r\right]^{-1} : \overline{\boldsymbol{\varepsilon}} \tag{2.27}$$

From Eqs. (2.25) and (2.27), we have

$$\boldsymbol{\varepsilon}_r = \mathbf{T}_r : \left[\phi_0 \mathbf{I} + \sum_{m=1}^{n} \phi_m \mathbf{T}_m\right]^{-1} : \overline{\boldsymbol{\varepsilon}} \tag{2.28}$$

where the global strain concentration tensor is obtained as

$$\mathbf{A}_r = \mathbf{T}_r : \left[\phi_0 \mathbf{I} + \sum_{m=1}^{n} \phi_m \mathbf{T}_m\right]^{-1} \tag{2.29}$$

Therefore, substituting Eq. (2.29) into Eq. (2.19), the effective elastic stiffness tensor of the composite is determined

$$\overline{\mathbf{C}} = \mathbf{C}_0 + \sum_{r=1}^{n} \phi_r (\mathbf{C}_r - \mathbf{C}_0) : \mathbf{T}_r : \left[\phi_0 \mathbf{I} + \sum_{m=1}^{n} \phi_m \mathbf{T}_m\right]^{-1} \tag{2.30}$$

Similar to the direct Eshelby method, the Mori-Tanaka method considers only one inhomogeneous particle in the otherwise homogeneous effective matrix. However, instead of neglecting the interactions in the composite, Mori and Tanaka considers the interactions through the effective matrix, see Fig. 2-4. Therefore, better estimations of the effective elastic moduli are given by the Mori-Tanaka method than the direct Eshelby method.

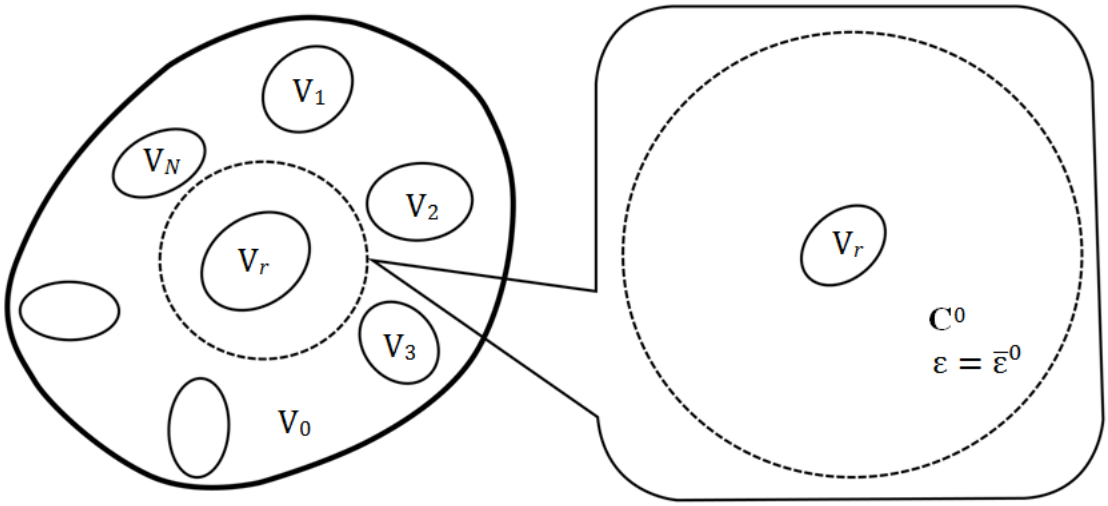

Figure 2–4 The *r*th inhomogeneity in the composite following the Mori-Tanaka method

2.1.6 Self-Consistent method

Similar to the Mori-Tanaka method, the self-consistent method (Budiansky 1965, Hill 1965) assumes that removing one inhomogeneity from the composite will not influence the overall effective properties. The difference is that, in the self-consistent method, the effective elastic moduli and the effective strain of the effective matrix is assumed to be equal to the overall volume-averaged elastic moduli and strain of the composite. The assumptions of the self-consistent method can be written as

$$\hat{\boldsymbol{\varepsilon}}_0 = \bar{\boldsymbol{\varepsilon}} \quad \text{and} \quad \hat{\mathbf{C}}_0 = \bar{\mathbf{C}} \tag{2.31}$$

Therefore, the local strain concentration tensor and the global strain concentration tensor are identical,

$$\mathbf{A}_r = \mathbf{T}_r = \left[\mathbf{I} + \bar{\mathbf{S}} : \left(\bar{\mathbf{C}}\right)^{-1} : \left(\mathbf{C}_r - \bar{\mathbf{C}}\right)\right]^{-1} \tag{2.32}$$

where $\bar{\mathbf{S}}$ is the Eshelby tensor that corresponds to the effective matrix of the elastic stiffness tensor $\bar{\mathbf{C}}$. Substitution of Eq. (2.32) into Eq. (2.19) renders the overall effective elastic stiffness tensor $\bar{\mathbf{C}}$ as

$$\begin{aligned}\bar{\mathbf{C}} &= \mathbf{C}_0 + \sum_{r=1}^{n} \phi_r (\mathbf{C}_r - \mathbf{C}_0) : \mathbf{T}_r : \left[\phi_0 \mathbf{I} + \sum_{m=1}^{n} \phi_m \mathbf{T}_m\right]^{-1} \\ &= \mathbf{C}_0 + \sum_{r=1}^{N} \phi_r (\mathbf{C}_r - \mathbf{C}_0) : \left[\mathbf{I} + \bar{\mathbf{S}} : \left(\bar{\mathbf{C}}\right)^{-1} : \left(\mathbf{C}_r - \bar{\mathbf{C}}\right)\right]^{-1} : \left[\phi_0 \mathbf{I} + \sum_{m=1}^{n} \phi_m \left[\mathbf{I} + \bar{\mathbf{S}} : \left(\bar{\mathbf{C}}\right)^{-1} : \left(\mathbf{C}_m - \bar{\mathbf{C}}\right)\right]^{-1}\right]^{-1}\end{aligned} \tag{2.33}$$

It is noted that Eq. (2.33) is a function of $\bar{\mathbf{C}}$, from which $\bar{\mathbf{C}}$ can be solved, typically iteratively.

The self-consistent method treats the inhomogeneity as a particle in an effective homogeneous matrix. The properties of the effective matrix are assumed to be identical to the unknown yet overall volume-averaged properties of the composite; see Fig. 2-5.

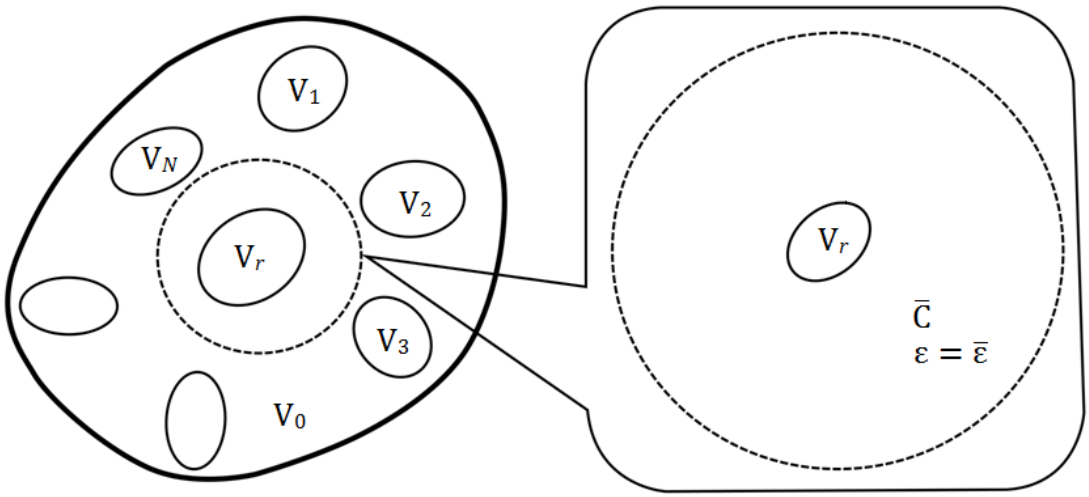

Figure 2–5 The *r*th inhomogeneity in the composite following the self-consistent method

2.1.7 Direct particle interaction model

Ju and Chen (1994a) proposed a micromechanical framework that considers the direct particle interactions to evaluate the effective moduli of composite material with ellipsoidal inhomogeneities. The Green's function is integrated to determine the point-wise strain and stress fields in the composite. Through the ensemble volume average procedures, the effective elastic fields are obtained from the point-wise solutions. The governing equations are derived to determine the effective elastic moduli, which are

$$\bar{\boldsymbol{\sigma}} = \mathbf{C}_0 : \left(\bar{\boldsymbol{\varepsilon}} - \sum_{r=1}^{n} \phi_r \bar{\boldsymbol{\varepsilon}}_r^* \right) \tag{2.34}$$

$$\bar{\boldsymbol{\varepsilon}} = \boldsymbol{\varepsilon}_0 + \sum_{r=1}^{n} \phi_r \mathbf{S} : \bar{\boldsymbol{\varepsilon}}_r^* \tag{2.35}$$

$$-\left(\mathbf{A}_r + \mathbf{s}\right) : \bar{\boldsymbol{\varepsilon}}_r^* = \boldsymbol{\varepsilon}_0 + \bar{\boldsymbol{\varepsilon}}_r{}'^{p} \tag{2.36}$$

$$\left(1 - \sum_{r=1}^{n} \phi_r \right) \bar{\boldsymbol{\varepsilon}}_r{}'^{m} + \sum_{r=1}^{n} \phi_r \bar{\boldsymbol{\varepsilon}}_r^{p} = \sum_{r=1}^{n} \phi_r \left(\mathbf{S} - \mathbf{s}_r \right) : \bar{\boldsymbol{\varepsilon}}_r^* \tag{2.37}$$

where $\mathbf{S}$ is a fourth-order constant tensor, $\mathbf{s}_r$ is the Eshelby tensor for rth phase particles, $\bar{\boldsymbol{\varepsilon}}_r{}'^{p}$ corresponds to the interaction between the inhomogeneities. The effective moduli can be solved from Eqs. (2.34)–(2.37) if one can determine $\bar{\boldsymbol{\varepsilon}}_r{}'^{p}$ explicitly. By neglecting $\bar{\boldsymbol{\varepsilon}}_r{}'^{p}$, Ju and Chen proved that their framework provides the same solution as the Hashin-Shtrikman lower bound and the Mori-Tanaka method. Further, Ju and Chen (1994b) solved $\bar{\boldsymbol{\varepsilon}}_r{}'^{p}$ by considering the pairwise particle interactions and improved the accuracy of the prediction.

2.2 Nanomechanics of Heterogeneous Materials

2.2.1 Interface energy and interface stress

Interface in the heterogeneous materials is the surface between the matrix and the reinforcement. It is well-known that, due to the different local micro-structures at the interface and in the interior, the mechanical properties at or near the interface are different from the mechanical properties of the abutting materials. However, in the classical micromechanics theories, the difference is usually neglected, and the perfect interface bonding conditions are adopted, in which the displacements and the stresses through the interface are continuous.

Gibbs (1928) firstly introduced the concept of interface energy. The interface energy is defined as the excess free energy at the interface, which is due to the different local micro-structure at the interface. Interface stress is a different concept from the interface energy for solids, despite they always treated as equivalent terms in fluid mechanics. Various definitions of the interface stress are proposed in literature. Ibach and Harald (1997) defined the interface stress as the change of the bulk stress near the interface,

$$\tau_{\alpha\beta} = \int_{-\infty}^{+\infty} (\sigma_{\alpha\beta}(\mathrm{z}) - \sigma_{\alpha\beta}^{b}) d\mathrm{z} \tag{2.38}$$

where $\tau_{\alpha\beta}$ is the interface stress (α, β=1,2, are the two perpendicular tangential directions of interface), $\sigma_{\alpha\beta}(\mathrm{z})$ is the stress along the *z*-direction (the normal direction to the interface) and σ_{ij}^{b} is the stress on the interface. It is observed from Eq. (2.38) that the unit of the interface stress

is force per unit length. Shuttleworth (1950) followed the principle of virtual work that related the interface stress and the interface energy,

$$\tau_{\alpha\beta} = \gamma\delta_{\alpha\beta} + \frac{\partial\gamma}{\partial\varepsilon_{\alpha\beta}} \tag{2.39}$$

where γ is the interface energy density. Eq. (2.39) is referred to as the Shuttleworth equation.

The change in the local atomic environment leads to the change of the interface energy and, consequently, the interface stress. Therefore, the interface energy and the interface stress are related to the deformation of the interface (Duan et al. 2005a). According to Bottomley and Ogino (2001), Miller and Shenoy (2000), a linear constitutive relation is proposed for the interface stress and the interface strain,

$$\boldsymbol{\tau} = \mathbf{C}^S : \boldsymbol{\varepsilon}^S \tag{2.40}$$

where $\mathbf{C}^S$ is the *two*-dimensional elastic stiffness tensor of the interface, $\boldsymbol{\varepsilon}^S$ is the interface strain tensor composed of the tangential components of the strain at the interface, and $\boldsymbol{\tau}$ denotes the interface stress tensor. Further, Duan et al. (2005a) suggested a linear isotropic constitutive relation

$$\boldsymbol{\tau} = 2\mu_S\boldsymbol{\varepsilon}^S + \lambda_S(\mathrm{tr}\,\boldsymbol{\varepsilon}^S)\mathbf{1} \tag{2.41}$$

where λ_S and μ_S are the interfacial lamé constants and $\mathbf{1}$ is the *two*-dimensional second-order unit tensor. If written in the form with the interfacial bulk modulus and the interfacial shear modulus, Eq. (2.41) becomes

$$\tau_{\alpha\beta} = 2K_S\left(\tfrac{1}{2}\varepsilon^S_{\theta\theta}\delta_{\alpha\beta}\right) + 2\mu_S\left(\varepsilon^S_{\alpha\beta} - \tfrac{1}{2}\varepsilon^S_{\theta\theta}\delta_{\alpha\beta}\right) \tag{2.42}$$

where K_S and μ_S are the interfacial bulk and shear modulus, respectively.

2.2.2 Interface models

To simulate the interface energy effect on the mechanical properties of the composite, interface models are proposed in the literature, including the free sliding model, the linear spring model, the dislocation-like model and the interface stress model, etc. (Duan et al., 2005b). In the free sliding model, the traction and the displacement along the direction normal to the interface are continuous, while the components of the traction in the tangential direction is zero, that is, we have

$$\begin{cases} \mathbf{n}\cdot[\boldsymbol{\sigma}]\cdot\mathbf{n}=0 \\ [\mathbf{u}]\cdot\mathbf{n}=0 \\ \mathbf{P}\cdot\boldsymbol{\sigma}\cdot\mathbf{n}=0 \end{cases} \tag{2.43}$$

where $\mathbf{P}=\mathbf{I}^{(2)}-\mathbf{n}\otimes\mathbf{n}$, $\mathbf{I}^{(2)}$ is the 2nd-order identity tensor, $\mathbf{n}$ is the unit normal vector to the interface and the bracket $[\cdot]$ represents the interfacial discontinuity of the inner value from the matrix to the inhomogeneity.

The linear spring model assumes continuous traction and discontinuous displacements at the interface, and the traction at interface is proportionally related to the interfacial displacement discontinuity,

$$\begin{cases} [\boldsymbol{\sigma}]\cdot\mathbf{n}=0 \\ \mathbf{P}\cdot\boldsymbol{\sigma}\cdot\mathbf{n}=k_1\mathbf{P}\cdot[\mathbf{u}] \\ \mathbf{n}\cdot\boldsymbol{\sigma}\cdot\mathbf{n}=k_2[\mathbf{u}]\cdot\mathbf{n} \end{cases} \tag{2.44}$$

where k_1 and k_2 are the spring constants in the tangential direction and the normal direction, respectively. When $k_1=k_2=0$, tractions become *zero*, which corresponds to the complete

debonding of the interface. When k_1 and k_2 go to infinity, the displacement discontinuity has to be *zero*, which means that the interface is perfectly bonded.

Dislocation-like model, similar to the linear spring model, assumes the continuous traction and the discontinuous displacement. However, the displacements on the two sides of an interface are assumed to be proportionally related, which can be expressed as

$$\begin{cases} [\boldsymbol{\sigma}]\cdot\mathbf{n}=0 \\ \mathbf{P}\cdot\mathbf{u}^m = k_1\mathbf{P}\cdot\mathbf{u}^i \\ \mathbf{n}\cdot\mathbf{u}^m = k_2\mathbf{n}\cdot\mathbf{u}^i \end{cases} \tag{2.45}$$

where $\mathbf{u}^m$ is the displacement on matrix side and $\mathbf{u}^i$ is the displacement on the inhomogeneity side, and k_1 and k_2 are two constants.

2.2.3 Interface stress model

Gurtin and Murdoch (1975) studied the elastic material surface/interface under the continuum mechanics theory. They established a theoretical framework of the interface, in which membrane theory is followed. According to Gurtin and Murdoch, the equilibrium equations at the interface can be written as

$$[\boldsymbol{\sigma}]\cdot\mathbf{n} = -\nabla_S\cdot\boldsymbol{\tau} \tag{2.46}$$

where $\mathbf{n}$ is a unit normal vector of interface pointing from inhomogeneity to matrix and $\nabla_S\cdot$ denotes the interface divergence. Eq. (2.46) is names as the *generalized* Young-Laplace equation, which corresponds to the Young-Laplace equation in fluid mechanics. Chen, Chiu and Weng (2006) presented the derivation of the *generalized* Young-Laplace equation by considering the

equilibrium conditions for an element on the interface. For a prolate spheroid,

$$\frac{r^2}{b^2}+\frac{z^2}{a^2}=1 \quad 0\le\phi\le 2\pi \quad a>b \tag{2.47}$$

the *generalized* Young-Laplace equations under the cylindrical coordinate system are

$$\left[\sigma_{31}\right]=-\frac{1}{h_1h_2}\left(h_2\frac{\partial\tau_{11}}{\partial\phi}+\frac{\partial h_2}{\partial z}\left(\tau_{12}+\tau_{21}\right)+h_1\frac{\partial\tau_{21}}{\partial z}\right) \tag{2.48}$$

$$\left[\sigma_{32}\right]=-\frac{1}{h_1h_2}\left(h_2\frac{\partial\tau_{12}}{\partial\phi}+\frac{\partial h_1}{\partial z}\left(-\tau_{11}+\tau_{22}\right)+h_2\frac{\partial\tau_{22}}{\partial z}\right) \tag{2.49}$$

$$\left[\sigma_{33}\right]=-\left(\frac{\tau_{11}}{R_1}+\frac{\tau_{22}}{R_2}\right) \tag{2.50}$$

where $h_1=r$, $h_2=\sec\alpha$, $\alpha=\tan^{-1}\left(\frac{\mathrm{d}r}{\mathrm{d}z}\right)$, and $R_1=-b\left(1+\frac{z^2}{a^2}\left(\frac{b^2}{a^2}-1\right)\right)^{1/2}$, $R_2=-\frac{a^2}{b}\left(1+\frac{z^2}{a^2}\left(\frac{b^2}{a^2}-1\right)\right)^{3/2}$. The *generalized* Young-Laplace equations for a spherical particle with radius *r* are expressed under the spherical coordinate system as

$$[\sigma_{rr}]=\frac{\tau_{\phi\phi}+\tau_{\theta\theta}}{r} \tag{2.51}$$

$$[\sigma_{r\theta}]=-\left(\frac{1}{r}\frac{\partial\tau_{\theta\theta}}{\partial\theta}+\frac{1}{r\sin\theta}\frac{\partial\tau_{\theta\varphi}}{\partial\varphi}+\frac{\tau_{\theta\theta}-\tau_{\varphi\varphi}}{r}\cot\theta\right) \tag{2.52}$$

$$[\sigma_{r\varphi}]=-\left(\frac{1}{r}\frac{\partial\tau_{\theta\varphi}}{\partial\theta}+\frac{1}{r\sin\theta}\frac{\partial\tau_{\varphi\varphi}}{\partial\varphi}+\frac{2\tau_{\theta\varphi}}{r}\cot\theta\right) \tag{2.53}$$

For a circular fiber with radius *a*, the generalized Young-Laplace equations under the cylindrical coordinate system becomes

$$\left[\sigma_{rr}\right]=\frac{\tau_{\theta\theta}}{a} \tag{2.54}$$

$$\left[\sigma_{r\theta}\right]=-\frac{1}{a}\frac{\partial\tau_{\theta\theta}}{\partial\theta} \tag{2.55}$$

$$\left[\sigma_{rz}\right]=-\frac{1}{a}\frac{\partial\tau_{\theta z}}{\partial\theta} \tag{2.56}$$

Since the derivations of the *generalized* Young-Laplace equations strictly follow the membrane theory of thin shells, one may refer to the derivations of the equilibrium equations in the membrane theory for details. In the interface stress model, the interface energy effect is simulated by inducing the interface stress in the membrane-type interface, and the *generalized* Young-Laplace equations are formulated accordingly. For a coherent interface, when the interface energy effect is considered, the continuous displacement together with the *generalized* Young-Laplace equations are the boundary conditions that need to be satisfied when solving the elastic field of a composite material.

2.3 References

Bottomley, D. J., and T. Ogino. "Alternative to the Shuttleworth formulation of solid surface stress." *Physical Review B* 63.16 (2001): 165412.

Budiansky, Bernard. "On the elastic moduli of some heterogeneous materials." Journal of the Mechanics and Physics of Solids 13.4 (1965): 223-227.

Chen, Tungyang, Min-Sen Chiu, and Chung-Ning Weng. "Derivation of the generalized Young-Laplace equation of curved interfaces in nanoscaled solids." Journal of Applied Physics 100.7 (2006): 074308.

Duan, H. L., et al. "Size-dependent effective elastic constants of solids containing nano-inhomogeneities with interface stress." Journal of the Mechanics and Physics of Solids 53.7 (2005a): 1574-1596.

Duan, H. L., et al. "Stress concentration tensors of inhomogeneities with interface effects." Mechanics of Materials 37.7 (2005b): 723-736.

Eshelby, John D. "The determination of the elastic field of an ellipsoidal inclusion, and related problems." Proceedings of the Royal Society of London A: Mathematical, Physical and Engineering Sciences. Vol. 241. No. 1226. The Royal Society, 1957.

Gao, X-L., and H. M. Ma. "Solution of Eshelby's inclusion problem with a bounded domain and Eshelby's tensor for a spherical inclusion in a finite spherical matrix based on a simplified strain gradient elasticity theory." Journal of the Mechanics and Physics of Solids 58.5 (2010):

779-797.

Gibbs, Josiah Willard. The collected works of J. Willard Gibbs. Eds. Henry Andrews Bumstead, and William Raymond Longley. Vol. 1. Longmans, Green and Company, 1928.

Gurtin, Morton E., and A. Ian Murdoch. "A continuum theory of elastic material surfaces." Archive for Rational Mechanics and Analysis 57.4 (1975): 291-323.

Hashin, Z., and S. Shtrikman. "On some variational principles in anisotropic and nonhomogeneous elasticity." Journal of the Mechanics and Physics of Solids 10.4 (1962): 335-342.

Hashin, Z., and S. Shtrikman. "A variational approach to the theory of the elastic behaviour of multiphase materials." Journal of the Mechanics and Physics of Solids 11.2 (1963): 127-140.

Hill, R1. "A self-consistent mechanics of composite materials." Journal of the Mechanics and Physics of Solids 13.4 (1965): 213-222.

Ibach, Harald. "The role of surface stress in reconstruction, epitaxial growth and stabilization of mesoscopic structures." Surface science reports 29.5 (1997): 195-263.

Ju, J. W., and T. M Chen. "Micromechanics and effective moduli of elastic composites containing randomly dispersed ellipsoidal inhomogeneities." Acta Mechanica 103.1-4 (1994): 103-121.

Ju, J. W., and T. M. Chen. "Effective elastic moduli of two-phase composites containing randomly dispersed spherical inhomogeneities." Acta Mechanica 103.1-4 (1994): 123-144.

Ju, J. W., and T. M. Chen. "Micromechanics and effective elastoplastic behavior of two-phase metal matrix composites." Journal of engineering materials and technology 116.3 (1994): 310-318.

Miller, Ronald E., and Vijay B. Shenoy. "Size-dependent elastic properties of nanosized structural elements." Nanotechnology 11.3 (2000): 139.

Mori, Tanaka, and K. Tanaka. "Average stress in matrix and average elastic energy of materials with misfitting inclusions." Acta metallurgica 21.5 (1973): 571-574.

Mura, Toshio. Micromechanics of defects in solids. Springer Science & Business Media, 2013.

Norris, A. N. "A differential scheme for the effective moduli of composites." Mechanics of materials 4.1 (1985): 1-16.

Qu, Jianmin, and Mohammed Cherkaoui. Fundamentals of micromechanics of solids. Hoboken: Wiley, 2006.

Reuss, A., and Z. Angnew. "A calculation of the bulk modulus of polycrystalline materials." Math Meth 9 (1929): 55.

Shuttleworth, Ro. "The surface tension of solids." Proceedings of the physical society. Section A 63.5 (1950): 444.

Voigt, W. "On the relation between the elasticity constants of isotropic bodies." Ann. Phys. Chem 274 (1889): 573-587.

- Chapter 3 -

INTERFACE ENERGY EFFECT ON THE EFFECTIVE ELASTIC MODULI OF SPHERICAL PARTICLE-REINFORCED NANOCOMPOSITES

Abstract

In this chapter, the effective elastic moduli are derived for the spherical particle reinforced nanocomposite. The interface energy effect is considered for the nanocomposite. To simulate the interface energy effect, the interface is simulated by the zero-thickness membrane interphase with the interface stress. The interface stress is determined by a linear isotropic constitutive equation of the idealized interphase. The elastic fields in the particles and the elastic fields in the matrix are related by solving the equilibrium equations of the interphase. Further, the homogenization procedures in the classical micromechanics theories, including the direct Eshelby method, the Mori-Tanaka method, the self-consistent method and the direct particle interaction model, are adopted in determining the effective elastic moduli of the nanocomposite. Comparisons are made between the current nanomechanical framework and the micromechanical frameworks. It is observed that the effective elastic moduli become size-dependent when the interface energy effect is considered, and the effect of interface energy is negatively related to the size of the particles.

3.1 Introduction

Nanocomposites are the composite materials with one or more dimensions of their reinforcement phases in the nanometer scale. Currently, with the advancement in nanotechnology, nanocomposites have attracted more and more attentions. Due to the large specific interface area of the reinforcements in the nanocomposites, the effect of the interface energy becomes an important factor that determine the mechanical properties of the nanocomposites. Interface energy, which is originated from the different local microstructures at the interface, affects the elastic fields near the interface, and perturbs the effective elastic fields in the composites. The concept of interface energy was firstly introduced by Gibbs (1906). Since then, the interface energy and its effect are studied by many researchers (Shuttleworth, 1950; Herring, 1953; Orowan, 1970; Gurtin and Murdoch, 1975; Murr, 1975; Cahn, 1978; Cammarata, 1994; Chen, Chiu and Weng, 2006; Duan et al., 2005). To simulate the interface energy effect on the elastic fields, Gurtin and Murdoch (1975) established an interface framework that treats the interface as a zero-thickness interphase between the matrix phase and the reinforcement phase., from which the interface continuity equations; i.e., the *generalized* Young-Laplace equations, are proposed. The elastic fields at the interface on the matrix side and on the reinforcement side are readily related through the *generalized* Young-Laplace equations.

The predictions on the effective elastic moduli of the composite materials are extensively discussed in the micromechanics field, and various micromechanical theories are developed based

on different types of simplifications. For example, the direct Eshleby method totally neglects the particle interactions in the composite and the Mori-Tanaka method neglects the near field particle interactions. Ju and Chen (1994a) proposed an analytical framework that considers the particle interactions exactly and directly. Further, they presented an approximate solution that considers the inter-particle interaction, and their prediction exhibits good compatibility with the experimental data even for the composites with moderately high particle concentrations.

In this chapter, a nanomechanical framework in determining the effective elastic moduli of the nanocomposites reinforced by the spherical particles is established. The nanomechanics framework, which is based on the micromechanics theories, takes the interface energy effect into consideration. Unlike the assumption of perfect interface condition in micromechanics, discontinuities of the stresses are considered at the interface. Solving the interface discontinuity equations; i.e., the generalized Young-Laplace equations, the interfacial strain discontinuity is obtained. Further, an interface average procedure is carried out for the strain discontinuity to consider the averaged interface energy effect over the interface. Consequently, the strain field in the particle and the strain field in the matrix are related, and the effective elastic moduli can be solved. The effective elastic moduli are derived following the homogenization approaches of the direct Eshelby method, the Mori-Tanaka method and the generalized self-consistent method, respectively. Isotropic interface energy effect is noticed on the effective elastic moduli. The results are revealed to be depending on the size and the volume fraction of the reinforcement.

3.2 Equivalent Inclusion Method with Interface Energy Effect

Eshelby (1957) proposed an equivalent inclusion principle that is able to equivalent the inhomogeneity material into the matrix material with an eigenstrain field inside the original inhomogeneity domain. Moreover, Eshelby proved that the eigenstrain field is uniform when the shape of the inhomogeneity is an ellipsoid. For an ellipsoidal particle with the elastic stiffness tensor $\mathbf{C}_1$ embedded in a homogeneous matrix with the elastic stiffness tensor $\mathbf{C}_0$, the equivalence inclusion principle can be written as

$$\mathbf{C}_0 : \left(\boldsymbol{\varepsilon}_0 + \mathbf{S} : \boldsymbol{\varepsilon}^* - \boldsymbol{\varepsilon}^*\right) = \mathbf{C}_1 : \left(\boldsymbol{\varepsilon}_0 + \mathbf{S} : \boldsymbol{\varepsilon}^*\right) \tag{3. 1}$$

where $\boldsymbol{\varepsilon}_0$ is the far-field strain, $\boldsymbol{\varepsilon}^*$ is the eigenstrain and $\mathbf{S}$ is the Eshelby tensor. It is noticed that the inhomogeneity problem becomes an inclusion problem through the equivalence. The strain and stress fields in the inhomogeneity are simulated by adjusting the eigenstrain in the equivalented inclusion.

Following the Eshelby's equivalent inclusion principle in the micromechanics, an equivalent inclusion method is proposed in this section to that incorporates the interface energy effect on the elastic fields. Consider an ellipsoidal inhomogeneity Ω_1 in the matrix D-Ω_1. The elastic stiffness tensor of the particle and the matrix are $\mathbf{C}_1$ and $\mathbf{C}_0$, respectively. The total strain field in the inhomogeneity can be displayed as

$$\boldsymbol{\varepsilon}_1 = \boldsymbol{\varepsilon}_0 + \boldsymbol{\varepsilon}^p + \boldsymbol{\varepsilon}' \tag{3. 2}$$

where $\boldsymbol{\varepsilon}_1$ is the total strain in the inhomogeneity, $\boldsymbol{\varepsilon}_0$ is the far field strain, $\boldsymbol{\varepsilon}^p$ is the perturbed

strain due to the interface energy effect and $\boldsymbol{\varepsilon}'$ is the perturbed strain field due to the interaction between the inhomogeneity and the matrix.

To this end, the inhomogeneity is transformed into the matrix, and the original heterogeneous material becomes a homogeneous material with the eigenstrain $\boldsymbol{\varepsilon}^*$ in Ω_1. According to Eshelby, the perturbed strain $\boldsymbol{\varepsilon}'$ can be expressed as follows,

$$\boldsymbol{\varepsilon}' = \mathbf{S} : \boldsymbol{\varepsilon}^* \tag{3. 3}$$

The total strains in the original inhomogeneity and the equivalented inclusion are identical. However, due to the stress-free eigenstrain $\boldsymbol{\varepsilon}^*$ in the inclusion, the elastic strain $\mathbf{e}_1$ of the equivalented inclusion becomes

$$\mathbf{e}_1 = \boldsymbol{\varepsilon}_1 - \boldsymbol{\varepsilon}^* \tag{3. 4}$$

To ensure the stress in Ω_1 before and after the equivalence are equal, the eigenstrain needs to be adjusted. Then, the equivalent inclusion equation with interface energy effect can be demonstrated as

$$\mathbf{C}_0 : \left(\boldsymbol{\varepsilon}_0 + \boldsymbol{\varepsilon}^p + \mathbf{S} : \boldsymbol{\varepsilon}^* - \boldsymbol{\varepsilon}^*\right) = \mathbf{C}_1 : \left(\boldsymbol{\varepsilon}_0 + \boldsymbol{\varepsilon}^p + \mathbf{S} : \boldsymbol{\varepsilon}^*\right) \tag{3. 5}$$

Conventionally, the only unknown in the equivalent inclusion equation is the eigenstrain $\boldsymbol{\varepsilon}^*$. Therefore, the eigenstrain can be solved from Eq. (3.1). However, in Eq. (3.5), one more unknown, $\boldsymbol{\varepsilon}^p$, is induced due to the interface energy. To determine the two unknowns, one more equation is required. Further, it is noticed that, if the total strain in the inhomogeneity is solved directly, the equivalent inclusion equation can be written in the following form

$$\mathbf{C}_0 : \left(\boldsymbol{\varepsilon}_1 - \boldsymbol{\varepsilon}^*\right) = \mathbf{C}_1 : \boldsymbol{\varepsilon}_1 \tag{3. 6}$$

where the eigenstrain can be determined.

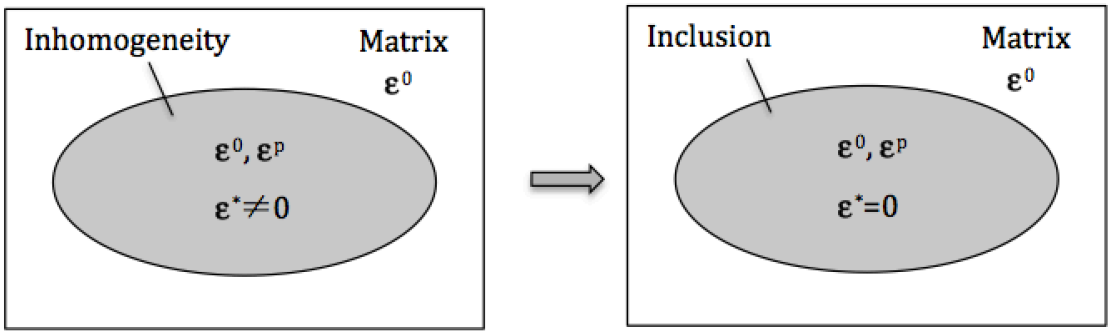

Figure 3–1 Equivalent Inclusion Method

3.3 Interface Boundary Conditions

In classical micromechanics, the interface energy effect is neglected, and the interface between an inhomogeneity and the surrounding matrix is assumed to be perfect, where both of the displacement and the stress are continuous. However, for nanocomposites, the interface energy effect is proved to be important in the determination of the overall effective properties. To simulate the interface energy effect, the interface stress model is adopted. Therefore, if perfect interface bonding condition is considered, the displacement remains to be continuous. Nevertheless, the stress at the interface is discontinuous due to the interface stress. Following the interface stress model, the interfacial stress discontinuity condition can be represented by the *generalized* Young-Laplace equations, which are

$$[\boldsymbol{\sigma}]\cdot\mathbf{n} = -\nabla_S \cdot \boldsymbol{\tau} \tag{3. 7}$$

where $\boldsymbol{\tau}$ is the interface stress, $\mathbf{n}$ is the unit normal vector to the interface, which points the matrix, and $\nabla_S \cdot$ is the interface divergence operator. Here, [•] represents the difference of the said value between the matrix and the inhomogeneity. As a consequence, $[\boldsymbol{\sigma}]\cdot\mathbf{n}$ denotes the discontinuity of the traction on the two sides of the membrane interface. The detailed expressions of the *generalized* Young-Laplace equations for spherical particles are (Chen, Chiu and Weng, 2006),

$$\left[\sigma_{rr}\right]=\frac{\tau_{\theta\theta}+\tau_{\phi\phi}}{a} \tag{3. 8}$$

$$\left[\sigma_{r\theta}\right]=-\frac{1}{a}\left(\frac{\partial\tau_{\theta\theta}}{\partial\theta}+\frac{1}{\sin\theta}\frac{\partial\tau_{\theta\phi}}{\partial\phi}+(\tau_{\theta\theta}-\tau_{\phi\phi})\cot\theta\right) \tag{3. 9}$$

$$\left[\sigma_{r\phi}\right]=-\frac{1}{a}\left(\frac{\partial\tau_{\theta\phi}}{\partial\theta}+\frac{1}{\sin\theta}\frac{\partial\tau_{\phi\phi}}{\partial\phi}+2\tau_{\theta\phi}\cot\theta\right) \tag{3. 10}$$

where *a* is the radius of the spherical particle. It is observed that the size of the reinforcement is considered in the *generalized* Young-Laplace equations.

Now consider an inclusion problem. The displacements are continuous through the interface, that is, we have

$$[u_i]=u_i(S^+)-u_i(S^-)=0 \tag{3. 11}$$

where S^+ is the matrix side of interface and S^- is the inclusion side of the interface. Accordingly, the gradient of the displacements can be discontinuous through the interface (Mura 2013, Qu and Cherkaoui 2006),

$$[u_{i,j}]=u_{i,j}(S^+)-u_{i,j}(S^-)=\lambda_i n_j \tag{3. 12}$$

where λ_i denotes the magnitude of discontinuity. It is noted that the discontinuity is along the

normal direction to the interface, and the displacement gradient is continuous in the tangential direction to the interface. Further the strain discontinuity across the interface is given by,

$$\varepsilon_{ij}^{\lambda} \equiv [\varepsilon_{ij}] = \frac{1}{2}\left([u_{i,j}] + [u_{j,i}]\right) = \frac{1}{2}(\lambda_i n_j + \lambda_j n_i) \tag{3. 13}$$

where $\varepsilon_{ij}^{\lambda}$ is the discontinuity of the total strain through the interface. Then, the interfacial discontinuity of elastic strain becomes

$$[e_{ij}] = [\varepsilon_{ij}] - [\varepsilon_{ij}^{*}] \tag{3. 14}$$

where e_{ij} is the elastic strain in the inclusion. Since the eigenstrain is zero in the matrix and $\boldsymbol{\varepsilon}^{*}$ in the inclusion, the interfacial discontinuity of the eigenstrain is

$$[\varepsilon_{ij}^{*}] = -\varepsilon_{ij}^{*}. \tag{3. 15}$$

The substitution of Eqs. (3.13) and (3.15) into Eq. (3.14) gives

$$[e_{ij}] = \frac{1}{2}(\lambda_i n_j + \lambda_j n_i) + \varepsilon_{ij}^{*} \tag{3. 16}$$

Therefore, the interfacial stress discontinuity renders

$$[\sigma_{ij}] = C_{ijkl}^{0}[e_{kl}] = C_{ijkl}^{0}([\varepsilon_{kl}] - [\varepsilon_{kl}^{*}]) = C_{ijkl}^{0}(\varepsilon_{kl}^{\lambda} + \varepsilon_{kl}^{*}) \tag{3. 17}$$

or in the tensor form as

$$[\boldsymbol{\sigma}] = \mathbf{C}_0 : (\boldsymbol{\varepsilon}^{\lambda} + \boldsymbol{\varepsilon}^{*}) \tag{3. 18}$$

Consequently, the traction discontinuity at interface becomes

$$[\boldsymbol{\sigma}] \cdot \mathbf{n} = \mathbf{C}_0 : (\boldsymbol{\varepsilon}^{\lambda} + \boldsymbol{\varepsilon}^{*}) \cdot \mathbf{n} \tag{3. 19}$$

and substitution of Eq. (3.19) into Eq. (3.7) gives

$$\mathbf{C}_0 : (\boldsymbol{\varepsilon}^{\lambda} + \boldsymbol{\varepsilon}^{*}) \cdot \mathbf{n} = -\nabla_S \cdot \boldsymbol{\tau} \tag{3. 20}$$

In Eq. (3.20), the interfacial stress discontinuity $\boldsymbol{\varepsilon}^{\lambda}$ is related to the eigenstrain $\boldsymbol{\varepsilon}^{*}$ and the

interface stress $\boldsymbol{\tau}$. To determine the interface stress, a linear interface constitutive relation is assumed, which leads to

$$\boldsymbol{\tau} = \mathbf{C}^S : \boldsymbol{\varepsilon}^S \tag{3. 21}$$

where $\boldsymbol{\varepsilon}^S$ is the interface strain and $\mathbf{C}^S$ is the elastic stiffness tensor of the interface. The interface strain is composed of the tangential components of the strain at the interface. Further, it is acknowledged by the previous researchers that the linear isotropic interface elastic stiffness tensor can be adopted, which can be written as

$$\mathbf{C}^S = 2K_S \mathbf{L}^{\mathrm{v}}_{ijkl} + 2\mu_S \mathbf{L}^{\mathrm{d}}_{ijkl} \tag{3. 22}$$

where K_S and μ_S are the bulk modulus and the shear modulus of the interface, respectively, and

$$\mathbf{L}^{\mathrm{v}}_{ijkl} = \frac{1}{2}\delta_{ij}\delta_{kl}\mathbf{e}_i \otimes \mathbf{e}_j \otimes \mathbf{e}_k \otimes \mathbf{e}_l$$

$$\mathbf{L}^{\mathrm{d}}_{ijkl} = \frac{1}{2}\left(\delta_{ik}\delta_{jl} + \delta_{jk}\delta_{il} - \delta_{ij}\delta_{kl}\right)\mathbf{e}_i \otimes \mathbf{e}_j \otimes \mathbf{e}_k \otimes \mathbf{e}_l$$

Now, the interface stress is related to the interface strain, which is composed of the tangential components of the total strain in the abutting material. Substitution of Eq. (3.21) into Eq. (3.20) renders

$$\mathbf{C}_0 : (\boldsymbol{\varepsilon}^{\lambda} + \boldsymbol{\varepsilon}^{*}) = -\nabla_S \cdot (\mathbf{C}^S : \boldsymbol{\varepsilon}^S) \tag{3. 23}$$

The interface strain $\boldsymbol{\varepsilon}^S$ can be determined when the total strain at the interface is obtained. Therefore, the interfacial strain discontinuity can be solved from Eq. (3.23), and the stress and the strain fields are related between the matrix and the inclusion. Further, the homogenization methods in classical micromechanics frameworks can be employed to predict the overall effective elastic

moduli of the composite. In the next section, the direct Eshelby method, the Mori-Tanaka method and the self-consistent method are followed in the determination of effective elastic moduli.

3.4 Effective Elastic Moduli of the Composite

The interfacial strain discontinuity tensor $\overline{\boldsymbol{\varepsilon}}^{\lambda}$ can be solved from Eq. (3.23) as follows

$$\overline{\boldsymbol{\varepsilon}}^{\lambda} = \hat{\mathbf{A}} : \hat{\boldsymbol{\varepsilon}}^{0} + \hat{\mathbf{B}} : \boldsymbol{\varepsilon}^{*} \tag{3. 24}$$

where $\hat{\mathbf{A}}$ and $\hat{\mathbf{B}}$ are the isotropic coefficient tensors,

$$\begin{aligned} &\hat{\mathbf{A}} = \left(3\hat{A}_b, 2\hat{A}_s\right) \quad \hat{A}_b = \frac{4}{9}\frac{K_S}{a\left(\hat{K}_0 + \frac{4}{3}\hat{\mu}_0\right)} \qquad \hat{A}_s = -\frac{2}{15}\frac{K_S}{a\left(\hat{K}_0 + \frac{4}{3}\hat{\mu}_0\right)} + \frac{1}{5}\frac{K_S}{a\hat{\mu}_0} + \frac{2}{5}\frac{\mu_S}{a\hat{\mu}_0} \\ &\hat{\mathbf{B}} = \left(3\hat{B}_b, 2\hat{B}_s\right) \quad \hat{B}_b = -\frac{1}{3}\frac{\hat{K}_0}{\hat{K}_0 + \frac{4}{3}\hat{\mu}_0} \qquad \hat{B}_s = -\frac{2}{15}\frac{\hat{\mu}_0}{\hat{K}_0 + \frac{4}{3}\hat{\mu}_0} - \frac{1}{5} \end{aligned} \tag{3. 25}$$

The detailed step-by-step solution of $\overline{\boldsymbol{\varepsilon}}^{\lambda}$ is demonstrated in Appendix I.

Now consider a *r*th phase particle in the composite. According to the equivalence principle, we have

$$\mathbf{C}_r : \boldsymbol{\varepsilon}_r = \hat{\mathbf{C}}_0 : \mathbf{e}_r \tag{3. 26}$$

where $\boldsymbol{\varepsilon}_r$ and $\mathbf{e}_r$ are the total strain and the elastic strain in the particle, respectively. Assume that the interface energy has uniform effect on the strain field in the particle. As a consequence, the total strain in the particle can be solved as

$$\boldsymbol{\varepsilon}_r = \hat{\boldsymbol{\varepsilon}}^{0} - \overline{\boldsymbol{\varepsilon}}_r^{\lambda} \tag{3. 27}$$

where $\boldsymbol{\varepsilon}_r^{\lambda}$ is the interfacial strain discontinuity tensor for the *r*th phase particles. The elastic strain in the original domain of the particle can be expressed as

$$\mathbf{e}_r = \hat{\boldsymbol{\varepsilon}}^0 - \overline{\boldsymbol{\varepsilon}}_r^{\lambda} - \boldsymbol{\varepsilon}_r^* \tag{3. 28}$$

Substitution of Eqs. (3.27)–(3.78) into Eq. (3.26) gives

$$\mathbf{C}_r : \left(\hat{\boldsymbol{\varepsilon}}_0 - \overline{\boldsymbol{\varepsilon}}^{\lambda}\right) = \hat{\mathbf{C}}_0 : \left(\hat{\boldsymbol{\varepsilon}}_0 - \overline{\boldsymbol{\varepsilon}}^{\lambda} - \boldsymbol{\varepsilon}_r^*\right) \tag{3. 29}$$

Further, from Eqs. (3.24) and (3.29),

$$\mathbf{C}_r : \left(\hat{\boldsymbol{\varepsilon}}_0 - \hat{\mathbf{A}} : \hat{\boldsymbol{\varepsilon}}_0 - \hat{\mathbf{B}} : \boldsymbol{\varepsilon}_r^*\right) = \hat{\mathbf{C}}_0 : \left(\hat{\boldsymbol{\varepsilon}}_0 - \hat{\mathbf{A}} : \hat{\boldsymbol{\varepsilon}}_0 - \hat{\mathbf{B}} : \boldsymbol{\varepsilon}_r^* - \boldsymbol{\varepsilon}_r^*\right) \tag{3. 30}$$

and $\boldsymbol{\varepsilon}^*$ can be solved as

$$\boldsymbol{\varepsilon}^* = \left[\left(\mathbf{I} + \hat{\mathbf{B}}\right) - \hat{\mathbf{C}}_0^{-1} : \mathbf{C}_r : \hat{\mathbf{B}}\right]^{-1} : \left[\left(\mathbf{I} - \hat{\mathbf{C}}_0^{-1} : \mathbf{C}_r\right) : \left(\mathbf{I} - \hat{\mathbf{A}}\right)\right] : \hat{\boldsymbol{\varepsilon}}_0 \tag{3. 31}$$

To predict the overall effective moduli, the homogenization procedures in classical micromechanics theories are adopted. Following the direct Eshelby Method,

$$\hat{\boldsymbol{\varepsilon}}_0 = \boldsymbol{\varepsilon}_0 \quad \text{and} \quad \hat{\mathbf{C}}_0 = \mathbf{C}_0 \tag{3. 32}$$

Consequently, we have

$$\hat{\mathbf{A}} = \mathbf{A} \quad \text{and} \quad \hat{\mathbf{B}} = \mathbf{B} \tag{3. 33}$$

The relation between the total strain $\boldsymbol{\varepsilon}_r$ in the particle and the effective strain $\hat{\boldsymbol{\varepsilon}}^0$ in matrix under Eshelby's assumptions is obtained from Eqs. (3.24), (3.28) and (3.31)

$$\boldsymbol{\varepsilon}_r = \left\{\mathbf{I} - \mathbf{A} - \mathbf{B} : \left[\left(\mathbf{I} + \mathbf{B}\right) - \mathbf{C}_0^{-1} : \mathbf{C}_r : \mathbf{B}\right]^{-1} : \left[\left(\mathbf{I} - \mathbf{C}_0^{-1} : \mathbf{C}_r\right) : \left(\mathbf{I} - \mathbf{A}\right)\right]\right\} : \boldsymbol{\varepsilon}_0 \tag{3. 34}$$

from which the strain concentration tensor reveals to be

$$\mathbf{N}_r = \left\{\mathbf{I} - \mathbf{A} - \mathbf{B} : \left[\left(\mathbf{I} + \mathbf{B}\right) - \mathbf{C}_0^{-1} : \mathbf{C}_r : \mathbf{B}\right]^{-1} : \left[\left(\mathbf{I} - \mathbf{C}_0^{-1} : \mathbf{C}_r\right) : \left(\mathbf{I} - \mathbf{A}\right)\right]\right\} \tag{3. 35}$$

and the effective elastic stiffness tensor is

$$\overline{\mathbf{C}} = \mathbf{C}_0 + \sum_{r=1}^{n} \phi_r \left(\mathbf{C}_r - \mathbf{C}_0\right)\left\{\mathbf{I} - \mathbf{A} - \mathbf{B} : \left[\left(\mathbf{I} + \mathbf{B}\right) - \mathbf{C}_0^{-1} : \mathbf{C}_r : \mathbf{B}\right]^{-1} : \left[\left(\mathbf{I} - \mathbf{C}_0^{-1} : \mathbf{C}_r\right) : \left(\mathbf{I} - \mathbf{A}\right)\right]\right\} \tag{3. 36}$$

When a *two*-phase composite is considered, the effective elastic stiffness tensor can be written as,

$$\overline{\mathbf{C}} = \mathbf{C}_0 + \phi_1 (\mathbf{C}_1 - \mathbf{C}_0) \left\{ \mathbf{I} - \mathbf{A} - \mathbf{B} : \left[(\mathbf{I} + \mathbf{B}) - \mathbf{C}_0^{-1} : \mathbf{C}_1 : \mathbf{B} \right]^{-1} : \left[\left(\mathbf{I} - \mathbf{C}_0^{-1} : \mathbf{C}_1 \right) : (\mathbf{I} - \mathbf{A}) \right] \right\} \quad (3.37)$$

Accordingly, the effective bulk modulus and the effective shear modulus can be expressed as,

$$\overline{K} = K_0 + \frac{\phi_1 (K_1 - K_0)(3K_0 + 4\mu_0)}{3K_1 + 4\mu_0} - \frac{4\phi_1 (K_1 - K_0) K_S}{a(3K_1 + 4\mu_0)} \quad (3.38)$$

$$\begin{aligned} \overline{\mu} = \mu_0 &+ \frac{5\phi_1 \mu_0 (\mu_1 - \mu_0)(3K_0 + 4\mu_0)}{3K_0(3\mu_0 + 2\mu_1) + 4\mu_0(2\mu_0 + 3\mu_1)} \\ &- \frac{2\phi_1 K_S (\mu_1 - \mu_0)(3K_0 + 2\mu_0)}{a\left[3K_0(3\mu_0 + 2\mu_1) + 4\mu_0(2\mu_0 + 3\mu_1)\right]} - \frac{4\phi_1 \mu_S (\mu_1 - \mu_0)(3K_0 + 4\mu_0)}{a\left[3K_0(3\mu_0 + 2\mu_1) + 4\mu_0(2\mu_0 + 3\mu_1)\right]} \end{aligned} \quad (3.39)$$

It is observed that the first two terms in the bulk modulus and the shear modulus are the equal to the bulk modulus and the shear modulus of the micromechanical solution of the direct Eshelby method, and the additional terms are related to the interface stiffness and the radius of the particles.

Following the Mori-Tanaka method, effective moduli can be solved similarly. Different from the direct Eshelby method, Mori and Tanaka considered the far-field interactions by assuming

$$\hat{\boldsymbol{\varepsilon}}_0 = \overline{\boldsymbol{\varepsilon}}_0 \quad \text{and} \quad \hat{\mathbf{C}}_0 = \mathbf{C}_0 \quad (3.40)$$

Consequently,

$$\hat{\mathbf{A}} = \mathbf{A} \quad \text{and} \quad \hat{\mathbf{B}} = \mathbf{B} \quad (3.41)$$

Based on the assumptions made by Mori and Tanaka, the total strain in the *r*th phase particles is related to the volume-averaged strain in the matrix as follows

$$\boldsymbol{\varepsilon}_r = \left\{ \mathbf{I} - \mathbf{A} - \mathbf{B} : \left[(\mathbf{I} + \mathbf{B}) - \mathbf{C}_0^{-1} : \mathbf{C}_r : \mathbf{B} \right]^{-1} : \left[\left(\mathbf{I} - \mathbf{C}_0^{-1} : \mathbf{C}_r \right) : (\mathbf{I} - \mathbf{A}) \right] \right\} : \overline{\boldsymbol{\varepsilon}}_0 \quad (3.42)$$

where the local strain concentration tensor is

$$\mathbf{G}_r = \left\{ \mathbf{I} - \mathbf{A} - \mathbf{B} : \left[(\mathbf{I} + \mathbf{B}) - \mathbf{C}_0^{-1} : \mathbf{C}_r : \mathbf{B} \right]^{-1} : \left[\left(\mathbf{I} - \mathbf{C}_0^{-1} : \mathbf{C}_r \right) : (\mathbf{I} - \mathbf{A}) \right] \right\} \tag{3. 43}$$

The volume-averaged strain in the composite is

$$\overline{\boldsymbol{\varepsilon}} = \phi_0 \overline{\boldsymbol{\varepsilon}}_0 + \sum_{r=1}^{N} \phi_r \overline{\boldsymbol{\varepsilon}}_r = \left[\phi_0 \mathbf{I} + \sum_{r=1}^{N} \phi_r \mathbf{G}_r \right] : \overline{\boldsymbol{\varepsilon}}_0 \tag{3. 44}$$

which leads to

$$\overline{\boldsymbol{\varepsilon}}_0 = \left[\phi_0 \mathbf{I} + \sum_{r=1}^{N} \phi_r \mathbf{G}_r \right]^{-1} : \overline{\boldsymbol{\varepsilon}} \tag{3. 45}$$

Substitution of Eq. (3.42) into Eq. (3.45) yields,

$$\boldsymbol{\varepsilon}_r = \mathbf{G}_r : \left[\phi_0 \mathbf{I} + \sum_{r=1}^{n} \phi_r \mathbf{G}_r \right]^{-1} : \overline{\boldsymbol{\varepsilon}} \tag{3. 46}$$

where the global strain concentration tensor is obtained

$$\begin{aligned} \mathbf{N}_r &= \mathbf{G}_r : \left[\phi_0 \mathbf{I} + \sum_{r=1}^{n} \phi_r \mathbf{G}_r \right]^{-1} \\ &= \left\{ \mathbf{I} - \mathbf{A} - \mathbf{B} : \left[(\mathbf{I} + \mathbf{B}) - \mathbf{C}_0^{-1} : \mathbf{C}_r : \mathbf{B} \right]^{-1} : \left[\left(\mathbf{I} - \mathbf{C}_0^{-1} : \mathbf{C}_r \right) : (\mathbf{I} - \mathbf{A}) \right] \right\} \\ &\quad : \left[\phi_0 \mathbf{I} + \sum_{r=1}^{n} \phi_r \left\{ \mathbf{I} - \mathbf{A} - \mathbf{B} : \left[(\mathbf{I} + \mathbf{B}) - \mathbf{C}_0^{-1} : \mathbf{C}_r : \mathbf{B} \right]^{-1} : \left[\left(\mathbf{I} - \mathbf{C}_0^{-1} : \mathbf{C}_r \right) : (\mathbf{I} - \mathbf{A}) \right] \right\} \right] \end{aligned} \tag{3. 47}$$

Consequently, the effective elastic tensor is exhibited as

$$\begin{aligned} \overline{\mathbf{C}} &= \mathbf{C}_0 + \sum_{r=1}^{n} \phi_r \left(\mathbf{C}_r - \mathbf{C}_0 \right) \mathbf{N}_r \\ &= \mathbf{C}_0 + \sum_{r=1}^{n} \phi_r \left(\mathbf{C}_r - \mathbf{C}_0 \right) \left\{ \mathbf{I} - \mathbf{A} - \mathbf{B} : \left[(\mathbf{I} + \mathbf{B}) - \mathbf{C}_0^{-1} : \mathbf{C}_r : \mathbf{B} \right]^{-1} : \left[\left(\mathbf{I} - \mathbf{C}_0^{-1} : \mathbf{C}_r \right) : (\mathbf{I} - \mathbf{A}) \right] \right\} \\ &\quad : \left[\phi_0 \mathbf{I} + \sum_{m=1}^{n} \phi_m \left\{ \mathbf{I} - \mathbf{A} - \mathbf{B} : \left[(\mathbf{I} + \mathbf{B}) - \mathbf{C}_0^{-1} : \mathbf{C}_m : \mathbf{B} \right]^{-1} : \left[\left(\mathbf{I} - \mathbf{C}_0^{-1} : \mathbf{C}_m \right) : (\mathbf{I} - \mathbf{A}) \right] \right\} \right] \end{aligned} \tag{3. 48}$$

Now, consider a *two*-phase composite material. The effective elastic modulus can be written as

$$\begin{aligned}\bar{\mathbf{C}} &= \mathbf{C}_0 + \phi_1(\mathbf{C}_1 - \mathbf{C}_0)\mathbf{N}_1 \\ &= \mathbf{C}_0 + \phi_1(\mathbf{C}_1 - \mathbf{C}_0)\left\{\mathbf{I} - \mathbf{A} - \mathbf{B} : \left[(\mathbf{I}+\mathbf{B}) - \mathbf{C}_0^{-1} : \mathbf{C}_1 : \mathbf{B}\right]^{-1} : \left[\left(\mathbf{I} - \mathbf{C}_0^{-1} : \mathbf{C}_1\right) : (\mathbf{I} - \mathbf{A})\right]\right\} \\ &\quad : \left[(1-\phi_1)\mathbf{I} + \phi_1\left\{\mathbf{I} - \mathbf{A} - \mathbf{B} : \left[(\mathbf{I}+\mathbf{B}) - \mathbf{C}_0^{-1} : \mathbf{C}_1 : \mathbf{B}\right]^{-1} : \left[\left(\mathbf{I} - \mathbf{C}_0^{-1} : \mathbf{C}_1\right) : (\mathbf{I} - \mathbf{A})\right]\right\}\right]\end{aligned} \tag{3. 49}$$

and the corresponding effective elastic moduli of the composite are

$$\bar{K} = K_0 + \frac{\phi_1(K_1 - K_0)(3K_0 + 4\mu_0) - \frac{4}{a}\phi_1(K_1 - K_0)K_S}{3K_0 + 4\mu_0 + 3(1-\phi_1)(K_1 - K_0) - \frac{4}{a}\phi_1 K_S} \tag{3. 50}$$

$$\bar{\mu} = \mu_0 + \frac{5\phi_1\mu_0(\mu_1 - \mu_0)(3K_0 + 4\mu_0) - \phi_1(\mu_1 - \mu_0)\left[\frac{2}{a}K_S(3K_0 + 2\mu_0) + \frac{4}{a}\mu_S(3K_0 + 4\mu_0)\right]}{5\mu_0(3K_0 + 4\mu_0) + 6(1-\phi_1)(\mu_1 - \mu_0)(K_0 + 2\mu_0) - \phi_1\left[\frac{2}{a}K_S(3K_0 + 2\mu_0) + \frac{4}{a}\mu_S(3K_0 + 4\mu_0)\right]} \tag{3. 51}$$

If the K_S and μ_S related terms are dropped, the above effective elastic moduli is identical to the micromechanical effective elastic moduli predicted by the Mori-Tanaka method, where the interface energy effect is neglected.

3.5 Discussions

In this section, the interface energy effect on the effective elastic moduli of the *two*-phase composite containing spherical nano-voids are discussed. The effective elastic moduli of the two-phase composite materials are presented in Eqs. (3.38)–(3.39) following the direct Eshelby method and in Eqs. (3.50)–(3.51) following the Mori-Tanaka method. For the two-phase composite containing nano-voids, the effective moduli are obtained by letting $K_1 = 0$ and $\mu_1 = 0$, and the effective elastic moduli following the direct Eshelby method become

$$\bar{K} = K_0 - \frac{\phi_1 K_0 \left(3K_0 + 4\mu_0\right)}{4\mu_0} - \frac{\phi_1 K_0 K_S}{2a\mu_0} \tag{3.52}$$

$$\bar{\mu} = \mu_0 - \frac{5\phi_1 {\mu_0}^2 \left(3K_0 + 4\mu_0\right)}{9K_0\mu_0 + 8{\mu_0}^2} + \frac{2\phi_1 K_S \mu_0 \left(3K_0 + 2\mu_0\right)}{a\left(9K_0\mu_0 + 8{\mu_0}^2\right)} + \frac{4\phi_1 \mu_0 \mu_S \left(3K_0 + 4\mu_0\right)}{a\left(9K_0\mu_0 + 8{\mu_0}^2\right)} \tag{3.53}$$

Additionally, the micromechanical direct Eshelby solutions are

$$\bar{K} = K_0 - \frac{\phi_1 K_0 \left(3K_0 + 4\mu_0\right)}{4\mu_0} \tag{3.54}$$

$$\bar{\mu} = \mu_0 - \frac{5\phi_1 {\mu_0}^2 \left(3K_0 + 4\mu_0\right)}{9K_0\mu_0 + 8{\mu_0}^2} \tag{3.55}$$

Comparing the solutions with and without considering the interface energy effect, we notice that the interface energy effect induces additional terms in the elastic moduli. The additional terms depend on the size and volume fraction of the voids, the elastic moduli of the interface and the elastic moduli of the matrix.

By substituting $K_1 = 0$ and $\mu_1 = 0$ into Eqs. (3.50)–(3.51), the effective moduli of a two-phase composite containing nano-voids can be displayed as

$$\bar{K} = K_0 - \frac{\phi_1 K_0 \left(3K_0 + 4\mu_0\right) - \frac{4}{a}\phi_1 K_0 K_S}{3K_0 + 4\mu_0 - 3\left(1-\phi_1\right)K_0 - \frac{4}{a}\phi_1 K_S} \tag{3.56}$$

$$\bar{\mu} = \mu_0 + \frac{-5\phi_1 {\mu_0}^2 \left(3K_0 + 4\mu_0\right) + \phi_1 \mu_0 \left[\frac{2}{a} K_S \left(3K_0 + 2\mu_0\right) + \frac{4}{a}\mu_S \left(3K_0 + 4\mu_0\right)\right]}{5\mu_0 \left(3K_0 + 4\mu_0\right) - 6\left(1-\phi_1\right)\mu_0 \left(K_0 + 2\mu_0\right) - \phi_1 \left[\frac{2}{a} K_S \left(3K_0 + 2\mu_0\right) + \frac{4}{a}\mu_S \left(3K_0 + 4\mu_0\right)\right]} \tag{3.57}$$

and the micromechanical Mori-Tanaka solutions are

$$\bar{K} = K_0 - \frac{\phi_1 K_0 \left(3K_0 + 4\mu_0\right)}{3K_0 + 4\mu_0 - 3\left(1-\phi_1\right)K_0} \tag{3.58}$$

$$\bar{\mu} = \mu_0 - \frac{5\phi_1\mu_0{}^2\left(3K_0 + 4\mu_0\right)}{5\mu_0\left(3K_0 + 4\mu_0\right) - 6\left(1-\phi_1\right)\mu_0\left(K_0 + 2\mu_0\right)} \tag{3. 59}$$

Similarly, it is observed that additional terms are induced in the effective elastic moduli by considering the interface energy effect.

Next, numerical calculations are presented for the *two*-phase composite with nano-voids. The aluminum matrix is considered. The bulk modulus of aluminum K_0=75.2 GPa and the shear modulus μ_0=34.7 GPa. The interface between the matrix and a void is the free-surface. Miller and Shenoy (2000) determined the free surface properties by the molecular dynamic simulations, which are adopted here for illustration:

$$\textit{Interface } 1\text{:}\quad K_S = -5.457\,N/m \quad \mu_S = -6.2178\,N/m$$

$$\textit{Interface } 2\text{:}\quad K_S = 12.932\,N/m \quad \mu_S = -0.3755\,N/m$$

Now define the specific effective bulk modulus $\bar{K}_{specific}$ and the specific effective shear modulus $\bar{\mu}_{specific}$ as

$$\bar{K}_{specific} = \frac{\left(\bar{K}\right)_{nano}}{\left(\bar{K}\right)_{micro}} \quad \text{and} \quad \bar{\mu}_{specific} = \frac{\left(\bar{\mu}\right)_{nano}}{\left(\bar{\mu}\right)_{micro}} \tag{3. 60}$$

where $(\cdot)_{nano}$ represents the solution that considers the interface energy effect and $(\cdot)_{micro}$ is the classical micromechanical solution. Fig. 3.2–3.5 depict the change of the specific elastic moduli with the change of the radius of the spherical voids, where the volume fraction of the voids is 0.3. The interface energy effect continues to decrease as the radius of the voids increases and becomes negligible when the radius is larger than 50nm. However, due to the different assumptions on the effective matrix, large differences are observed on the effect of the interface energy between the

effective elastic moduli solved following the direct Eshelby method and following the Mori-Tanaka method.

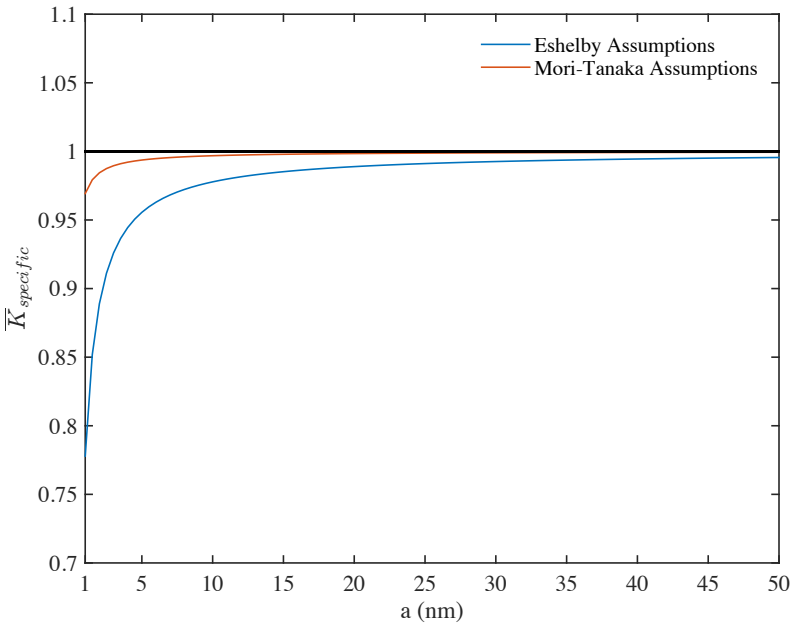

Figure 3–2 The specific effective bulk modulus vs. the radius of the voids (interface 1)

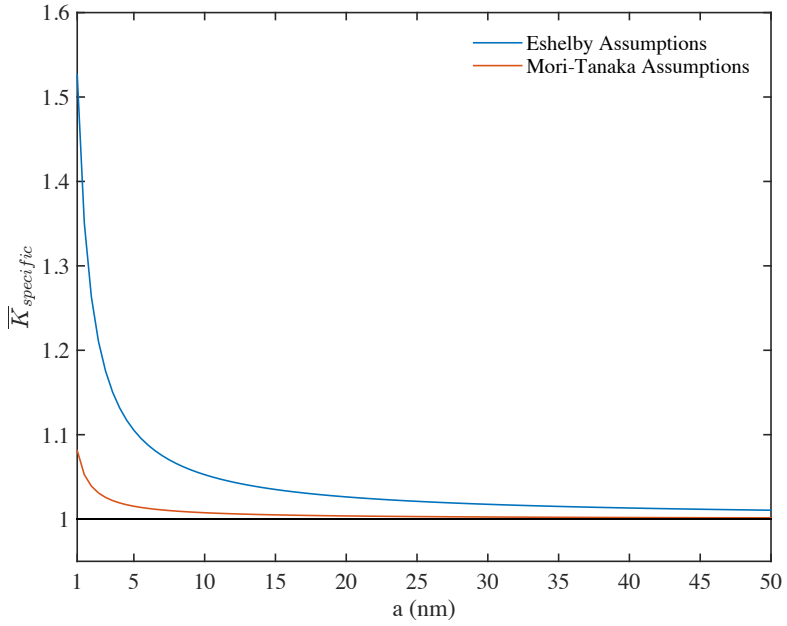

Figure 3–3 The specific effective bulk modulus vs. the radius of the voids (interface 2)

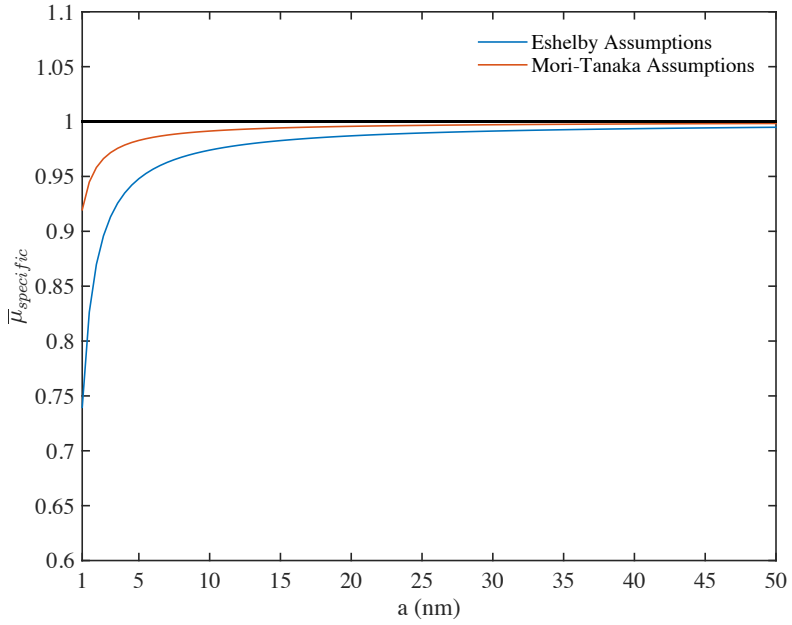

Figure 3–4 The specific effective shear modulus vs. the radius of the voids (interface 1)

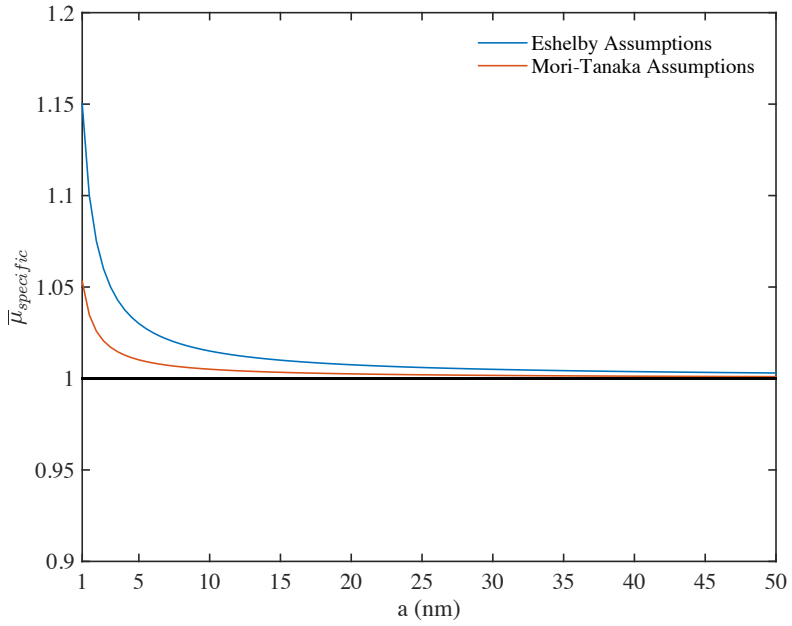

Figure 3–5 The specific effective shear modulus vs. the radius of the voids (interface 2)

The dependence of the interface energy effect upon the volume fraction of the voids is presented in Fig. 3.6–3.9. The effective moduli corresponding to the volume fractions of 0.05, 0.1, 0.15, 0.2, 0.25 and 0.3 are compared. It is recognized that the interface energy effect on the effective elastic moduli increases with the increasing of the volume fraction.

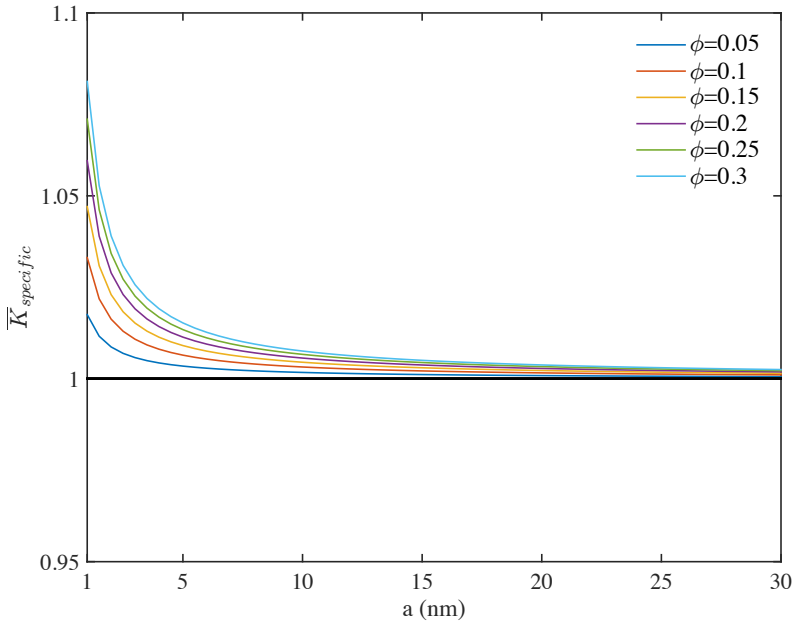

Figure 3–6 The specific effective bulk modulus vs. the volume fraction of the voids (interface 1)

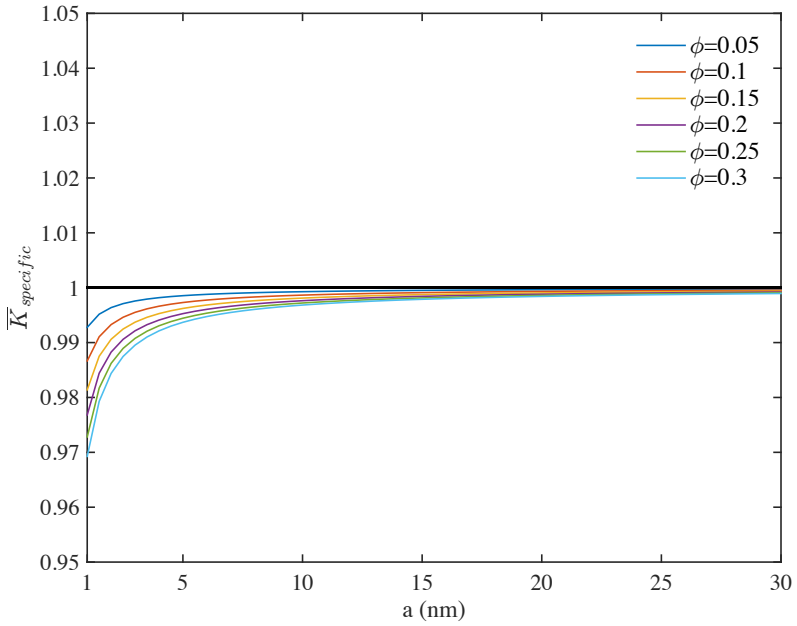

Figure 3–7 The specific effective bulk modulus vs. the volume fraction of the voids (interface 2)

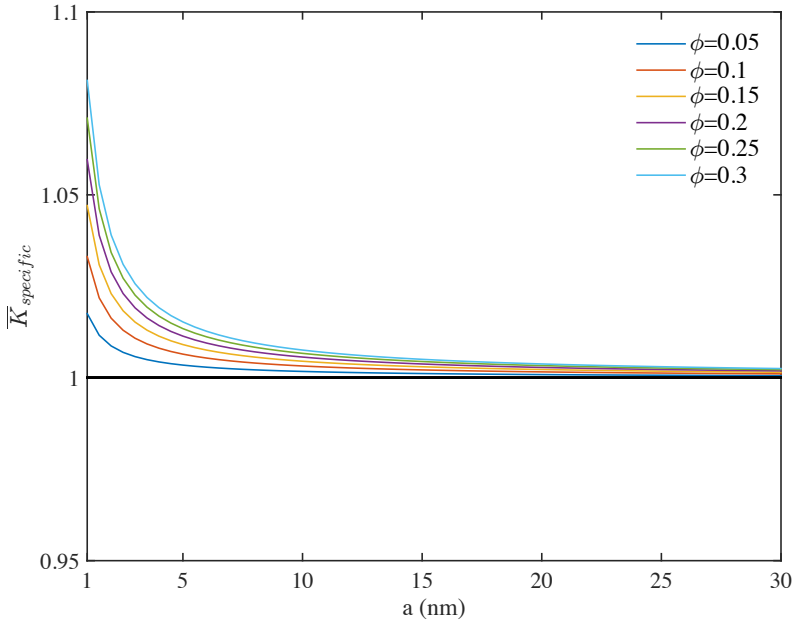

Figure 3–8 The specific effective shear modulus vs. the volume fraction of voids (interface 1)

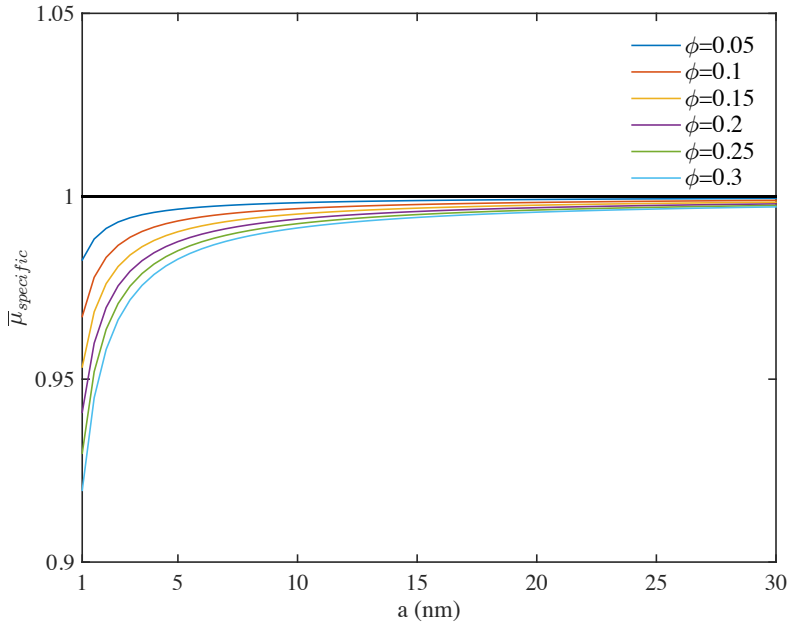

Figure 3–9 The specific effective shear modulus vs. the volume fraction of voids (interface 1)

Figure 3-10 and Figure 3-11 exhibit that, at the same particle size, the interface energy effect on the effective moduli is positively related to the volume fraction of the inhomogeneities. Moreover, at the same volume fraction, the interface energy effect is larger for the inhomogeneities with smaller radius. In summary, the interface energy effect on the effective elastic moduli is demonstrated to be positively related to the total interface area in the composite.

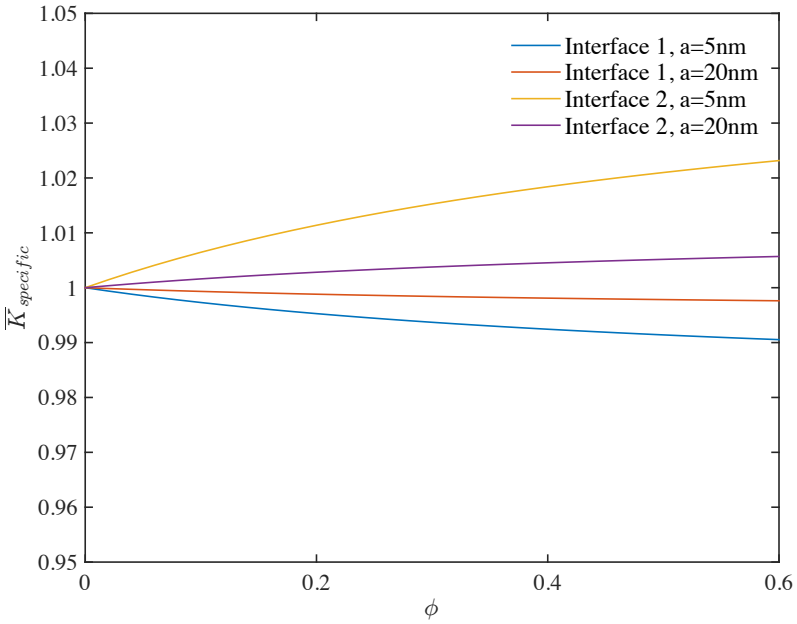

Figure 3–10 Effective bulk modulus as a function of void volume fraction

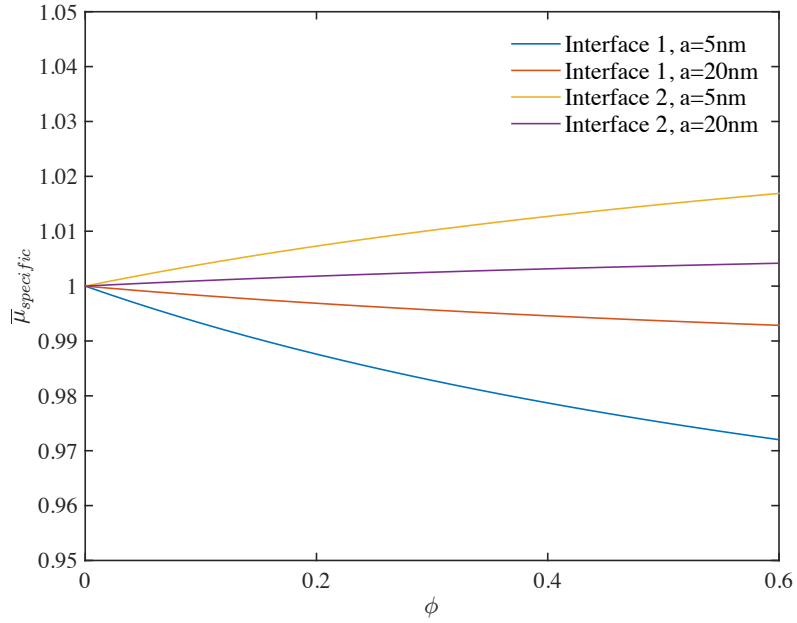

Figure 3–11 Effective shear modulus as a function of void volume fraction

3.6 Conclusions

In this chapter, the interface energy effect on the effective elastic moduli of the spherical particle reinforced composite is studied. The interface energy effect is simulated by the zero-thickness membrane interphase and the in-plane interface stress. Different from the micromechanical assumption of the perfect interface, discontinuity of the stress over the interface is considered in the present work. According to the boundary conditions at the interface, the interfacial strain discontinuity is determined, which is revealed to be related to the far-field applied strain and the eigenstrain of the equivalent inclusion. Accordingly, the effective elastic fields in the matrix and the particle are related. Next, following the assumptions in the direct Eshelby method and the Mori-Tanaka method, the effective elastic moduli of the spherical particle reinforced composites are solved by considering the interface energy effect. It is noticed that the interface energy effect induces extra terms on the effective moduli solved by classical micromechanics methods. The extra terms are shown to have particle size dependence and involve the interface properties. Based on the existing data of interface properties, a two-phase heterogeneous material containing nano-voids is investigated. Based on the illustrative figures of effective moduli with respect to void size and volume fraction, it is shown that interface energy effect increases with the increase of total interface area. Therefore, the size dependence can be interpreted as interface area dependence. And the volume fraction of inhomogeneities, the size of inhomogeneities are two factors that will influence the total area of interface.

3.7 References

Cammarata, Robert C., and Karl Sieradzki. "Surface and interface stresses." *Annual Review of Materials Science* 24.1 (1994): 215-234.

Chen, Tungyang, Min-Sen Chiu, and Chung-Ning Weng. "Derivation of the generalized Young-Laplace equation of curved interfaces in nanoscaled solids." Journal of Applied Physics 100.7 (2006): 074308.

Duan, H. L., Wang, J. X., Huang, Z. P., and Karihaloo, B. L.: Size-dependent effective elastic constants of solids containing nano-inhomogeneities with interface stress. J. Mech. Phys. Solids. 53, 1574-1596 (2005a)

Duan, H. L., Wang, J., Huang, Z. P., and Luo, Z. Y.: Stress concentration tensors of inhomogeneities with interface effects. Mech. Mater. 37(7), 723-736 (2005b)

Eshelby, J. D.: The determination of the elastic field of an ellipsoidal inclusion, and related problems. Proc. R. Soc. Lond. A, 241, 376-396 (1957)

Eshelby, J. D.: Elastic inclusion and inhomogeneities. Prog. Solid Mech. 2, 89-140 (1961)

Gibbs, Josiah Willard. The collected works of J. Willard Gibbs. Eds. Henry Andrews Bumstead, and William Raymond Longley. Vol. 1. Longmans, Green and Company, 1928.

Gurtin, Morton E., and A. Ian Murdoch. "A continuum theory of elastic material surfaces." Archive for Rational Mechanics and Analysis 57.4 (1975): 291-323.

Herring, Conyers. "The use of classical macroscopic concepts in surface energy problems."

Structure and properties of solid surfaces. 1953.

Ju, J. W., and Chen, T. M.: Micromechanics and effective moduli of elastic composites containing randomly dispersed ellipsoidal inhomogeneities. Acta Mech. 103, 103-121 (1994a)

Ju, J. W., and Chen, T. M.: Effective elastic moduli of two-phase composites containing randomly dispersed spherical inhomogeneities. Acta Mech. 103, 123-144 (1994b)

Larché, F. C., and J. W. Cahn. "Thermochemical equilibrium of multiphase solids under stress." Acta Metallurgica 26.10 (1978): 1579-1589.

Miller, Ronald E., and Vijay B. Shenoy. "Size-dependent elastic properties of nanosized structural elements." Nanotechnology 11.3 (2000): 139.

Mura, Toshio. Micromechanics of defects in solids. Springer Science & Business Media, 2013.

Miller, R. E., and Shenoy, V. B.: Size-dependent elastic properties of nanosized structural elements. Nanotechnology. 11, 139 (2000)

Mori, T., and Tanaka, K.: Average stress in matrix and average elastic energy of materials with misfitting inclusions. Acta Metall. 21, 571-574 (1973)

Murr, Lawrence Eugene. "Interfacial phenomena in metals and alloys." (1975).

Orowan, E. "Surface energy and surface tension in solids and liquids." Proceedings of the Royal Society of London A: Mathematical, Physical and Engineering Sciences. Vol. 316. No. 1527. The Royal Society, 1970.

Qu, Jianmin, and Mohammed Cherkaoui. Fundamentals of micromechanics of solids. Hoboken: Wiley, 2006.

Sharma, P., and Dasgupta, A.: Average elastic fields and scale-dependent overall properties of heterogeneous micropolar materials containing spherical and cylindrical inhomogeneities. Phys. Rev. B. 66, 224110 (2002)

Sharma, P., Ganti, S., and Bhate, N.: Effect of surfaces on the size-dependent elastic state of nano-inhomogeneities. Appl. Phys. Lett. 82, 535-537 (2003)

Sharma, P., and Ganti, S.: Size-dependent Eshelby's tensor for embedded nano-inclusions incorporating surface/interface energies. J. Appl. Mech. 71, 663-671 (2004)

Shuttleworth, Ro. "The surface tension of solids." Proceedings of the physical society. Section A 63.5 (1950): 444.

- Chapter 4 -

INTERFACE ENERGY EFFECT ON EFFECTIVE ELASTIC MODULI OF SPHEROIDAL PARTICLE REINFORCED NANOCOMPOSITES

Abstract

By incorporating the interface energy effect into classical micromechanics framework, effective elastic moduli of the composite material containing randomly distributed nanosized prolate spheroidal inhomogeneities are investigated in this chapter. The effect of interface energy, which is usually neglected in classical micromechanics theories, becomes important when the size of reinforcement phase in the composite enters the nanometer range. The interface energy effect is simulated by inducing interface stress on the zero-thickness membrane interface between the matrix and the inhomogeneities. The interfacial stress discontinuity equations are formulated in accordance with the equilibrium conditions on the idealized interface, from which the interfacial strain discontinuity is solved. Subsequently, the effective elastic moduli are derived basing on the classical micromechanics homogenization approaches. Comparisons are made between the effective moduli solved under the current nanomechanical framework and the classical micromechanical theory. The effective moduli are exhibited to be dependent upon the size of the inhomogeneities and the interface properties when the interface energy effect is considered.

4.1 Introduction

The advancement of material science in nanotechnology provides new insights into particles in nanoscale and has attracted considerable attention in a wide range of disciplines such as astronomy, medicine, electronics and optics, etc. (Wood, 2008). Nanoparticles, having one or more dimensions in nanometer scale, may possess desirable properties different from conventional materials due to their greater specific surface areas. Currently, scientists attempt to use nanoparticles as the reinforcement phase in composite materials to create new materials with improved properties, such as high strengths, high moduli, high heat resistance, low gas permeability and low flammability (Giannelis, 1996; Ray and Okamoto, 2003). Meanwhile, predictions on the mechanical properties of nanocomposites have drawn significant attention. As nanocomposites are heterogeneous materials consisting of phases with distinctive properties and length scales, it is impractical to find the point-wise mechanical properties of a random material point. Instead, a common practice is to consider the overall effective properties of a heterogeneous composite. For composites with large-sized reinforcement (typically in the micrometer or larger scale), classical micromechanics theories have exhibited good predictions on the effective mechanical properties; e.g., the direct Eshelby method (Eshelby, 1957; Eshelby, 1961) for dilute particle concentration, the Mori-Tanaka method (Mori and Tanaka, 1973) for moderate concentration, and the pairwise particle interaction model (Ju and Chen, 1994a, b) for moderately high particle concentration. In this chapter, the homogenization scheme of the classical

micromechanics theory, the Mori-Tanaka method (Mori and Tanaka, 1973) or the first-order non-interacting method (Ju and Chen, 1994a, b), is incorporated into the determination of the effective properties of nanocomposites.

It is well known that the local atomic environment at the particle-matrix interface is different from its setting associated with the interior. As a consequence, the free energies possessed by the molecules at the particle-matrix interface and by the molecules in the interior are different. Gibbs, who first pointed out this phenomenon in 1906, proposed the concept of interface energy as the excess free energy per unit area of the interface (Gibbs, 1906). As the mechanical properties of a solid are related to its associated free energy, they are affected by the interface energy at the interface (Duan et al., 2005a). In classical micromechanics theories, the effect of interface energy is neglected because of the relatively low specific interface area as well as the small gross interface area in the composite. However, when one or more dimensions of a solid phase is (are) in nanoscale, the interface energy becomes one of the main factors that determine the material properties of a composite including its mechanical performances (Cammarata, 1997). For a nanocomposite, since the dimensions of the inhomogeneities are in the nanometer scale, the effect of interface energy needs to be considered. To characterize the interface energy effect on the mechanical properties, several models are proposed in the literature; among them, the interphase model and the interface model are most widely discussed. The interphase model (Walpole, 1978; Mikata and Taya, 1985; Qiu and Weng, 1991; Herve and Zaoui, 1993) assumes that there exists a layer between the matrix and an inhomogeneity, which is referred to as the interphase. The interphase transfers the loading

from the matrix to an inhomogeneity, and it can be regarded as a separate phase with a specified thickness and mechanical properties. On the other hand, the interface model, originated from the classical treatments for the imperfect bonding conditions in composite materials, assumes discontinuous stress and/or displacement from the matrix to an inhomogeneity; e.g., the free tangential interface sliding in the free sliding model, the linear displacement-traction relation in the linear spring model, and the linear relationship between the displacements on the two sides of the interface in the dislocation-like model (Duan et al., 2005b).

In the study of capillarity, the interface energy is exhibited to be equal to the surface tension (the interface stress) *numerically* under certain occasions, and they are often wrongly regarded as equivalent (Shuttleworth, 1950). However, Gibbs (1906) distinguished these two concepts by the thermodynamics approach. He defined the interface stress as the reversible work required to elastically stretch an existing interface. In order to study the mechanical behavior of material surfaces, Gurtin and Murdoch (Gurtin and Murdoch, 1975) established a mathematical framework for the material surfaces following the continuum mechanics theory. The formulation is based on the interphase model, in which the thickness of the interphase is set to be *zero*. As a consequence, the membrane theory applies, and only in-plane forces are retained in the idealized zero-thickness interphase. According to the elastic theory of membranes, Gurtin and Murdoch (1975) assumed continuous displacements but discontinuous stress at the interface by inducing the in-plane interface stress. The corresponding interface boundary conditions, which involve the interface stress terms, are named the *generalized* Young-Laplace equations, as a counterpart of the well-

known Young-Laplace equations in fluid mechanics. The *generalized* Young-Laplace equations can be expressed as:

$$[\boldsymbol{\sigma}]\cdot\mathbf{n} = -\nabla_S \cdot \boldsymbol{\tau} \tag{4.1}$$

where $[\boldsymbol{\sigma}]$ denotes the difference of stress at the interface between the matrix and the reinforcement, $\mathbf{n}$ is the outward unit normal to the interface, and $-\nabla_S \cdot \boldsymbol{\tau}$ is the surface divergence of the interface stress $\boldsymbol{\tau}$. In the following expressions, **[.]** represents the discontinuity of said value at the interface from the matrix to the inhomogeneity. From the *generalized* Young-Laplace equations, relations of the elastic fields at the interface between the matrix and the inhomogeneity can be determined.

Recently, some researchers have studied the mechanical properties of nanostructured elements, such as nanosized plates and beams (Miller and Shenoy, 2000), spherical nanoparticles, thin films and nanowires (Dingreville et al., 2005; Wang et al., 2010). However, only a few researchers focus on the effective mechanical properties of nanocomposites, and experimental data are especially rare in the literature. Sharma et al. (2003) included the interface energy in the total free energy and rendered a variational formulation to determine the stress and the strain states for the composite containing a single spherical nano-inclusion, in which dilatational eigenstrain is assumed. Sharma and Ganti (2004) proposed a revised size-dependent Eshelby tensor that considers the interface energy effect and presented its expressions for spherical and cylindrical inclusions with dilatational eigenstrain. Duan et al. (2005a) addressed the spherical nano-inhomogeneity problem and predicted the effective moduli of the nanocomposite. Shodja and Hashemian (2019) adopted the

couple stress theory to consider the size effect in nanocomposites. In addition to the research on the elastic behavior, the performances of nanocomposites under damage are discussed (Heidarhaei, 2018; Rostamiyan and Ferasat, 2017; Fan et al., 2017; Voyiadjis and Kattan, 2019). Nevertheless, most of the existing approaches tackle the nanocomposite with spherical or cylindrical reinforcements, studies on the more general and more sophisticated spheroidal particle reinforced nanocomposites are demanded.

In this chapter, an analytical framework is proposed to predict the effective elastic moduli of prolate spheroidal particle reinforced nanocomposites. The present framework is based on the classical micromechanics theories and considers the interface energy effect. At variance from the conventional perfect interface boundary conditions, which are assumed in micromechanics theories, the *generalized* Young-Laplace equations are incorporated at the interface to account for the interface energy-induced interfacial discontinuities. The interfacial strain discontinuity is solved for spheroidal particles. Further, effective moduli are derived following the homogenization approach in the Mori-Tanaka method. Compared with the classical micromechanical solutions on the effective moduli, the results are demonstrated to be dependent upon the size of the reinforcement particles and the properties of the interface.

4.2 Interface Discontinuity Conditions for Spheroids

Following Gurtin and Murdoch (1975), the interface energy effect is simulated by the *generalized* Young-Laplace equations. For a prolate spheroidal particle, we have

$$\frac{r^2}{b^2}+\frac{z^2}{a^2}=1, \qquad 0\le\phi\le 2\pi, \quad a>b \tag{4.2}$$

The *generalized* Young-Laplace equations are (Chen et al., 2006)

$$\left[\sigma_{31}\right]=-\frac{1}{h_1h_2}\left(h_2\frac{\partial\tau_{11}}{\partial\phi}+\frac{\partial h_1}{\partial z}\left(\tau_{12}+\tau_{21}\right)+h_1\frac{\partial\tau_{21}}{\partial z}\right) \tag{4.3}$$

$$\left[\sigma_{32}\right]=-\frac{1}{h_1h_2}\left(h_2\frac{\partial\tau_{12}}{\partial\phi}+\frac{\partial h_1}{\partial z}\left(-\tau_{11}+\tau_{22}\right)+h_2\frac{\partial\tau_{22}}{\partial z}\right) \tag{4.4}$$

$$\left[\sigma_{32}\right]=-\left(\frac{\tau_{11}}{R_1}+\frac{\tau_{22}}{R_2}\right) \tag{4.5}$$

where $h_1=r$, $h_2=\sec\alpha$, $\alpha=\tan^{-1}\left(\frac{\mathrm{d}r}{\mathrm{d}z}\right)$, and $R_1=-b\left(1+\frac{z^2}{a^2}\left(\frac{b^2}{a^2}-1\right)\right)^{1/2}$, $R_2=-\frac{a^2}{b}\left(1+\frac{z^2}{a^2}\left(\frac{b^2}{a^2}-1\right)\right)^{3/2}$.

The interface energy is associated with the interfacial atomic environment. When the effect of interface energy is simulated by the interface stress, it is essential to determine the relation between the interface stress and the strain at the interface, which illustrates the change of the interfacial local atomic environment. Under the assumption of small deformation, a linearized constitutive relation has been widely employed in the literature (Duan et al., 2005a; Gurtin and Murdoch, 1975; Bottomley and Ogino, 2001). When the interface of a particle in the composite material is considered, the linearized constitutive equation can be written as:

$$\boldsymbol{\tau}=\mathbf{C}^{\mathrm{S}}:\boldsymbol{\varepsilon}^{\mathrm{S}} \tag{4.6}$$

where $\mathbf{C}^{\mathrm{S}}$ is the interface elastic stiffness tensor and $\boldsymbol{\varepsilon}^{\mathrm{S}}$ is the interface strain. As the thickness of the idealized interphase is neglected, the interface strain becomes identical to the tangential

components of the strain at the interface in the bulk material. As indicated by Duan et al. (2005a) that an isotropic interface is able to describe the interfacial elastic behavior under small deformations, a linear isotropic constitutive relation is adopted here. The linear isotropic interface stiffness tensor follows the form

$$\mathbf{C}^{\mathrm{S}} = 2K^{\mathrm{S}}\mathbf{L}^{\mathrm{v}}_{ijkl} + 2\mu^{\mathrm{S}}\mathbf{L}^{\mathrm{d}}_{ijkl} \tag{4.7}$$

for *i, j, k, l* = 1, 2, with

$$\mathbf{L}^{\mathrm{v}}_{ijkl} = \frac{1}{2}\delta_{ij}\delta_{kl}\mathbf{e}_i \otimes \mathbf{e}_j \otimes \mathbf{e}_k \otimes \mathbf{e}_l \tag{4.8}$$

$$\mathbf{L}^{\mathrm{d}}_{ijkl} = \frac{1}{2}\left(\delta_{ik}\delta_{jl} + \delta_{jk}\delta_{il} - \delta_{ij}\delta_{kl}\right)\mathbf{e}_i \otimes \mathbf{e}_j \otimes \mathbf{e}_k \otimes \mathbf{e}_l \tag{4.9}$$

where K^{S}, μ^{S} are the 'bulk modulus' and the 'shear modulus' of the idealized two-dimensional interface.

4.3 Interface Discontinuities

For a single ellipsoidal particle reinforced composite subjected to the far-field stress, the stress disturbance from the inhomogeneity is equivalent to the stress disturbance induced by a uniform stress-free strain (eigenstrain) in an inclusion (Eshelby, 1957, 1961; Mura, 2013). On the other hand, for the multi-particle reinforced composite, the particle-particle and the particle-matrix interactions are much more complicated compared with the single particle composite, which lead to nonuniform elastic fields surrounding each particle and nonuniform eigenstrain in the equivalent inclusions. To simplify the interaction problem, an effective medium approach is suggested by Mori and Tanaka (1973) (cf. Ju and Chen, 1994a, b) to treat each particle as a single particle inside

an effective matrix, which expands the use of Eshelby's formulation to the multiparticle case and enables the prediction of effective properties. The Mori-Tanaka method is essentially a special case of the particle-interaction framework proposed by Ju and Chen (1994a, b), if the first-order non-interacting method is adopted. However, the perfect interface conditions (the continuous stress and strain through the interface) are assumed in the Eshelby's framework. When discontinuities are introduced at the interface, we use the *generalized* Young-Laplace equations to determine the stress and the strain fields in the reinforcement particles instead of the Eshelby's solutions.

Now we consider a multiphase prolate-spheroidal-particle-reinforced nanocomposite with isotropic reinforcements and the matrix material. Let us assume that all particles are unidirectionally aligned, and the particles in each reinforcement phase are identically shaped and randomly distributed in the matrix. When the particles are not unidirectionally aligned, the present work can be easily generalized with specified orientation distribution. For the *r*th phase particle Ω_r, let us follow Mori and Tanaka's assumption by regarding each particle as a single particle embedded in an otherwise homogeneous effective matrix with the averaged strain $\overline{\boldsymbol{\varepsilon}}_0$. Further, the averaged strain is also considered in the particle for simplicity. Following the equivalent inclusion principle, the equivalent inclusion equation for Ω_r can be rendered as:

$$\mathbf{C}_0 : \left(\boldsymbol{\varepsilon}_r - \boldsymbol{\varepsilon}_r^*\right) = \mathbf{C}_r : \boldsymbol{\varepsilon}_r \tag{4.10}$$

where $\mathbf{C}_0$ and $\mathbf{C}_r$ are, respectively, the stiffness tensor of the matrix and the particle, $\boldsymbol{\varepsilon}_r$ is the averaged total strain in the particle, and $\boldsymbol{\varepsilon}_r^*$ is the eigenstrain. From Eq. (4.10), we have

$$\boldsymbol{\varepsilon}_r^* = \mathbf{D}_r^{-1} : \boldsymbol{\varepsilon}_r \tag{4.11}$$

where

$$\mathbf{D}_r = \left(\mathbf{C}_r - \mathbf{C}_0\right)^{-1} : \mathbf{C}_0 \tag{4.12}$$

Furthermore, the elastic strain $\mathbf{e}_r$ in the particle becomes

$$\mathbf{e}_r = \boldsymbol{\varepsilon}_r - \boldsymbol{\varepsilon}_r^* = \left(\mathbf{I} - \mathbf{D}_r^{-1}\right) : \boldsymbol{\varepsilon}_r \tag{4.13}$$

It is emphasized that the eigenstrain is *nonzero* in the particle domain and *zero* in the matrix domain, and can be determined from Eq. (4.11) once the total strain of the particle is obtained.

Based on the assumption that no interfacial debonding happens at the matrix-reinforcement interface, the displacement continuity condition at the interface can be expressed as

$$\left[\mathbf{u}_r\right] = \mathbf{0} \tag{4.14}$$

where $\left[\mathbf{u}_r\right]$ is the relative displacement at the interface between the surrounding matrix and Ω_r. From this point, **[.]** denotes the interfacial discontinuity of inner value from the matrix to the particle. It follows from Eq. (4.14) that the displacement gradient at the interface can be discontinuous over the interface (Mura, 2013; Qu and Cherkaoui, 2006); that is, we have

$$\left[\mathbf{u}_r \nabla\right] = \boldsymbol{\lambda}_r \otimes \mathbf{n} \tag{4.15}$$

where $\boldsymbol{\lambda}_r$ is the vector that magnifies the discontinuity of the displacement gradient over the interface and **n** is the unit normal vector to the interface. It is noted that the discontinuity is along the normal direction to the interface, and the displacement gradient is continuous in the tangential direction. By substituting Eq. (4.15) into the strain compatibility equations, the interfacial strain discontinuity is rendered as:

$$\boldsymbol{\varepsilon}_r^{\lambda} = \left[\boldsymbol{\varepsilon}_r\right] = \frac{1}{2}\left(\left[\mathbf{u}_r\nabla\right] + \left[\nabla\mathbf{u}_r\right]\right) = \frac{1}{2}\left(\boldsymbol{\lambda}^r \otimes \mathbf{n} + \mathbf{n} \otimes \boldsymbol{\lambda}^r\right) \tag{4.16}$$

where $\boldsymbol{\varepsilon}_r^{\lambda}$ is defined as the strain discontinuity through the interface. In accordance with Eqs. (4.13) and (4.16), the interface discontinuity of elastic strain becomes

$$\left[\mathbf{e}_r\right] = \left[\boldsymbol{\varepsilon}_r\right] - \left[\boldsymbol{\varepsilon}_r^*\right] = \boldsymbol{\varepsilon}_r^{\lambda} + \boldsymbol{\varepsilon}_r^* \tag{4.17}$$

Further, the interfacial stress discontinuity takes the form

$$\left[\boldsymbol{\sigma}_r\right] = \mathbf{C}_0 : \left[\mathbf{e}_r\right] = \mathbf{C}_0 : \left(\boldsymbol{\lambda}^r \otimes \mathbf{n} + \boldsymbol{\varepsilon}_r^*\right) \tag{4.18}$$

Substitution of Eqs. (4.6) and (4.18) into Eq. (4.1) leads to

$$\mathbf{C}_0 : \left(\boldsymbol{\lambda}^r \otimes \mathbf{n} + \boldsymbol{\varepsilon}_r^*\right) \cdot \mathbf{n} = -\nabla_S \cdot \left(\mathbf{C}_r^S : \boldsymbol{\varepsilon}_r^S\right) \tag{4.19}$$

From Eq. (4.19), the vector of discontinuity $\boldsymbol{\lambda}_r$ can be determined by the eigenstrain $\boldsymbol{\varepsilon}_r^*$ in the particle and the total strain $\overline{\boldsymbol{\varepsilon}}_0$ in the matrix, whose tangential components are identical to the interface strain $\boldsymbol{\varepsilon}_r^S$. Moreover, the strain discontinuity $\boldsymbol{\varepsilon}_r^{\lambda}$ can be solved according to Eq. (4.16). To determine the averaged strain in the particle, an interface averaging procedure is applied to the strain discontinuity $\boldsymbol{\varepsilon}_r^{\lambda}$:

$$\overline{\boldsymbol{\varepsilon}}_r^{\lambda} = \frac{1}{\partial\Omega_r}\int_{\partial\Omega_r} \boldsymbol{\varepsilon}_r^{\lambda}\, dA = \mathbf{A}_r : \overline{\boldsymbol{\varepsilon}}_0 + \mathbf{B} : \boldsymbol{\varepsilon}_r^* \tag{4.20}$$

where $\overline{\boldsymbol{\varepsilon}}_r^{\lambda}$ is the averaged interfacial strain discontinuity tensor, $\partial\Omega_r$ is the interface area of the particle Ω_r, and $\mathbf{A}_r$ and $\mathbf{B}$ are the coefficient tensors, whose detailed expressions are exhibited in **Appendix I** and **II** for prolate spheroids. For illustration, the detailed expressions of $\mathbf{A}_r$ and $\mathbf{B}$ under two limiting conditions are rendered here. When the spheroid reduces to a sphere with the radius *a*, the coefficient tensors $\mathbf{A}_r$ and $\mathbf{B}$ become isotropic tensors taking the

forms:

$$\left(A_r\right)_{ijkl}=\frac{1}{a}\left(\frac{8}{15}\frac{K_r^S}{M_0}-\frac{2}{15}\frac{K_r^S}{\mu_0}-\frac{4}{15}\frac{\mu_r^S}{\mu_0}\right)\delta_{ij}\delta_{kl}+\frac{1}{a}\left(-\frac{4}{15}\frac{K_r^S}{M_0}+\frac{2}{5}\frac{K_r^S}{\mu_0}+\frac{4}{5}\frac{\mu_r^S}{\mu_0}\right)\left(\delta_{ik}\delta_{jl}+\delta_{il}\delta_{jk}\right) \quad (4.21)$$

$$B_{ijkl}=\left(-\frac{1}{3}\frac{K_0}{M_0}+\frac{4}{45}\frac{\mu_0}{M_0}+\frac{2}{15}\right)\delta_{ij}\delta_{kl}+\left(-\frac{4}{15}\frac{\mu_0}{M_0}-\frac{2}{5}\right)\left(\delta_{ik}\delta_{jl}+\delta_{il}\delta_{jk}\right) \quad (4.22)$$

for $i, j, k, l = 1, 2, 3$, where M_0 is the P-wave modulus defined as $M_0=K_0+\frac{4}{3}\mu_0$. When the semi-axis a, in Eq. (4.2), goes to infinity, the spheroidal particle becomes a cylindrical fiber with $\mathbf{A}_r$ and $\mathbf{B}$ equal to

$$\left(A_r\right)_{ijkl}=\frac{1}{b}\left(\frac{3}{8}\frac{K_S+\mu_S}{M_0}-\frac{1}{4}\frac{K_S+\mu_S}{\mu_0}\right)\delta_{ij}\delta_{kl}+\frac{1}{b}\left(-\frac{1}{4}\frac{K_S+\mu_S}{M_0}+\frac{1}{2}\frac{K_S+\mu_S}{\mu_0}\right)\left(\delta_{ik}\delta_{jl}+\delta_{il}\delta_{jk}\right) \quad (4.23)$$

$$B_{ijkl}=\left(\frac{1}{4}-\frac{1}{2}\frac{K_0}{M_0}+\frac{1}{12}\frac{\mu_0}{M_0}\right)\delta_{ij}\delta_{kl}+\left(-\frac{1}{2}-\frac{1}{2}\frac{\mu_0}{M_0}\right)\left(\delta_{ik}\delta_{jl}+\delta_{il}\delta_{jk}\right) \quad (4.24)$$

for $i, j, k, l = 1, 2$, and

$$\left(A_r\right)_{1133}=\left(A_r\right)_{2233}=\frac{1}{2}\frac{K_S-\mu_S}{bM_0},\quad \left(A_r\right)_{3311}=\left(A_r\right)_{3322}=0,\quad \left(A_r\right)_{1313}=\left(A_r\right)_{2323}=\frac{1}{2}\frac{\mu_S}{b\mu_0}$$

$$B_{1133}=B_{2233}=-\frac{1}{2}\frac{K_0}{M_0}+\frac{1}{3}\frac{\mu_0}{M_0},\quad B_{3311}=B_{3322}=0,\quad B_{1313}=B_{2323}=-\frac{1}{2}$$

It is noted that under either limiting conditions; i.e., the spheroidal particle becomes a sphere or a cylinder, the coefficient tensor $\mathbf{B}$ is identical to the negative of the Eshelby tensor for spherical or cylindrical particles (see Mura, 2013 for detailed expressions of the Eshelby tensor). For spheroids, the components $-B_{1111}$ and $-B_{3333}$ are compared with the corresponding components S_{1111} and S_{3333} of the Eshelby tensor with the change of aspect ratio in Fig. 4-1 and Fig. 4-2.

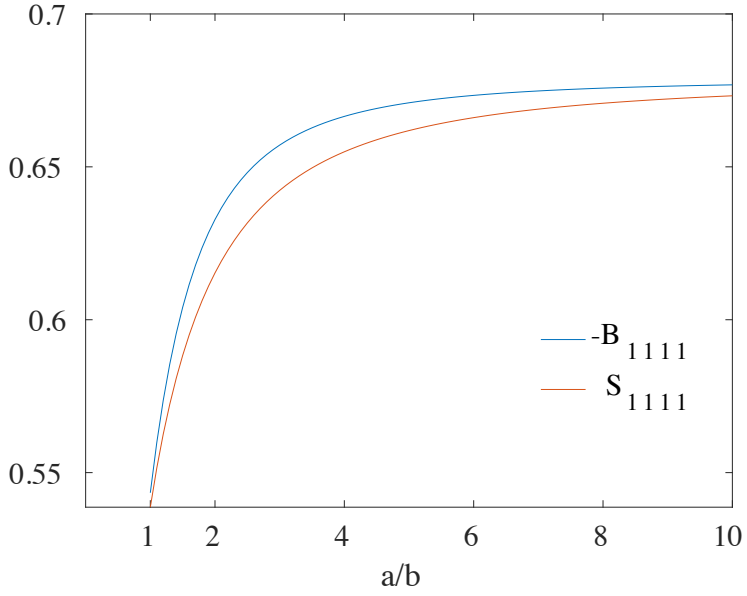

Figure 4–1 Comparison between $-B_{1111}$ and the component S_{1111} of the Eshelby tensor vs. the aspect ratio (The material properties are $K_0 = 75.2\text{GPa}$, $\mu_0 = 34.7\text{GPa}$)

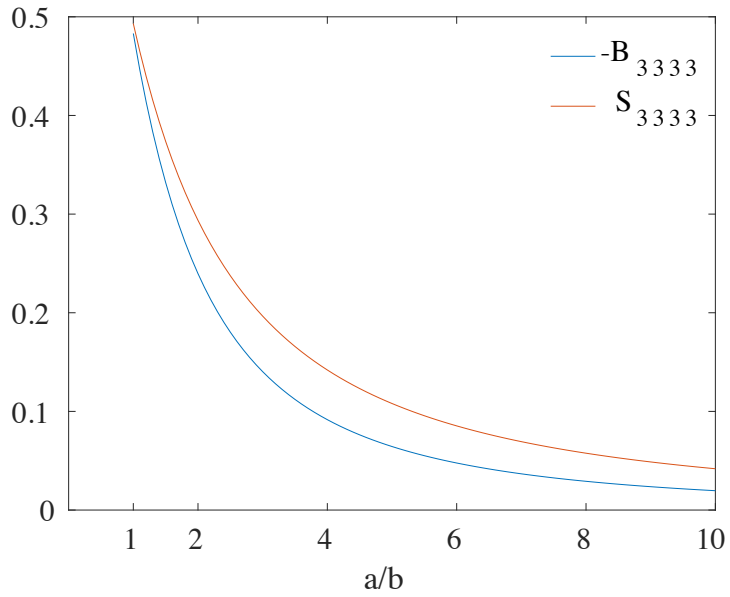

Figure 4–2 Comparison between $-B_{3333}$ and the component S_{3333} of the Eshelby tensor vs. the aspect ratio (The material properties are $K_0 = 75.2\text{GPa}$, $\mu_0 = 34.7\text{GPa}$)

The corresponding components in tensor $-\mathbf{B}$ and the Eshelby tensor reveal to be very close between the limiting conditions. The components of tensor $\mathbf{A}_r$, A_{1111} and A_{3333}, are plotted in Fig. 4-3 and 4-4 with respect to the size of the reinforcement. The components approach zero with the increasing of the size of reinforcement.

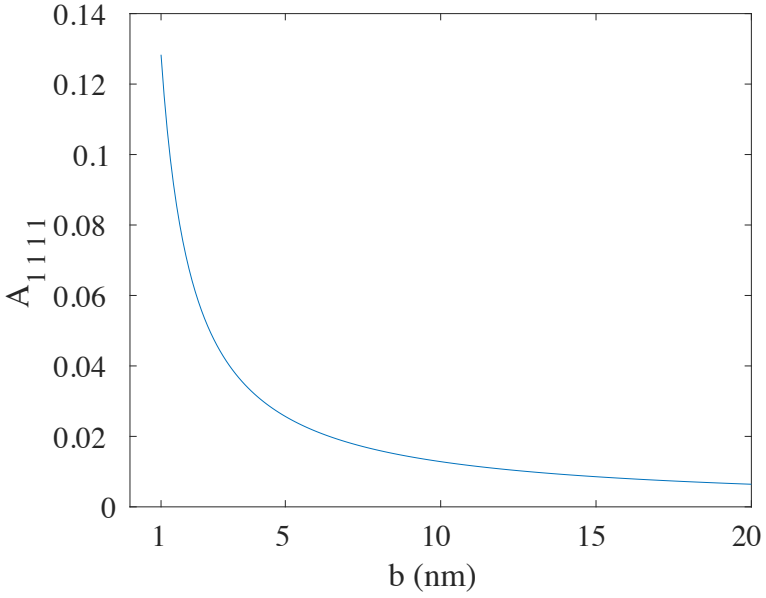

Figure 4–3 The component A_{1111} of the coefficient tensor A vs. the particle size b (with the aspect ratio a/b=5, the volume fraction $\phi_1 = 0.2$, $K_S = 12.932\text{N/m}$, $\mu_S = -0.3755\text{N/m}$, $K_0 = 75.2\text{GPa}$, $\mu_0 = 34.7\text{GPa}$)

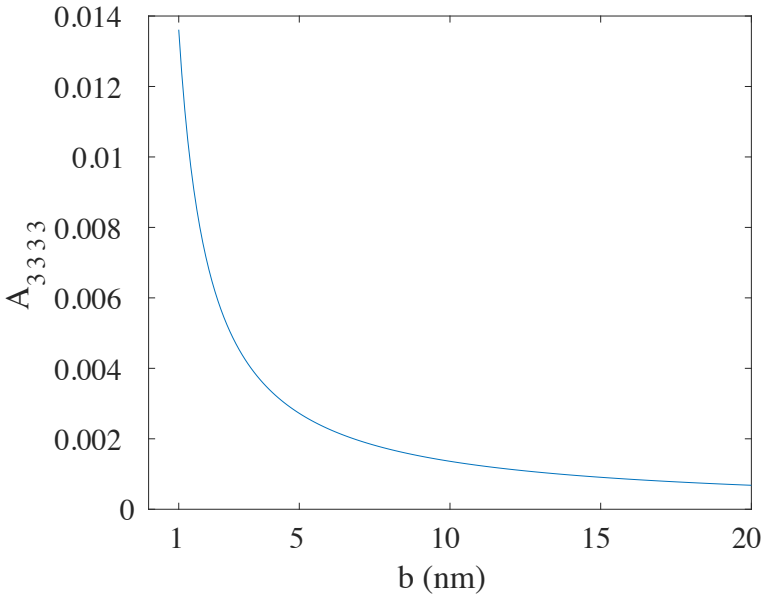

Figure 4–4 The component A_{3333} of the coefficient tensor A vs. the particle size *b* (with the aspect ratio *a*/*b*=5, the volume fraction $\phi_1 = 0.2$, $K_S = 12.932\text{N/m}$, $\mu_S = -0.3755\text{N/m}$, $K_0 = 75.2\text{GPa}$, $\mu_0 = 34.7\text{GPa}$)

Further, according to Eq. (4.16), the effective strain in Ω_r can be revealed as:

$$\boldsymbol{\varepsilon}_r = \overline{\boldsymbol{\varepsilon}}_0 - \overline{\boldsymbol{\varepsilon}}_r^{\lambda} = \left(\mathbf{I} - \mathbf{A}_r\right) : \overline{\boldsymbol{\varepsilon}}_0 - \mathbf{B} : \boldsymbol{\varepsilon}_r^* \tag{4.25}$$

In this section, an interfacial averaged strain discontinuity tensor is derived in order to determine the effective strain in the particle. The corresponding coefficient tensors, $\mathbf{A}_r$ and $\mathbf{B}$, are presented in detail in **Appendix II** and **III** for spheroids, in Eqs. (21)–(22) for spheres, and in Eqs. (23)–(24) for cylinders. The components of tensor $\mathbf{A}_r$ exhibit the dependence on the interface elastic stiffness and the dimensions of the particle Ω_r. They decrease as the size of the reinforcement particles increases, leading to the decrease of the interface energy effect.

Additionally, when the interface energy effect is neglected, all the components of $\mathbf{A}_r$ become zero. On the other hand, tensor $\mathbf{B}$ is a constant tensor based on the matrix properties only, which equals to the negative of the Eshelby tensor at limiting conditions. Moreover, the difference between the tensor $-\mathbf{B}$ and Eshelby tensor for prolate spheroids appears to be negligible.

4.4 Effective Moduli of Spheroidal Particle Reinforced Composites

The strain discontinuity at the interface is established for the composite with a single spheroidal particle inside the otherwise homogeneous effective matrix, and, from which, the strain of the particle is related to the strain in the matrix. In this section, predictions on the effective elastic stiffness of the multi-particle reinforced nanocomposites is presented. Now, let us define the effective elastic stiffness tensor as

$$\overline{\boldsymbol{\sigma}} = \mathbf{C}_* : \overline{\boldsymbol{\varepsilon}} \tag{4.26}$$

where $\overline{\boldsymbol{\sigma}}$ and $\overline{\boldsymbol{\varepsilon}}$ are, respectively, the averaged stress and averaged strain tensors of the composite, defined as

$$\overline{\boldsymbol{\sigma}} = \frac{1}{V}\int_V \boldsymbol{\sigma}(\mathbf{x})\mathrm{d}\mathbf{x} = \frac{1}{V}\left[\int_{V_m} \boldsymbol{\sigma}(\mathbf{x})\mathrm{d}\mathbf{x} + \sum_{r=1}^{n}\int_{V_r} \boldsymbol{\sigma}(\mathbf{x})\mathrm{d}\mathbf{x}\right] \tag{4.27}$$

$$\overline{\boldsymbol{\varepsilon}} = \frac{1}{V}\int_V \boldsymbol{\varepsilon}(\mathbf{x})\mathrm{d}\mathbf{x} = \frac{1}{V}\left[\int_{V_m} \boldsymbol{\varepsilon}(\mathbf{x})\mathrm{d}\mathbf{x} + \sum_{r=1}^{n}\int_{V_r} \boldsymbol{\varepsilon}(\mathbf{x})\mathrm{d}\mathbf{x}\right] \tag{4.28}$$

Here, V_m is the volume of matrix, V_r is the total volume of the rth phase particles and n is the total number of particulate phases. Substitution of Eq. (4.25) into Eq. (4.10) yields

$$\mathbf{C}_r : \left[\left(\mathbf{I}-\mathbf{A}_r\right) : \overline{\boldsymbol{\varepsilon}}_0 - \mathbf{B} : \boldsymbol{\varepsilon}_r^*\right] = \mathbf{C}_0 : \left[\left(\mathbf{I}-\mathbf{A}_r\right) : \overline{\boldsymbol{\varepsilon}}_0 - \left(\mathbf{I}+\mathbf{B}\right) : \boldsymbol{\varepsilon}_r^*\right] \tag{4.29}$$

Then, eigenstrain $\boldsymbol{\varepsilon}_r^*$ can be derived from Eq. (4.29):

$$\boldsymbol{\varepsilon}_r^* = \left[\left(\mathbf{I}+\mathbf{B}_r\right)-\mathbf{C}_0^{-1}:\mathbf{C}_r:\mathbf{B}\right]^{-1}:\left[\left(\mathbf{I}-\mathbf{C}_0^{-1}:\mathbf{C}_r\right):\left(\mathbf{I}-\mathbf{A}_r\right)\right]:\bar{\boldsymbol{\varepsilon}}_0 \tag{4.30}$$

By substituting Eq. (4.30) into Eq. (4.28), the averaged strain $\boldsymbol{\varepsilon}_r$ of the *r*th phase particle becomes

$$\boldsymbol{\varepsilon}_r = \mathbf{G}_r:\bar{\boldsymbol{\varepsilon}}_0 \tag{4.31}$$

where $\mathbf{G}_r$ is the local strain concentration tensor defined as:

$$\mathbf{G}_r = \mathbf{I}-\mathbf{A}_r-\mathbf{B}:\left[\left(\mathbf{I}+\mathbf{B}\right)-\mathbf{C}_0^{-1}:\mathbf{C}_r:\mathbf{B}\right]^{-1}:\left[\left(\mathbf{I}-\mathbf{C}_0^{-1}:\mathbf{C}_r\right):\left(\mathbf{I}-\mathbf{A}_r\right)\right] \tag{4.32}$$

In addition, from Eq. (4.28) and (4.31), we arrive at

$$\bar{\boldsymbol{\varepsilon}}_r = \mathbf{N}_r:\bar{\boldsymbol{\varepsilon}} \tag{4.33}$$

where $\mathbf{N}_r$ is the global strain concentration tensor and takes the form

$$\mathbf{N}_r = \mathbf{G}_r:\left[\phi_m\mathbf{I}+\sum_{r=1}^{N}\phi_r\mathbf{G}_r\right]^{-1} \tag{4.34}$$

Here, ϕ_m is the volume fraction of the matrix and ϕ_r is the volume fraction of the *r*th phase particles. Subsequently, the effective stiffness tensor becomes

$$\bar{\mathbf{C}} = \mathbf{C}_0+\sum_{r=1}^{n}\phi_r\left(\mathbf{C}_r-\mathbf{C}_0\right):\mathbf{N}_r \tag{4.35}$$

Based on the interfacial strain discontinuity tensor in the previous section, the effective elastic stiffness is derived following the classical homogenization procedures in the micromechanical framework. Note that the present work considers the particle interactions indirectly. Thus, inaccuracies are induced in the effective stiffness, particularly for composite materials with high particle concentrations. The direct inter-particle interactions were considered by Ju and Chen (1994a, b), and they showed higher order estimation of the effective properties, which provide

higher accuracy for the composite with high particle concentrations. To provide more accurate solutions at higher particle concentration, future work can be carried out by considering the inter-particle interactions in the present framework.

4.5 Nanomechanics Examples and Discussions

In previous sections, a nanomechanics framework is formulated to predict the effective elastic moduli of spheroidal particle reinforced multi-phase nanocomposites. The formulation is based on the assumption made by Mori and Tanaka on the elastic fields in the matrix surrounding each reinforcement particle (Mori and Tanaka, 1973; Weng, 1984, 1990). Different from the classical micromechanical frameworks, the effect of the interface energy on the effective stiffness tensor is considered, and the *generalized* Young-Laplace equations are solved at the interface to determine the strain field inside the particles. In what follows, nanomechanical homogenization examples are presented to compare our solutions in this chapter with the classical micromechanical solutions.

4.5.1 Analytical solutions of effective moduli for the 2-phase spherical-particle-reinforced nanocomposite

Let us consider the simplest case of a two-phase spherical-particle-reinforced nanocomposite. Assume that the matrix and the particles are linear isotropic materials with the elastic stiffness tensors $\mathbf{C}_0$ and $\mathbf{C}_1$, respectively. According to Eq. (4.35), the effective stiffness tensor can be exhibited as:

$$\bar{\mathbf{C}} = \mathbf{C}_0 + \phi_1 (\mathbf{C}_1 - \mathbf{C}_0) : \mathbf{N}_1 \tag{4.36}$$

and the corresponding effective bulk modulus and shear modulus are

$$\bar{K} = K_0 + \frac{\phi_1 (K_1 - K_0)(3M_0 - 4K_S/a)}{3M_0 + 3(1-\phi_1)(K_1 - K_0) - 4\phi_1 K_S/a} \tag{4.37}$$

$$\bar{\mu} = \mu_0 + \frac{15\phi_1\mu_0 M_0(\mu_1 - \mu_0) - \phi_1(\mu_1 - \mu_0)\left[2(3K_0 + 2\mu_0)K_S/a + 12M_0\mu_S/a\right]}{15\mu_0 M_0 + 6(1-\phi_1)(\mu_1 - \mu_0)(K_0 + 2\mu_0) - \phi_1\left[2(3K_0 + 2\mu_0)K_S/a + 12M_0\mu_S/a\right]} \tag{4.38}$$

Compared with the micromechanical Mori-Tanaka solution, the effective moduli are displayed to have additional size-dependent terms due to the interface energy effect. As the particle size increases, the size-dependent terms decrease. If the interface energy effect is neglected ($K_s = \mu_s = 0$), then size-dependent terms vanish and Eqs. (4.37)–(4.38) reduce to the classical micromechanics solutions (Qu, J., and Cherkaoui, 2006; Mura, 2013).

4.5.2 Numerical solutions of effective elastic stiffness for the 2-phase spheroidal-particle-reinforced nanocomposite

Next, numerical calculations on effective elastic stiffness will be presented for the two-phase spheroidal-particle-reinforced nanocomposite. Consider an aluminum matrix (K_0 = 75.2 GPa, μ_0 = 34.7 GPa) nanocomposite with randomly distributed spheroidal nanovoids. Miller and Shenoy obtained the free-surface properties of this type of composite through molecular dynamics simulations in 2000 [19]. For the surface [1 1 1], they obtained K_S = 12.932 N/m and μ_S = –0.3755 N/m; for the surface [1 0 0], K_S = –5.457 N/m and μ_S = –6.2178 N/m (Duan et al., 2005a; Miller and Shenoy, 2000; Sharma and Dasgupta, 2002). These sets of interface properties are adopted in

this section for illustration.

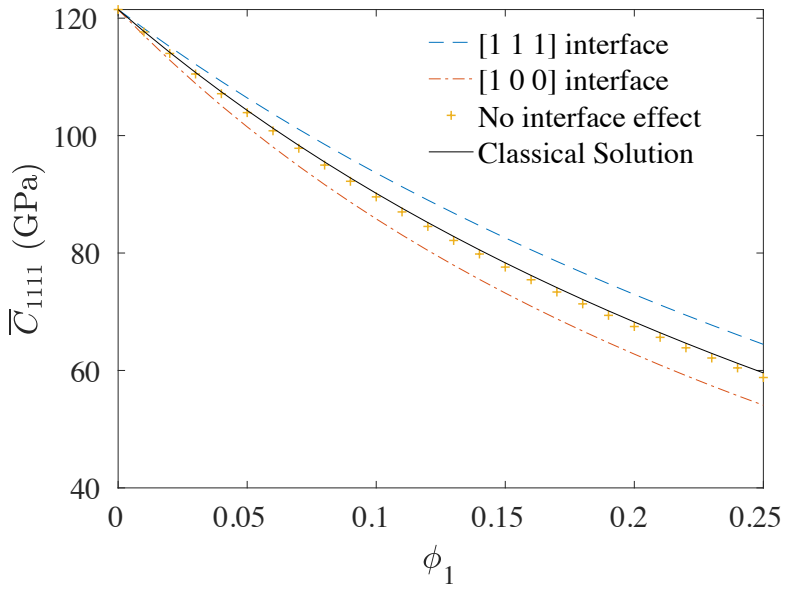

Figure 4–5 The effective elastic stiffness $\overline{C}_{1111}$ vs. the volume fraction ϕ_1 (the aspect ratio a/b=5).

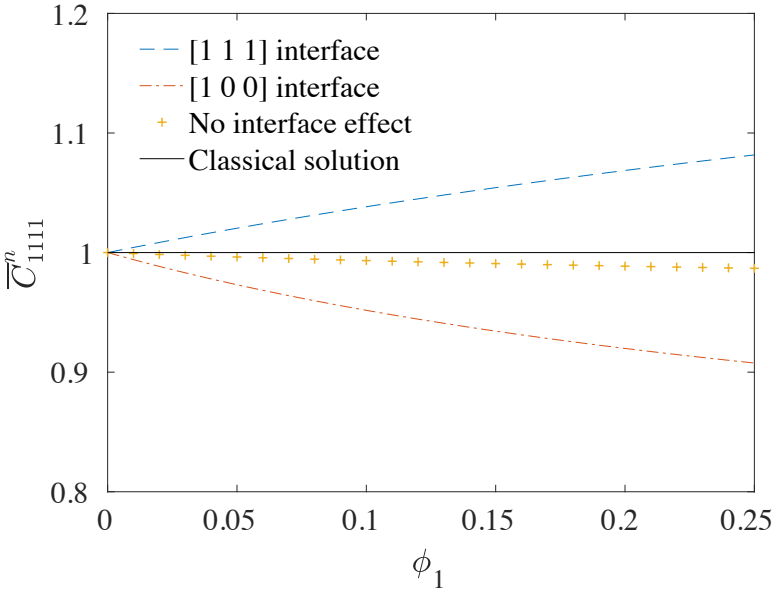

Figure 4–6 The normalized effective elastic stiffness $\overline{C}_{1111}$ (w.r.t. the classical micromechanics solution) vs. the volume fraction ϕ_1 (with the aspect ratio a/b=5).

The change of the component $\overline{C}_{1111}$ of the effective stiffness tensor with respect to the volume fraction ϕ of the spheroidal voids is rendered in Fig. 4-5 and Fig. 4-6. The solutions corresponding to different interface properties are compared with the classical micromechanics solutions. It is observed that as the volume fraction increases, the deviation increases between the solutions with and without the interface effect. Since the total interface area in a composite is proportionally related to the volume fraction of the inhomogeneities, it is reasonable to have larger interface energy effect on the effective elastic stiffness of composites with higher volume fractions.

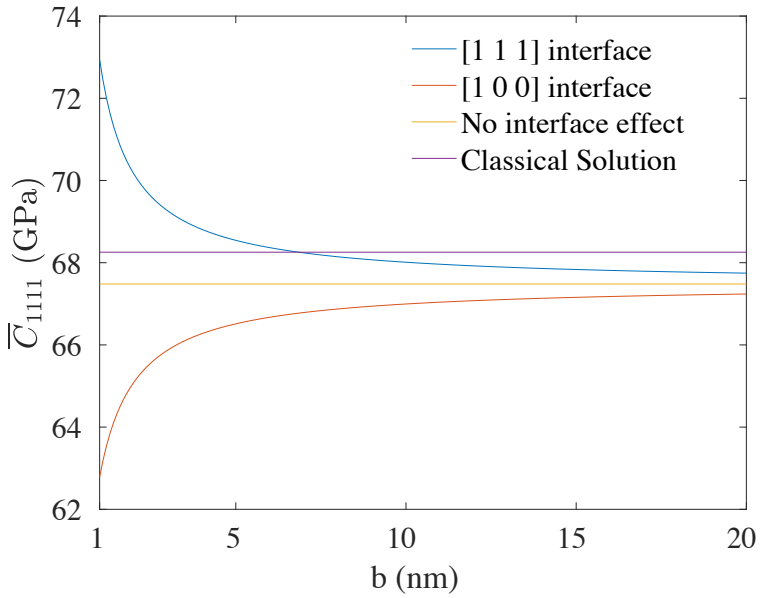

Figure 4–7 The effective elastic stiffness $\overline{C}_{1111}$ vs. the semi-axis b (with the aspect ratio a/b=5, and the volume fraction $\phi_1 = 0.2$).

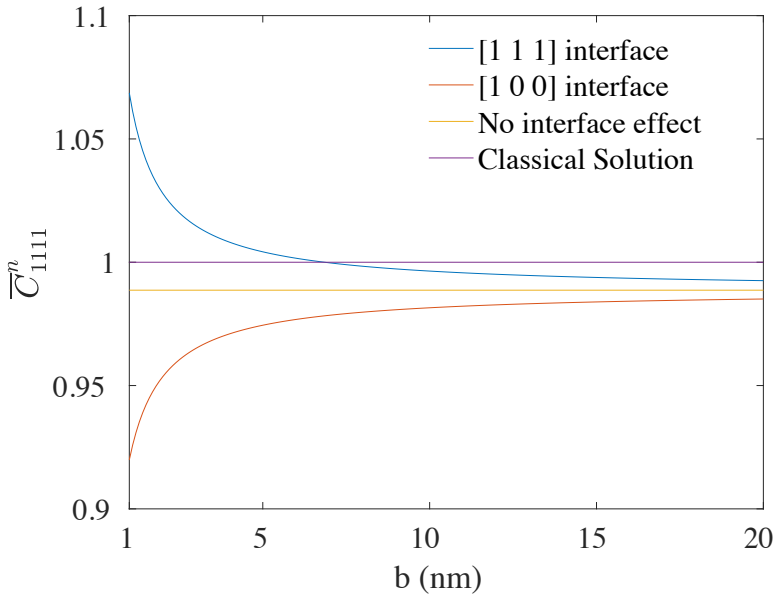

Figure 4–8 The normalized effective elastic stiffness $\overline{C}_{1111}$ (w.r.t. the classical micromechanics solution) vs. the semi-axis *b* (with the aspect ratio *a/b*=5, and the volume fraction $\phi_1 = 0.2$).

As the gross interface area is inversely related to the size of the spheroidal particle, the size effect on the effective elastic stiffness is studied. Fig. 4-7 and Fig. 4-8 reveal that the interface energy effect decreases as the particle size increases, and the interface energy has noticeable effect on the effective elastic stiffness for b<10nm (a/b=5) when the current interface properties are considered. Micromechanical solution of effective stiffness under our framework (by neglecting the interface energy effect) is also compared with the solution of the classical micromechanics solution. A 1% deviation is observed compared with micromechanical Mori-Tanaka solution. This is due to the small difference between the coefficient tensor $-\mathbf{B}$ in our formulation and the Eshelby tensor in classical micromechanics formulations for spheroids.

4.6 Conclusions

The interface energy effect on the elastic behavior of nanocomposite is discussed. The interface energy effect is regarded as the change of the interface boundary conditions, which is induced by the two-dimensional interface stress at the idealized zero-thickness membrane interface between the inhomogeneity and the matrix. The discontinuous boundary conditions at the interface are presented for spheroidal inhomogeneities.

Furthermore, a nanomechanical framework is formulated to predict the effective moduli of composite material reinforced by nano-sized spheroidal particles. By solving the interfacial discontinuity equations and applying the micromechanical homogenization procedures, we relate the effective elastic fields in the inhomogeneities to the effective elastic fields in the matrix. Accordingly, the effective elastic moduli of the nanocomposite are derived.

For illustration purpose, effective moduli for a composite material with spheroidal voids are presented. It is noted that the effective moduli depend upon the dimensions and volume fractions of the spherical inhomogeneities and approach to the classical micromechanical results with increasing radius and decreasing volume fractions of the inhomogeneities.

4.7 References

Bottomley, D. J., and Ogino, T.: Alternative to the Shuttleworth formulation of solid surface stress. Phys. Rev. B. 63, 165412 (2001)

Cammarata, R. C.: Surface and interface stress effects on interfacial and nanostructured materials. Mater. Sci. Eng. A 237, 180-184 (1997)

Chen, T., Chiu, M. S., and Weng, C. N.: Derivation of the generalized Young-Laplace equation of curved interfaces in nanoscaled solids. J. Appl. Phys. 100, 074308 (2006)

Dingreville, R., Qu, J., and Cherkaoui, M.: Surface free energy and its effect on the elastic behavior of nano-sized particles, wires and films. J. Mech. Phys. Solids. 53, 1827-1854 (2005)

Duan, H. L., Wang, J. X., Huang, Z. P., and Karihaloo, B. L.: Size-dependent effective elastic constants of solids containing nano-inhomogeneities with interface stress. J. Mech. Phys. Solids. 53, 1574-1596 (2005a)

Duan, H. L., Wang, J., Huang, Z. P., and Luo, Z. Y.: Stress concentration tensors of inhomogeneities with interface effects. Mech. Mater. 37(7), 723-736 (2005b)

Eshelby, J. D.: The determination of the elastic field of an ellipsoidal inclusion, and related problems. Proc. R. Soc. Lond. A, 241, 376-396 (1957)

Eshelby, J. D.: Elastic inclusion and inhomogeneities. Prog. Solid Mech. 2, 89-140 (1961)

Fan, M., Zhang, Y. M., & Xiao, Z. M.: The interface effect of a nano-inhomogeneity on the fracture behavior of a crack and the nearby edge dislocation. Int. J. Damage Mech. 26(3), 480-497 (2017)

Giannelis, E. P.: Polymer layered silicate nanocomposites. Adv. Mater. 8, 29-35 (1996)

Gibbs, J. W.: The scientific papers of J. Willard Gibbs (Vol. 1). Longmans, Green and Company (1906)

Gurtin, M. E., and Murdoch, A. I.: theory of elastic material surfaces. Arch. Ratio. Mech. Anal. 57, 291-323 (1975).

Heidarhaei, M., Shariati, M., & Eipakchi, H. R.: Effect of interfacial debonding on stress transfer in graphene reinforced polymer nanocomposites. Int. J. Damage Mech. 27(7), 1105-1127 (2018)

Herve, E., and Zaoui, A.: N-layered inclusion-based micromechanical modelling. Int. J. Eng. Sci. 31, 1-10 (1993)

Ju, J. W., and Chen, T. M.: Micromechanics and effective moduli of elastic composites containing randomly dispersed ellipsoidal inhomogeneities. Acta Mech. 103, 103-121 (1994a)

Ju, J. W., and Chen, T. M.: Effective elastic moduli of two-phase composites containing randomly dispersed spherical inhomogeneities. Acta Mech. 103, 123-144 (1994b)

Mikata, Y., and Taya, M.: Stress field in and around a coated short fiber in an infinite matrix subjected to uniaxial and biaxial loadings. J. Appl. Mech. 52, 19-24 (1985)

Miller, R. E., and Shenoy, V. B.: Size-dependent elastic properties of nanosized structural elements. Nanotechnology. 11, 139 (2000)

Mori, T., and Tanaka, K.: Average stress in matrix and average elastic energy of materials with misfitting inclusions. Acta Metall. 21, 571-574 (1973)

Mura, T.: Micromechanics of defects in solids. Springer Science & Business Media (2013)

Qiu, Y. P., and Weng, G. J.: Elastic moduli of thickly coated particle and fiber-reinforced composites. J. Appl. Mech. 58, 388-398 (1991)

Qu, J., and Cherkaoui, M.: Fundamentals of Micromechanics of Solidss. John Wiley & Sons, Inc. (2006)

Ray, S. S., and Okamoto, M.: Polymer/layered silicate nanocomposites: a review from preparation to processing. Prog. Polym. Sci. 28, 1539-1641 (2003)

Rostamiyan, Y., & Ferasat, A.: High-speed impact and mechanical strength of ZrO2/polycarbonate nanocomposite. Int. J. Damage Mech. 26(7), 989-1002 (2017)

Sharma, P., and Dasgupta, A.: Average elastic fields and scale-dependent overall properties of heterogeneous micropolar materials containing spherical and cylindrical inhomogeneities. Phys. Rev. B. 66, 224110 (2002)

Sharma, P., Ganti, S., and Bhate, N.: Effect of surfaces on the size-dependent elastic state of nano-inhomogeneities. Appl. Phys. Lett. 82, 535-537 (2003)

Sharma, P., and Ganti, S.: Size-dependent Eshelby's tensor for embedded nano-inclusions incorporating surface/interface energies. J. Appl. Mech. 71, 663-671 (2004)

Shodja, H. M., & Hashemian, B.: Variational bounds and overall shear modulus of nano-composites with interfacial damage in anti-plane couple stress elasticity. Int. J. Damage Mech. 1056789519856934 (2019)

Shuttleworth, R.: The surface tension of solids. Proc. Phys. Soc. Section A 63, 444 (1950)

Voyiadjis, G. Z., & Kattan, P. I.: Fundamental aspects for characterization in continuum damage mechanics. Int. J. Damage Mech. 28(2), 200-218 (2019)

Walpole, L. J.: A coated inclusion in an elastic medium. In Mathematical Proceedings of the Cambridge Philosophical Society (Vol. 83, No. 3, pp. 495-506). Cambridge University Press. (1978)

Wang, Z. Q., Zhao, Y. P., and Huang, Z. P.: The effects of surface tension on the elastic properties of nano structures. Int. J. Eng. Sci. 48, 140-150 (2010)

Weng, G. J.: Some elastic properties of reinforced solids, with special reference to isotropic ones containing spherical inclusions. Int. J. Eng. Sci. 22, 845-856 (1984)

Weng, G. J.: The theoretical connection between Mori-Tanaka's theory and the Hashin-Shtrikman-Walpole bounds. Int. J. Eng. Sci. 28, 1111-1120 (1990)

Wood, J.: The top ten advances in materials science. Mater. Today. 11, 40-45 (2008)

- Chapter 5 -

INTERFACE ENERGY EFFECT ON EFFECTIVE ELASTOPLASTIC BEHAVIOR OF SPHERICAL PARTICLE REINFORCED METAL MATRIX NANOCOMPOSITES

Abstract

A nanomechanical framework is proposed to predict the effective elastoplastic behavior of the spherical particle reinforced metal matrix nanocomposites (MMNCs). The interface energy effect on the effective secant moduli of MMNCs is discussed. In this chapter, particles are assumed to be randomly distributed elastic spheres, while the matrix behaves elastoplastically. The interface energy, which perturbs the local mechanical properties near the matrix-reinforcement interface, is simulated by inducing the interface stress on the idealized zero-thickness membrane interphase between the matrix and the reinforcement. By employing the micromechanical homogenization approaches, an effective yield criterion is formulated, and the effective secant moduli of the spherical particle reinforced MMNCs are derived explicitly. Comparisons between the predictions under the present framework and under the classical micromechanics theories are presented. The dependence of the effective secant moduli upon the total interface area in the composite is noticed. Specifically, larger interface energy effect on the secant moduli is observed as the particle size decreases, whereas the interface energy effect can be neglected when the particle size enters

micrometer range.

5.1 Introduction

The research on the metal matrix composites (MMCs) has a long history in the literature. Due to the remarkable improvements on various properties, such as high strength and stiffness, long fatigue life, improved thermal stability, low density, over monolithic metals and conventional alloys, the MMCs are widely employed in the fields of aerospace, automotive, etc. Recently, with the advent of material science in nanotechnology, metal matrix nanocomposites (MMNCs) have attracted considerable attention. By reducing the dimensions of reinforcement phase to the nanometer scale, numerous desirable properties can be achieved, such as better damping capacity, wear resistance, higher temperature creep resistance and longer fatigue life (Trojanova et al., 2004; Deng et al., 2007; Shehata et al., 2009; Ferkel and Mordike, 2001). Despite the superior properties, the production of MMNCs remains to be the main obstacle that limits the practical applications. Due to the low wettability of ceramic nanoparticles with the molten metal matrix, conventional casting processes are not capable of dispersing the particles homogeneously over the entire matrix material (Casati and Vedani, 2014). Therefore, the production methods are discussed intensively by researchers, and several alternative preparation methods have been proposed in the literature (Yue et al., 1999; Tu et al., 2002; Li et al., 2004; Lan et al., 2004; Gu et al., 2011). Recently, the most popular and promising potential reinforcement materials include carbides, nitrides, oxides,

intermetallic alloys and allotropes of carbon, and the metal matrix could be Al, Cu, Mg and other alloys, etc.

Regarding the development and the applications of MMNCs, the prediction on their effective elastoplastic properties is of considerable practical importance. Predictions on the elastoplastic properties of the micro-particle reinforced MMCs are intensively discussed by researchers during the past decades in the micromechanics field, the related models include the direct particle interaction model (Ju and Chen, 1994a, b, c; Ju and Tseng, 1996, 1997; Ju and Sun, 2001; Voyiadjis and Ju, 1994), the self-consistent method (Hutchinson,1970, 1976), the Mori-Tanaka method (Tandon and Weng, 1988; Weng, 1990; Lagoudas et al., 1991) and the mathematical upper and lower bounds (Castaneda, 1991, 1992, 1996). However, it is well known that when the size of the reinforcement particles enters the nanometer range, the interface energy effect, which is totally neglected in the classical micromechanics theories, needs to be considered in determining the mechanical properties of the nanocomposite. While various strengthening mechanisms are proposed for nanocomposites (Zhang and Chen, 2006, 2008; Sanaty-Zadeh, 2012; Luo et al., 2012), limited studies have focused on constructing an analytical framework in the prediction of their elastoplastic behavior.

Gibbs (1906) pointed out that, due to the distinct local atomic environments, the free energies possessed by the molecules at the material surface is different from the free energy of the bulk material. As a consequence, he introduced the concept of interface energy as the excess free energy per unit area at the surface/interface. When the interface is deformed, the change in the interface

energy leads to the change of the elastic fields near the interface. To characterize the effect of interface energy, Gurtin and Murdoch (1975), based on the membrane theory of thin shells, established a mechanical framework for material surfaces by idealizing the matrix-reinforcement interface as a zero-thickness membrane with the in-plane interface stress. Consequently, the interfacial continuity conditions, which are also named as the *generalized* Young-Laplace equations, can be derived from the equilibrium conditions of a membrane element. Even though the effect of interface energy exists in all kinds of composites, it is usually neglected for the composite with reinforcement phase in or larger than the micrometer scale, where the specific interface area is relatively low. However, when one or more dimensions of reinforcement phase is (are) in the nanometer scale, the interface energy effect becomes essential in determining the effective mechanical properties (Cammarata, 1997). Therefore, in order to predict the elastoplastic behavior of spherical particle reinforced metal matrix nanocomposites, the interface energy effect needs to be considered.

The present chapter is aimed at developing an approximate and simple analytical framework in predicting the effective elastoplastic properties of spherical nanoparticle reinforced MMNCs. In the nanomechanical framework, the size effect is considered in addition to the classical micromechanical treatments for composites. To incorporate the size effect, the *generalized* Young-Laplace equations are solved at the matrix-particle interface in an effective sense. Accordingly, the effective elastic fields are determined, and the effective elastic properties of MMNCs are obtained. In order to predict the plastic responses, an effective yield function is formulated, from

which the secant moduli can be determined. At last, the elastoplastic response under a uniaxial loading is presented for illustration purpose.

5.2 Interface Continuity Conditions

Now we consider a two-phase spherical nanoparticle reinforced metal matrix nanocomposite. Assume that the particles are in the same size and are randomly distributed in the matrix, and both of the particulate phase and the matrix phase are isotropic materials. According to Gurtin and Murdoch (1975), when the interface energy effect is considered, the continuity conditions at the matrix-particle interface can be described by the *generalized* Young-Laplace equations,

$$[\boldsymbol{\sigma}]\cdot\mathbf{n} = -\nabla_S \cdot \boldsymbol{\tau} \tag{5.1}$$

where $[\boldsymbol{\sigma}]$ is the stress discontinuity from matrix to reinforcement, $\mathbf{n}$ is the unit normal to the interface, $\nabla_S \cdot$ is the interface divergence, and $\boldsymbol{\tau}$ represents the interface stress. In the following expressions, [.] denotes the interfacial discontinuity of the said value. Based on the equilibrium conditions in the membrane theory, the *generalized* Young-Laplace equations for spherical particles with the radius a can be expressed as:

$$\left[\sigma_{rr}\right] = \frac{\tau_{\varphi\varphi} + \tau_{\theta\theta}}{a} \tag{5.2}$$

$$\left[\sigma_{r\theta}\right] = -\left(\frac{1}{a}\frac{\partial \tau_{\theta\theta}}{\partial \theta} + \frac{1}{a\sin\theta}\frac{\partial \tau_{\theta\varphi}}{\partial \varphi} + \frac{\tau_{\theta\theta} - \tau_{\varphi\varphi}}{a}\cot\theta\right) \tag{5.3}$$

$$\left[\sigma_{r\varphi}\right] = -\left(\frac{1}{a}\frac{\partial \tau_{\theta\varphi}}{\partial \theta} + \frac{1}{a\sin\theta}\frac{\partial \tau_{\varphi\varphi}}{\partial \varphi} + \frac{2\tau_{\theta\varphi}}{a}\cot\theta\right) \tag{5.4}$$

Unlike the continuity conditions at the traditional perfectly bonded matrix-reinforcement interface, discontinuities in the stress are induced at the interface, the stress in the matrix and the stress in the particle are related through Eqs. (5.2)–(5.4). Under the assumption of small deformation, a linearized constitutive relation between the interface stress and the tangential components of the total strain at the interface is suggested (Gurtin and Murdoch, 1975; Bottomley and Ogino, 2001),

$$\boldsymbol{\tau} = \mathbf{C}^{\mathrm{I}} : \boldsymbol{\varepsilon}^{\mathrm{I}} \tag{5.5}$$

where $\mathbf{C}^{\mathrm{I}}$ is the interface stiffness tensor and $\boldsymbol{\varepsilon}^{\mathrm{I}}$ is the interface strain tensor, which is defined as the two-dimensional tensor consisting the tangential components of the strain at the interface in the bulk material. Further, a linear isotropic constitutive relation is proposed (Miller and Shenoy, 2000; Duan et al., 2005), in which the interface stiffness tensor can be written as:

$$\mathbf{C}^{\mathrm{I}} = 2K^{\mathrm{I}}\mathbf{L}^{\mathrm{v}}_{ijkl} + 2\mu^{\mathrm{I}}\mathbf{L}^{\mathrm{d}}_{ijkl} \tag{5.6}$$

for *i, j, k, l* = 1, 2, with

$$\mathbf{L}^{\mathrm{v}}_{ijkl} = \frac{1}{2}\delta_{ij}\delta_{kl}\mathbf{e}_i \otimes \mathbf{e}_j \otimes \mathbf{e}_k \otimes \mathbf{e}_l \tag{5.7}$$

$$\mathbf{L}^{\mathrm{d}}_{ijkl} = \frac{1}{2}\left(\delta_{ik}\delta_{jl} + \delta_{jk}\delta_{il} - \delta_{ij}\delta_{kl}\right)\mathbf{e}_i \otimes \mathbf{e}_j \otimes \mathbf{e}_k \otimes \mathbf{e}_l \tag{5.8}$$

where K^{I} and μ^{I} are the interface bulk modulus and the interface shear modulus, respectively.

Solving the *generalized* Young-Laplace equations leads to the direct relation between the stress and the strain fields in the matrix and in the reinforcement on the two sides of the interface, from which, theoretically, the elastic fields can be derived. Nevertheless, it is practically impossible to determine the elastic state locally of all the points in a composite due to its sophisticated microstructure, such as the spatial distributions and micro-geometries. Instead, we

are attempting to establish a nanomechanical framework to predict the overall effective elastoplastic properties of the nanocomposite. For micro-particle reinforced composite, classical micromechanical effective medium theories have presented good compatibility with the experimental data at low or moderate particle concentrations by considering the interactions indirectly through the effective strain and stress fields in the matrix. Whereas, the effect of the interface energy is neglected due to the relatively small specific interface area. However, the specific interface area for MMNCs is much higher than the micro-particle reinforced. To predict the mechanical behavior of MMNCs, we bring the interface energy effect into consideration, and therefore, the *generalized* Young-Laplace equations is incorporated into the classical micromechanical homogenization approaches.

Consider a two-phase metal matrix nanocomposite with elastoplastic matrix phase and elastic reinforcement phase. When large plastic strain occurs in the metallic matrix, even more sophisticated interactions could occur in the composite due to the change of its microstructure. Therefore, for simplicity, we consider small strains in this chapter, and accordingly, static isotropy and homogeneity of microstructure are assumed to hold during the loading process. In order to characterize the overall plastic response of the MMNCs, we construct an effective von Mises yield criterion in the matrix phase as

$$\bar{F}\left(\bar{\sigma}_0^*, \bar{\varepsilon}_0^{p*}\right) = \bar{\sigma}_0^* - K\left(\bar{\varepsilon}_0^{p*}\right) \tag{5.9}$$

where $\bar{\sigma}_0^*$ and $\bar{\varepsilon}_0^{p*}$ are the von Mises effective stress and effective plastic strain in the matrix, respectively, defined as:

$$\bar{\sigma}_0^* = \sqrt{\frac{3}{2}\bar{\boldsymbol{\sigma}}_0 : \mathbf{I}^{dev} : \bar{\boldsymbol{\sigma}}_0} \quad \text{and} \quad \bar{\varepsilon}_0^{p*} = \sqrt{\frac{2}{3}\bar{\boldsymbol{\varepsilon}}_0^p : \bar{\boldsymbol{\varepsilon}}_0^p} \tag{5.10}$$

and $\bar{\boldsymbol{\sigma}}_0$ is the averaged stress in the matrix, $\bar{\boldsymbol{\varepsilon}}_0^p$ is the corresponding averaged plastic strain. Further, $K\left(\bar{\varepsilon}_0^{p*}\right)$ represents the isotropic hardening function for the matrix-only material. Although isotropic hardening law with von Mises yield criterion is assumed here, the present work is capable of accommodating more general hardening law and yield criterion by making simple modifications.

When the composite is subjected to a prescribed traction $\mathbf{t} = \bar{\boldsymbol{\sigma}} \cdot \mathbf{n}$ at the far field, Tandon and Weng (1988) suggested an approximate expression of the secant Young's modulus E_0^s of the matrix phase,

$$E_0^s = \frac{1}{\dfrac{1}{E_0} + \dfrac{\bar{\varepsilon}_0^{p*}}{\bar{\sigma}_0^*}} \tag{5.11}$$

Due to the plastic incompressibility of the metallic matrix, a further restraint is imposed on the secant Poisson's ratio ν_0^s that

$$\nu_0^s = \frac{1}{2} - \left(\frac{1}{2} - \nu_0\right)\frac{E_0^s}{E_0} \tag{5.12}$$

where E_0 and ν_0 are the Young's modulus and Poisson's ratio of the matrix.

Once the secant Young's modulus and the secant Poisson's ratio of the matrix is determined, the corresponding secant bulk modulus K_0^s and shear modulus μ_0^s can be obtained through

$$K_0^s = \frac{E_0^s}{3\left(1-2\nu_0^s\right)} \quad \text{and} \quad \mu_0^s = \frac{E_0^s}{2\left(1+\nu_0^s\right)} \tag{5.13}$$

It is noted in Eqs. (5.12)–(5.13) that the secant bulk modulus K_0^s is identical to the elastic bulk modulus K_0 due to the plastic incompressibility of the matrix.

To predict the overall effective elastoplastic behavior of a composite, it is essential to determine the elastic fields in the reinforcement phase based on the elastic fields in the surrounding matrix. Following Hill's statement (Hill, 1965) about the continuous weakening constraint of the matrix on the reinforcements during plastic deformation, Berveiller and Zaoui (1978) proposed an expression of the effective stress in the inclusion for the single inclusion problem, which is

$$\bar{\boldsymbol{\sigma}}_1 = \bar{\boldsymbol{\sigma}}_0 - \mathbf{C}_0^s : \left(\bar{\boldsymbol{\varepsilon}}_1 - \bar{\boldsymbol{\varepsilon}}_0\right) \tag{5.14}$$

where $\bar{\boldsymbol{\sigma}}_1$ and $\bar{\boldsymbol{\sigma}}_0$ are the volume averaged stress in the inclusion and the matrix, respectively, $\bar{\boldsymbol{\varepsilon}}_1$ and $\bar{\boldsymbol{\varepsilon}}_0$ are the corresponding averaged strain, and $\mathbf{C}_0^s$ is the secant stiffness tensor in the matrix, defined as:

$$\mathbf{C}_0^{*s} : \mathbf{S}_0^s = \mathbf{C}_0^s : \left(\mathbf{I} - \mathbf{S}_0^s\right) \tag{5.15}$$

with $\mathbf{S}_0^s$ be the secant Eshelby tensor, which is obtained by replacing the elastic moduli in the Eshelby tensor with the secant moduli of the matrix under plastic deformation. In the subsequent discussions, superscript *s* denotes the secant moduli related properties. It is noted that the Berveiller and Zaoui's approach is a simplification of the Hill's study under a monotonic and proportional loading, the secant moduli and the deformation theory is adopted in describing the plastic behavior. In line with this approach, Tandon and Weng (1988), based on the Mori-Tanaka method and the Eshelby's equivalent inclusion principle, showed the corresponding expression for multi-particle reinforced inhomogeneous composite as:

$$\bar{\boldsymbol{\sigma}}_1 = \mathbf{C}_1 : \left(\bar{\boldsymbol{\varepsilon}}_0 + \bar{\boldsymbol{\varepsilon}}^{pt}\right) = \mathbf{C}_0^s : (\bar{\boldsymbol{\varepsilon}}_0 + \bar{\boldsymbol{\varepsilon}}^{pt} - \bar{\boldsymbol{\varepsilon}}^{*}) \tag{5.16}$$

where $\bar{\boldsymbol{\varepsilon}}^{pt}$ is the averaged perturbed strain in the particle domain due to the interactions between particles, and $\boldsymbol{\varepsilon}^{*}$ is the eigenstrain from the Eshelby's equivalence. $\bar{\boldsymbol{\varepsilon}}^{pt}$ and $\boldsymbol{\varepsilon}^{*}$ are related through the secant Eshelby tensor as follows,

$$\bar{\boldsymbol{\varepsilon}}^{pt} = \mathbf{S}_0^s : \boldsymbol{\varepsilon}^{*} \tag{5.17}$$

However, when the interface energy effect is studied, perturbed strain due to the interface energy effect needs to be considered. As a consequence, instead of applying Eshelby's solution, we calculate the strain in the reinforcement phase by solving the continuity equations at the matrix-particle interface.

Since we are not considering the situation of interfacial debonding in the present chapter, it is reasonable to assume that the displacement through the matrix-particle interface is continuous, which leads to

$$[\mathbf{u}] = \mathbf{0} \tag{5.18}$$

where $\mathbf{u}$ is the displacement vector in the composite. It follows that the displacement gradient can be discontinuous through the interface from the matrix to the particle (Mura, 2013; Qu and Cherkaoui, 2006), that is, we have

$$[\mathbf{u}\nabla] = \boldsymbol{\lambda} \otimes \mathbf{n} \tag{5.19}$$

where $\boldsymbol{\lambda}$ is the vector that magnifies the discontinuity over the interface and $\mathbf{n}$ is the unit normal vector to the interface. Although discontinuity is revealed for the displacement gradient in Eq.

(5.19), it is necessary to mention that the displacement gradient is always continuous in the tangential direction at the interface. Further, the interfacial strain discontinuity is given as

$$[\boldsymbol{\varepsilon}]=\frac{1}{2}\left([\mathbf{u}\nabla]+[\nabla\mathbf{u}]\right)=\frac{1}{2}\left(\boldsymbol{\lambda}\otimes\mathbf{n}+\mathbf{n}\otimes\boldsymbol{\lambda}\right) \tag{5.20}$$

According to Mori and Tanaka (1973), each particle in the composite can be treated as a single particle surrounded by an effective matrix, whose strain field is assumed to be uniform and equals to the averaged strain $\bar{\boldsymbol{\varepsilon}}_0$ in the matrix phase. Therefore, strain in the spherical particle can be expressed as:

$$\boldsymbol{\varepsilon}_1=\bar{\boldsymbol{\varepsilon}}_0-[\boldsymbol{\varepsilon}] \tag{5.21}$$

Following Tandon and Weng (1988), the stress in the particle becomes,

$$\boldsymbol{\sigma}_1=\mathbf{C}_1:\boldsymbol{\varepsilon}_1=\mathbf{C}_0^s:(\bar{\boldsymbol{\varepsilon}}_0-[\boldsymbol{\varepsilon}]-\boldsymbol{\varepsilon}^*) \tag{5.22}$$

and the stress in the matrix is

$$\bar{\boldsymbol{\sigma}}_0=\mathbf{C}_0^s:\bar{\boldsymbol{\varepsilon}}_0 \tag{5.23}$$

which leads to the interfacial stress discontinuity,

$$[\boldsymbol{\sigma}]=\bar{\boldsymbol{\sigma}}_0-\boldsymbol{\sigma}_1=\mathbf{C}_0^s:\left([\boldsymbol{\varepsilon}]+\boldsymbol{\varepsilon}^*\right)=\mathbf{C}_0^s:\left(\boldsymbol{\lambda}\otimes\mathbf{n}+\boldsymbol{\varepsilon}^*\right) \tag{5.24}$$

Eshelby (1957, 1959, 1961) proved that the eigenstrain $\boldsymbol{\varepsilon}^*$ inside an ellipsoidal inclusion is uniform under far-field loading. For simplicity, we follow Eshelby's statement and assume eigenstrain remains uniform when the interface energy effect is considered. Substituting Eqs. (5.5) and (5.24) into Eq. (5.1) gives

$$\mathbf{C}_0^s:\left(\boldsymbol{\lambda}\otimes\mathbf{n}+\boldsymbol{\varepsilon}^*\right)\cdot\mathbf{n}=-\nabla_S\cdot\left(\mathbf{C}^{\mathrm{I}}:\boldsymbol{\varepsilon}^{\mathrm{I}}\right) \tag{5.25}$$

Eqs. (5.20) and (5.25) allow us to solve the interfacial strain discontinuity tensor, which renders

$$[\boldsymbol{\varepsilon}] = \mathbf{A}^s : \bar{\boldsymbol{\varepsilon}}_0 + \mathbf{B}^s : \boldsymbol{\varepsilon}^* \tag{5.26}$$

where $\mathbf{A}^s$ and $\mathbf{B}^s$ are the coefficient tensors that will change with the plastic flow. Since volume averaged strain and stress fields are desired in determining the effective properties, the volume averaged strain discontinuity tensor is solved as:

$$[\bar{\boldsymbol{\varepsilon}}] = \bar{\mathbf{A}}^s : \bar{\boldsymbol{\varepsilon}}_0 + \bar{\mathbf{B}}^s : \boldsymbol{\varepsilon}^* \tag{5.27}$$

where $\bar{\mathbf{A}}^s$ and $\bar{\mathbf{B}}^s$ are the volume averaged coefficient tensors,

$$\bar{A}^s_{ijkl} = \frac{1}{a}\left(\frac{3}{8}\frac{K^I+\mu^I}{M_0^s} - \frac{1}{4}\frac{K^I+\mu^I}{\mu_0^s}\right)\delta_{ij}\delta_{kl} + \frac{1}{a}\left(-\frac{1}{4}\frac{K^I+\mu^I}{M_0^s} + \frac{1}{2}\frac{K^I+\mu^I}{\mu_0^s}\right)\left(\delta_{ik}\delta_{jl}+\delta_{il}\delta_{jk}\right) \tag{5.28}$$

$$\bar{B}^s_{ijkl} = \left(-\frac{1}{3}\frac{K_0}{M_0^s} + \frac{4}{45}\frac{\mu_0^s}{M_0^s} + \frac{2}{15}\right)\delta_{ij}\delta_{kl} + \left(-\frac{4}{15}\frac{\mu_0^s}{M_0^s} - \frac{2}{5}\right)\left(\delta_{ik}\delta_{jl}+\delta_{il}\delta_{jk}\right) \tag{5.29}$$

and a is the radius of the spherical particle, M_0^s is the P-wave modulus, $M_0^s = K_0 + \frac{4}{3}\mu_0^s$. Then, the averaged strain in the particle phase becomes

$$\bar{\boldsymbol{\varepsilon}}_1 = \bar{\boldsymbol{\varepsilon}}_0 - [\bar{\boldsymbol{\varepsilon}}] = \left(\mathbf{I} - \bar{\mathbf{A}}^s\right) : \bar{\boldsymbol{\varepsilon}}_0 - \bar{\mathbf{B}}^s : \boldsymbol{\varepsilon}^* \tag{5.30}$$

and the corresponding averaged stress is revealed to be

$$\bar{\boldsymbol{\sigma}}_1 = \mathbf{C}_0^s : \left(\mathbf{I} - \bar{\mathbf{A}}^s\right) : \bar{\boldsymbol{\varepsilon}}_0 - \mathbf{C}_0^s : \bar{\mathbf{B}}^s : \boldsymbol{\varepsilon}^* \tag{5.31}$$

It is noted that the tensor $\bar{\mathbf{A}}^s$ is an isotropic tensor that is induced by the interface energy effect, it is affected by the interface stiffness, the size of the particle and the secant moduli of the matrix. Moreover, the components of $\bar{\mathbf{A}}^s$ decreases as the particle size increases, and they become zero if the interface energy effect is neglected ($K^I = \mu^I = 0$). On the other hand, the coefficient tensor $\bar{\mathbf{B}}^s$ is identical to the negative of the secant Eshelby tensor for a sphere. Therefore, Eq. (5.27) is

consistent with the classical micromechanical Mori-Tanaka solution when the interface energy effect is totally ignored.

5.3 Effective Secant Moduli of MMNCs

Based on the strain discontinuity tensor in previous section, the overall effective strain and stress of the composite are related, and the effective secant moduli can be determined accordingly. When the effective fields are considered, Eq. (5.22) becomes

$$\mathbf{C}_1 : \overline{\boldsymbol{\varepsilon}}_1 = \mathbf{C}_0^s : (\overline{\boldsymbol{\varepsilon}}_0 - [\overline{\boldsymbol{\varepsilon}}] - \boldsymbol{\varepsilon}^*) \tag{5.32}$$

from which the eigenstrain $\boldsymbol{\varepsilon}^*$ can be solved,

$$\boldsymbol{\varepsilon}^* = \left(\mathbf{I} + \overline{\mathbf{B}}^s\right)^{-1} : \left(\mathbf{I} - \overline{\mathbf{A}}^s\right) : \overline{\boldsymbol{\varepsilon}}_0 - \left(\mathbf{I} + \overline{\mathbf{B}}^s\right)^{-1} : \mathbf{C}_0^{s-1} : \mathbf{C}_1 : \overline{\boldsymbol{\varepsilon}}_1 \tag{5.33}$$

Then, substituting Eq. (5.33) into Eq. (5.30) renders

$$\overline{\boldsymbol{\varepsilon}}_1 = \mathbf{G}_1^s : \overline{\boldsymbol{\varepsilon}}_0 \tag{5.34}$$

where $\mathbf{G}_1^s$ is defined as:

$$\mathbf{G}_1^s = \left[\mathbf{I} + \overline{\mathbf{B}}^s : \left(\mathbf{I} - \mathbf{C}_0^{s\text{-}1} : \mathbf{C}_1\right)\right]^{-1} : \left(\mathbf{I} - \overline{\mathbf{A}}^s\right) \tag{5.35}$$

Further, the overall volume averaged strain reveals to be

$$\overline{\boldsymbol{\varepsilon}} = \left(1 - \phi_1\right)\overline{\boldsymbol{\varepsilon}}_0 + \phi_1 \overline{\boldsymbol{\varepsilon}}_1 = \mathbf{N}_1^{s-1} : \overline{\boldsymbol{\varepsilon}}_1 \tag{5.36}$$

where $\mathbf{N}_1^s$ is the strain concentration tensor,

$$\mathbf{N}_1^s = \mathbf{G}_1^s : \left[\left(1 - \phi_1\right)\mathbf{I} + \phi_1 \mathbf{G}_1^s\right]^{-1} \tag{5.37}$$

and the overall volume averaged stress takes the form

$$\overline{\boldsymbol{\sigma}} = \left(1 - \phi_1\right)\overline{\boldsymbol{\sigma}}_0 + \phi_1 \overline{\boldsymbol{\sigma}}_1 = \left[\mathbf{C}_0^s + \phi_1 \left(\mathbf{C}_1 - \mathbf{C}_0^s\right) : \mathbf{N}_1^s\right] : \overline{\boldsymbol{\varepsilon}} \tag{5.38}$$

which leads to the effective secant stiffness tensor

$$\bar{\mathbf{C}}^s = \mathbf{C}_0^s + \phi_1\left(\mathbf{C}_1 - \mathbf{C}_0^s\right) : \mathbf{N}_1^s \tag{5.39}$$

Consequently, the effective secant moduli are given as:

$$\bar{K}^s = K_0 + \frac{\phi_1\left(K_1 - K_0\right)\left(3M_0^s - 4K^I / a\right)}{3M_0^s + 3\left(1-\phi_1\right)\left(K_1 - K_0\right) - 4\phi_1 K^I / a} \tag{5.40}$$

$$\bar{\mu}^s = \mu_0^s + \frac{15\phi_1\mu_0^s\left(\mu_1 - \mu_0^s\right)M_0^s - \phi_1\left(\mu_1 - \mu_0^s\right)\left[2\left(3K_0 + 2\mu_0^s\right)K^I / a + 12M_0^s\mu^I / a\right]}{15\mu_0^s M_0^s + 6\left(1-\phi_1\right)\left(\mu_1 - \mu_0^s\right)\left(K_0 + 2\mu_0^s\right) - \phi_1\left[2\left(3K_0 + 2\mu_0^s\right)K^I / a + 12M_0^s\mu^I / a\right]} \tag{5.41}$$

Comparing the secant moduli in Eqs. (5.40)–(5.41), with that derived by Tandon and Weng in 1988, the size of the reinforcement particles and the interface stiffness are comprised. The micromechanical solutions can be obtained by neglecting the additional terms. Further, before any plastic deformation appears in the matrix, the superscript *s* can be dropped in all the terms to find the effective elastic moduli of the composite. Note that the effective secant moduli of the composite are expressed in terms of the secant moduli of the matrix. Therefore, in order to determine the effective secant moduli of the composite, it is essential to determine the secant moduli of the matrix.

It is acknowledged that $\bar{F}\left(\bar{\sigma}_0^*, \bar{\varepsilon}_0^{p*}\right) = 0$ during the development of plastic flow, which leads to

$$\bar{\sigma}_0^* = K\left(\bar{\varepsilon}_0^{p*}\right) \tag{5.42}$$

Substitution of Eq. (5.42) into Eq. (5.11) gives

$$E_0^s\left(\bar{\sigma}_0^*\right) = \frac{1}{\dfrac{1}{E_0} + \dfrac{K^{-1}\left(\bar{\sigma}_0^*\right)}{\bar{\sigma}_0^*}} \tag{5.43}$$

Therefore, secant moduli of the matrix can be obtained once $\bar{\sigma}_0^*$ is determined. Now, let us identify the expression of $\bar{\sigma}_0^*$ in terms of $\bar{\sigma}$. For brevity, we express the fourth order isotropic tensors using their volumetric and deviatoric factors; e.g., the coefficient tensors $\bar{\mathbf{A}}^s$ and $\bar{\mathbf{B}}^s$ are revealed to be

$$\bar{\mathbf{A}}^s = A^{\mathrm{v}}\mathbf{I}^{\mathrm{vol}} + A^{\mathrm{d}}\mathbf{I}^{\mathrm{dev}} = \left(A^{\mathrm{v}}, A^{\mathrm{d}}\right) \text{ and } \bar{\mathbf{B}}^s = B^v\mathbf{I}^{vol} + B^d\mathbf{I}^{dev} = \left(B^v, B^d\right) \tag{5.44}$$

where

$$A^{\mathrm{v}} = \frac{4}{3}\frac{K^I}{aM_0^s} \text{ and } A^{\mathrm{d}} = -\frac{4}{15}\frac{K^I}{aM_0^s} + \frac{2K^I + 4\mu^I}{5a\mu_0^s} \tag{5.45}$$

$$B^{\mathrm{v}} = -\frac{K_0}{M_0^s} \text{ and } B^{\mathrm{d}} = -\frac{4}{15}\frac{\mu_0^s}{M_0^s} - \frac{2}{5} \tag{5.46}$$

The relation between $\bar{\boldsymbol{\sigma}}_0$ and $\bar{\boldsymbol{\sigma}}$ can be established from Eqs. (5.23), (5.34), (5.36) and (5.38) that

$$\bar{\boldsymbol{\sigma}}_0 = \mathbf{P} : \bar{\boldsymbol{\sigma}} \tag{5.47}$$

where

$$\mathbf{P} = \left(P^{\mathrm{v}}, P^{\mathrm{d}}\right) = \left[\left(1-\phi_1\right)\mathbf{I} + \phi_1\mathbf{C}_1 : \mathbf{G}_1^s : \mathbf{C}_0^{s-1}\right]^{-1} \tag{5.48}$$

Therefore, the von Mises effective stress $\bar{\boldsymbol{\sigma}}_0^*$ in the matrix becomes

$$\bar{\sigma}_0^* = \left|P^{\mathrm{d}}\right|\sqrt{\frac{3}{2}\bar{\boldsymbol{\sigma}} : \mathbf{I}^{\mathrm{dev}} : \bar{\boldsymbol{\sigma}}} = \left|P^{\mathrm{d}}\right|\bar{\sigma}^* \tag{5.49}$$

where

$$P^{\mathrm{d}} = \frac{1}{1 + \phi_1\left(\frac{\mu_1}{\mu_0^s}G^{\mathrm{d}} - 1\right)} \tag{5.50}$$

$$G^{\mathrm{d}} = \frac{1 - A^{\mathrm{d}}}{1 + \left(1 - \dfrac{\mu_1}{\mu_0^s}\right) B^{\mathrm{d}}} \tag{5.51}$$

The relation is found between $\bar{\boldsymbol{\sigma}}_0^*$ and the prescribed far-field stress $\bar{\boldsymbol{\sigma}}$ (identical to the overall averaged stress in the composite), in which, however, $E_0^s\left(\bar{\boldsymbol{\sigma}}_0^*\right)$ is also involved. Therefore, iterations are usually required to find $\bar{\boldsymbol{\sigma}}_0^*$, provided that the far-field stress $\bar{\boldsymbol{\sigma}}$ is specified. Once $\bar{\boldsymbol{\sigma}}_0^*$ is determined, the corresponding overall effective secant moduli are readily available.

5.4 Results and Discussions

In order to illustrate the present nanomechanical framework, in a context which is as simple as possible, the example of the aluminum matrix composite containing nanovoids under uniaxial loading is considered here. The far-field applied uniaxial stress can be presented as

$$\bar{\boldsymbol{\sigma}} = \begin{pmatrix} \bar{\sigma}_{11} & 0 & 0 \\ 0 & 0 & 0 \\ 0 & 0 & 0 \end{pmatrix} \tag{5.52}$$

The mechanical properties of the matrix, the reinforcements and the matrix-reinforcement interface are exhibited in Table 5−1. The interface properties are obtained through molecular dynamic simulations (Miller and Shenoy, 2000; Sharma and Dasgupta, 2002; Duan et al., 2005).

Table 5–1 The elastic moduli of the matrix, the reinforcements and the interface

Phase	Material	Symbol	Value
Matrix	Aluminum	K_0	75.2 GPa
		μ_0	34.7 GPa
Reinforcement	Spherical Voids	K_1	0 GPa
		μ_1	0 GPa
Interface	[1 0 0] surface	K_1^{I}	-5.457 N/m
		μ_1^{I}	-6.2178 N/m
	[1 1 1] surface	K_2^{I}	12.932 N/m
		μ_2^{I}	-0.3755 N/m

Further, the power-law type plastic hardening rule is adopted here. Then, Eq. (5.40) becomes

$$\bar{\sigma}_0^* = \sigma_y + h\left(\bar{\varepsilon}_0^{p*}\right)^q \tag{5.53}$$

where σ_y is the initial yield stress, h and q are the material constants related to the plastic hardening behavior of the matrix material. The numbers of the material constants during plastic hardening are chosen as $\sigma_y = 46$ MPa, $h = 320$ MPa and $q = 0.265$ for illustration purpose. Due to the lack of experimental data on the plastic behavior of MMNCs, comparisons are made between the solutions under current nanomechanical framework and under the classical micromechanics

theory. The secant moduli $\bar{K}^{s*}$ and $\bar{\mu}^{s*}$, which are normalized w.r.t. the micromechanical solutions, are displayed on Fig. 5-1 to Fig. 5-4 at the volume fraction $\phi_1 = 0.2$, where $\bar{K}^{s*} = \left(\bar{K}^{s}\right)^{\text{nano}} / \left(\bar{K}^{s}\right)^{\text{micro}}$ and $\bar{\mu}^{s*} = \left(\bar{\mu}^{s}\right)^{\text{nano}} / \left(\bar{\mu}^{s}\right)^{\text{micro}}$.

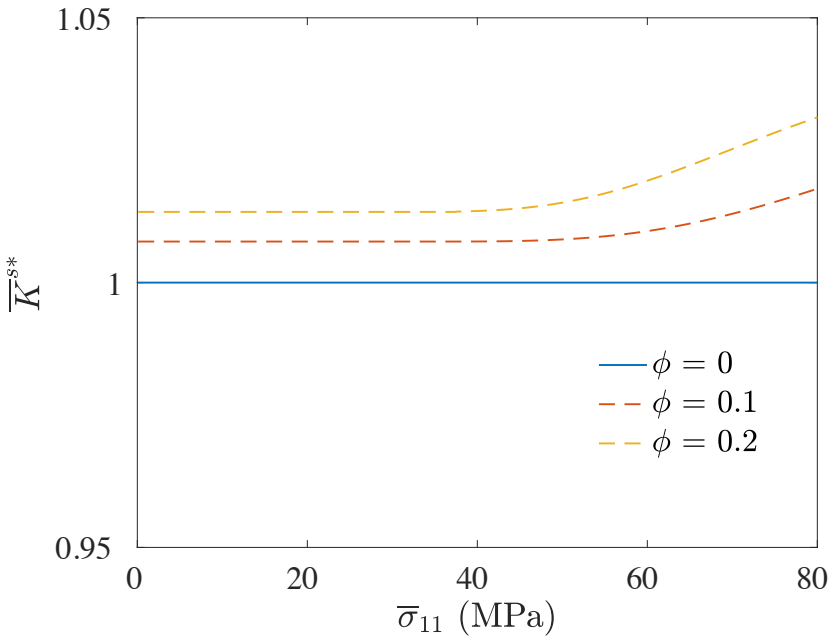

Figure 5–1 The change of normalized effective secant bulk modulus under different volume fraction of voids vs. the increase of external loading - interface [1 1 1]

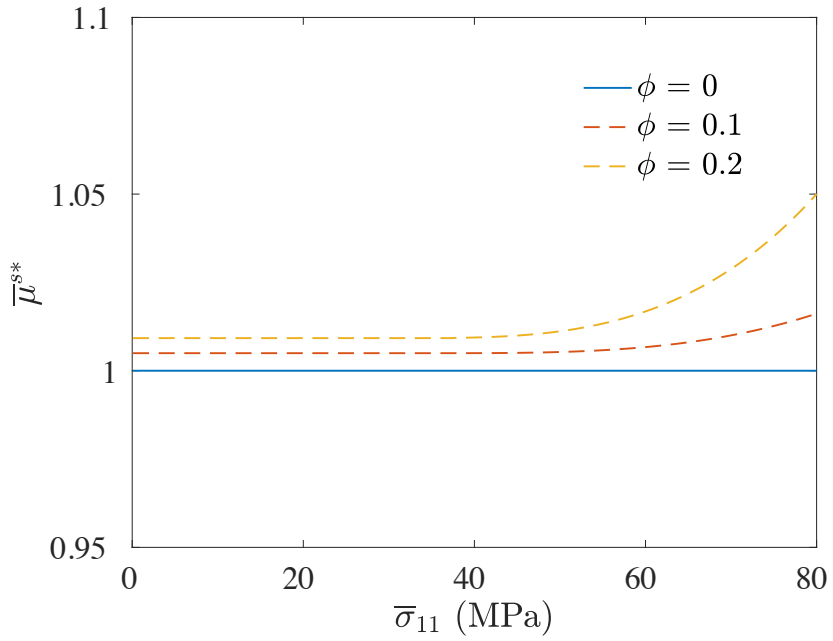

Figure 5–2 The change of normalized effective secant shear modulus under different volume fraction of voids vs. the increase of external loading - interface [1 1 1]

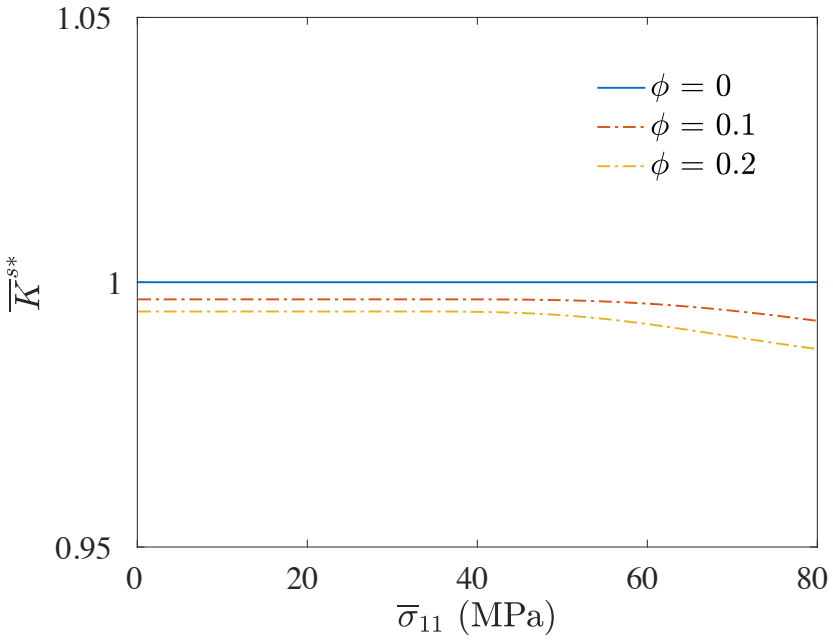

Figure 5–3 The change of normalized effective secant bulk modulus under different volume fraction of voids vs. the increase of external loading - interface [1 0 0]

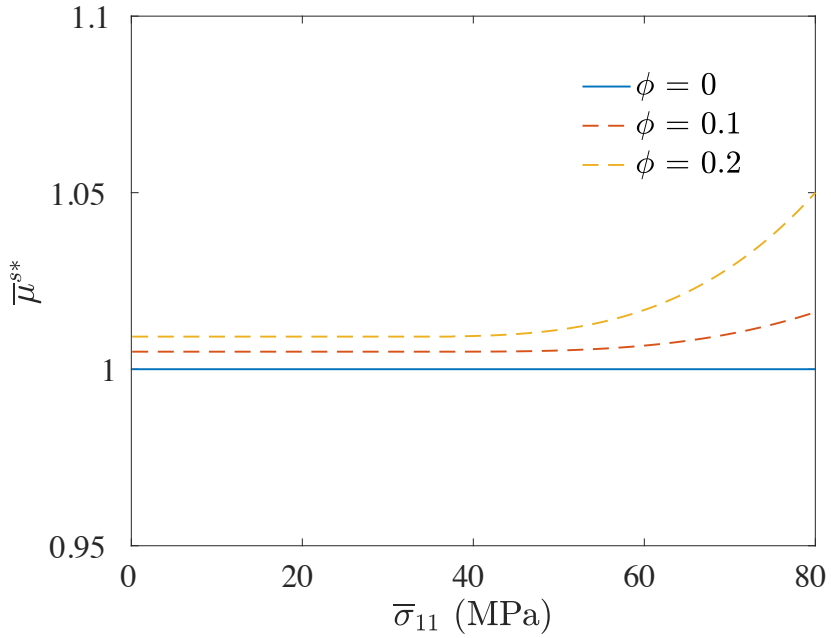

Figure 5–4 The change of normalized effective secant shear modulus under different volume fraction of voids vs. the increase of external loading - interface [1 0 0]

It is observed that the interface energy effect on the effective moduli remains constant before yielding, and it decreases as the size of the voids increases. Under the specified interface properties in Table 5-1, the effect of interface energy becomes very small when the particle size exceeds 20 nm in the elastic range. After yielding, we can see the continuous increasing on the interface energy effect with the increasing of the size of the voids. This phenomenon is due to two factors: 1. the interface energy plays a more important role in the composite with the continuously weakening matrix, 2. we assume that the interface properties are independent of the plastic flow in this chapter for brevity, while future study can be done on the change of interface properties with the weakening of the matrix material during the increase of the plastic flow. Further, even though the

different interface properties corresponding to [1 0 0] interface and [1 1 1] interface lead to opposite effects on the effective moduli, similar trends are noticed.

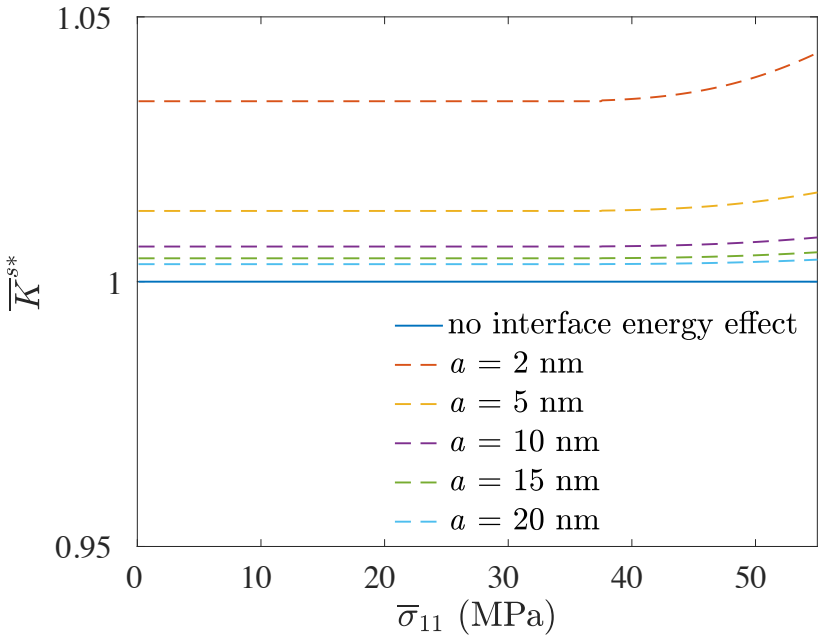

Figure 5–5 The change of normalized effective secant bulk modulus with different particle size vs. the increase of external loading - interface [1 1 1], $\phi = 0.2$.

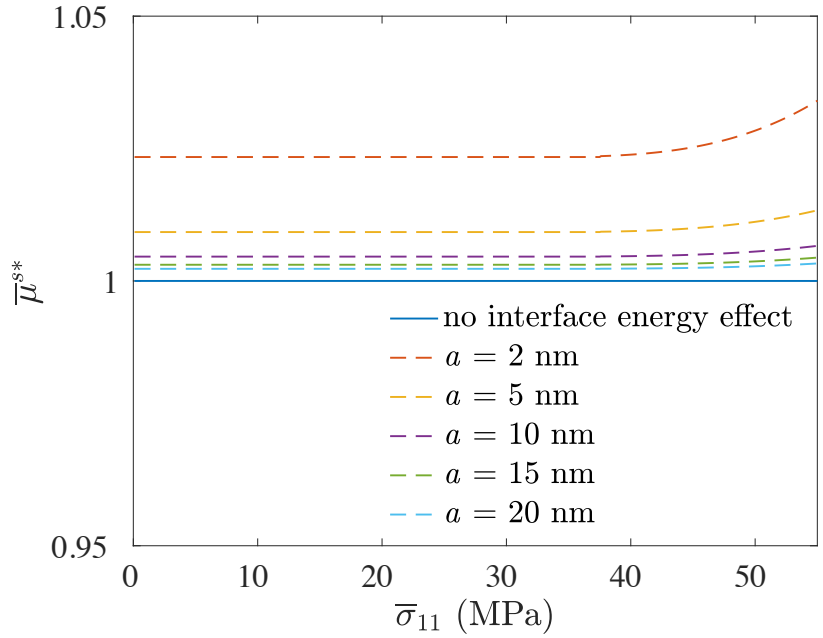

Figure 5–6 The change of normalized effective secant shear modulus with different particle size vs. the increase of external loading - interface [1 1 1], $\phi = 0.2$.

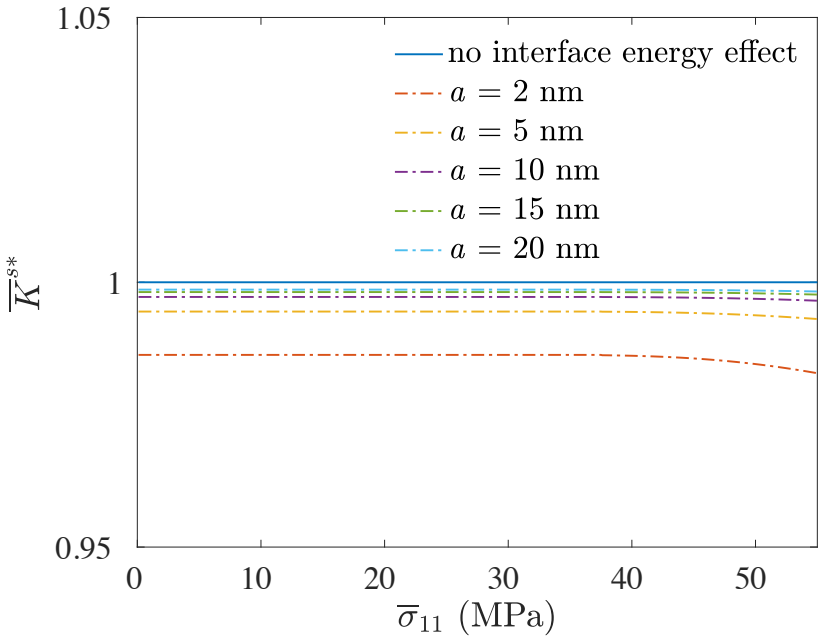

Figure 5–7 The change of normalized effective secant bulk modulus with different particle size vs. the increase of external loading - interface [1 0 0], $\phi = 0.2$.

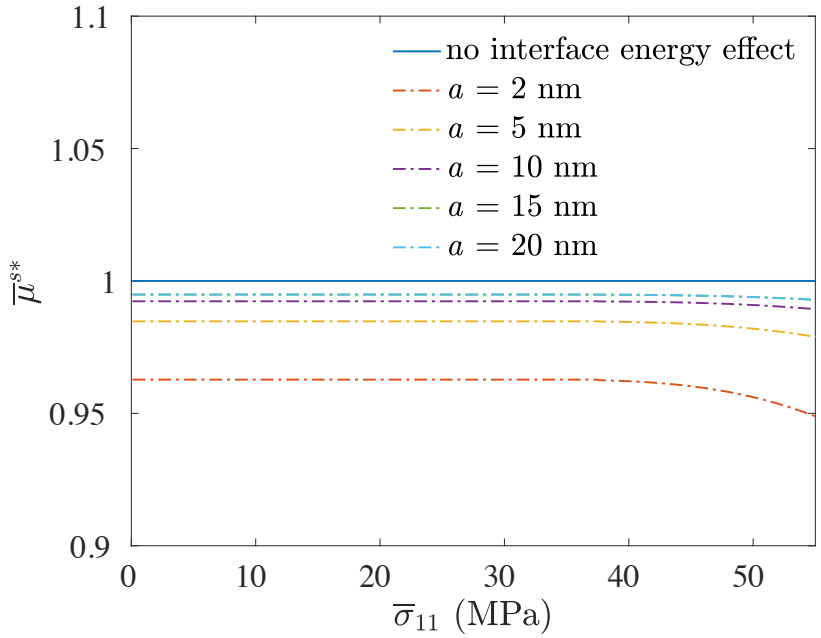

Figure 5–8 The change of normalized effective secant shear modulus with different particle size w.r.t. the increase of external loading - interface [1 0 0], $\phi = 0.2$.

The dependence of the normalized effective bulk modulus and shear modulus, $\overline{K}^{s*}$ and $\overline{\mu}^{s*}$, upon the volume fraction of voids are presented in Fig. 5-5 to Fig. 5-8 for both [1 0 0] and [1 1 1] interfaces with the radius of voids a = 10 nm. The present nanomechanical solutions at volume fractions $\phi_1 = 0, 0.1, 0.2$ are compared with their corresponding micromechanical solutions. $\phi_1 = 0$ represents the matrix-only material, where no matrix-particle interface exists. Therefore, the solutions under current nanomechanical framework match with the micromechanical solutions. Comparing the curves for various volume fractions, it is noticeable that the interface energy has larger effect on the effective moduli for the nanocomposite with higher reinforcement phase volume fraction.

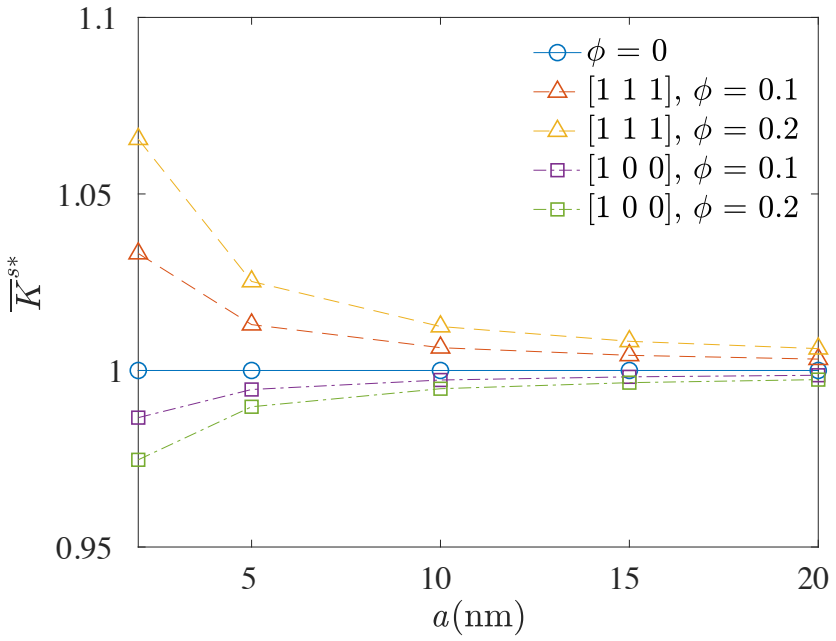

Figure 5–9 The effect of total interface area on the effective secant bulk modulus.

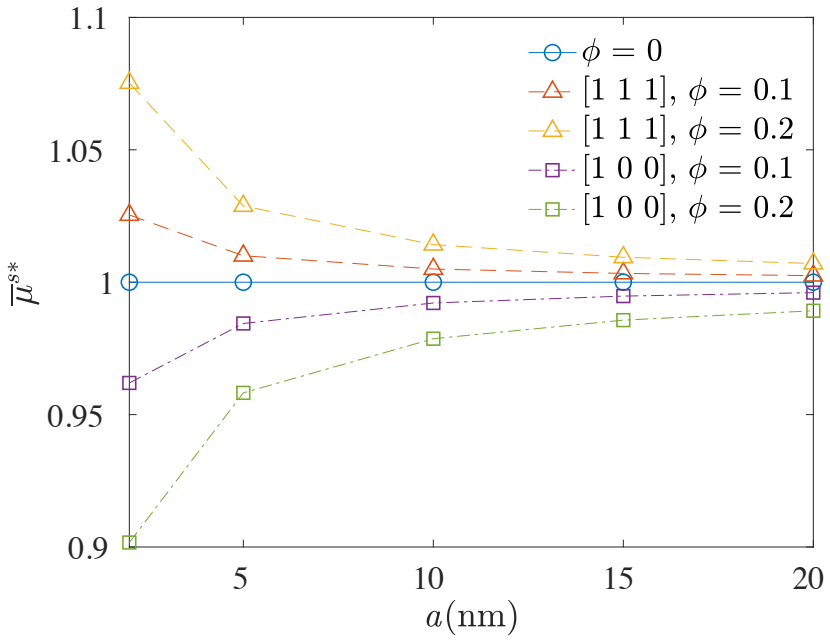

Figure 5–10 The effect of total interface area on the effective secant shear modulus.

It is known that both the decreasing of the particle size at a certain volume fraction and the increasing of the volume fraction at a fixed particle size lead to the increase of the total interface area in the composite. Therefore, the effect of interface energy on the effective moduli is positively related to the total interface area in the composite, which is displayed on Fig. 5-9 and Fig. 5-10.

Due to the lack of available and reliable experimental data on the present topic at this stage, experimental validation is not performed here. Comparisons are performed between our framework with the classical micromechanical solutions, and the comparisons with experimental data will be made when related experimental data become available in the future. In addition, the interface properties, which are determined by the microstructure at the matrix-particle interface, are different for different composite materials.

5.5 Closure

In this chapter, a nanomechanical framework is presented to predict the effective elastoplastic behavior of the two-phase spherical particle reinforced metal matrix nanocomposite. The effective secant moduli are predicted by introducing the interface energy effect to the classical micromechanical elastoplastic framework. A zero-thickness interphase between the matrix and the reinforcement is adopted to simulate the effect of interface energy, and the interfacial stress continuity equations are formulated accordingly. By solving the continuity equations at the interface and applying the assumptions on the effective fields by Mori and Tanaka (1973), the effective stress and strain fields are correlated between the reinforcement and its surrounding

matrix. Further, an effective yield criterion is considered for the matrix material (Ju and Chen, 1994c), and the Mori-Tanaka strategy (Tandon and Weng, 1988) is followed in estimating the effective secant moduli.

The proposed framework allows the prediction of the effective secant moduli of the two-phase spherical particle reinforced metal matrix composite, where the reinforcement particles are randomly distributed in the matrix and the matrix is elastoplastic while the particles are elastic. Comparisons are made between the present nanomechanical framework with the classical micromechanical solutions. The size effect is noticed on the effective secant moduli, and the total interface area in the composite is revealed to be positively related to the effect of interface energy. When the dimensions of reinforcement approach micrometer scale, the effect of interface energy becomes negligible and our nanomechanical solutions will obtain the classical micromechanical solutions.

Finally, it should be noted that this chapter is aimed at providing a simple and analytical framework in predicting the elastoplastic behavior of MMNCs and exploring the interface energy effect on the effective secant moduli compared with classical micromechanical solutions. Simplifications are made in the derivations, such as employing the volume averaged stress and strain fields in the matrix and in the reinforcements and assuming constant interfacial properties during the plastic flow. Further, the solutions are only compared with the classical solutions in section 5.4 due to the lack of available experimental data in this topic. Assessments and validations of present framework against reliable experimental data are warranted in the future.

5.6 References

Berveiller, M., & Zaoui, A. (1978). An extension of the self-consistent scheme to plastically-flowing polycrystals. *Journal of the Mechanics and Physics of Solids*, *26*(5-6), 325-344.

Bottomley, D. J., & Ogino, T. (2001). Alternative to the Shuttleworth formulation of solid surface stress. Physical Review B, 63(16), 165412.

Cammarata, R. C. (1997). Surface and interface stress effects on interfacial and nanostructured materials. Materials Science and Engineering: A, 237(2), 180-184.

Casati, R., & Vedani, M. (2014). Metal matrix composites reinforced by nano-particles—a review. Metals, 4(1), 65-83.

Castañeda, P. P. (1991). The effective mechanical properties of nonlinear isotropic composites. Journal of the Mechanics and Physics of Solids, 39(1), 45-71.

Castaneda, P. P. (1992). Bounds and estimates for the properties of nonlinear heterogeneous systems. Philosophical Transactions of the Royal Society of London. Series A: Physical and Engineering Sciences, 340(1659), 531-567.

Castañeda, P. P. (1996). Exact second-order estimates for the effective mechanical properties of nonlinear composite materials. Journal of the Mechanics and Physics of Solids, 44(6), 827-862.

Deng, C. F., Wang, D. Z., Zhang, X. X., & Ma, Y. X. (2007). Damping characteristics of carbon nanotube reinforced aluminum composite. Materials letters, 61(14-15), 3229-3231.

Duan, H. L., Wang, J. X., Huang, Z. P., & Karihaloo, B. L. (2005). Size-dependent effective elastic constants of solids containing nano-inhomogeneities with interface stress. Journal of the Mechanics and Physics of Solids, 53(7), 1574-1596.

Ferkel, H., & Mordike, B. L. (2001). Magnesium strengthened by SiC nanoparticles. Materials Science and Engineering: A, 298(1-2), 193-199.

Gibbs, J. W. (1906). The scientific papers of J. Willard Gibbs (Vol. 1). Longmans, Green and Company.

Gu, D., Hagedorn, Y. C., Meiners, W., Wissenbach, K., & Poprawe, R. (2011). Nanocrystalline TiC reinforced Ti matrix bulk-form nanocomposites by Selective Laser Melting (SLM): Densification, growth mechanism and wear behavior. Composites Science and Technology, 71(13), 1612-1620.

Gurtin, M. E., & Murdoch, A. I. (1975). A continuum theory of elastic material surfaces. Archive for Rational Mechanics and Analysis, 57(4), 291-323.

Hill, R. O. D. N. E. Y. (1965). Continuum micro-mechanics of elastoplastic polycrystals. Journal of the Mechanics and Physics of Solids, 13(2), 89-101.

Hutchinson, J. W. (1970). Elastic-plastic behaviour of polycrystalline metals and composites. Proceedings of the Royal Society of London. A. Mathematical and Physical Sciences, 319(1537), 247-272.

Hutchinson, J. W. (1976). Bounds and self-consistent estimates for creep of polycrystalline materials. Proceedings of the Royal Society of London. A. Mathematical and Physical Sciences, 348(1652), 101-127.

Ju, J. W., & Chen, T. M. (1994a). Micromechanics and effective moduli of elastic composites containing randomly dispersed ellipsoidal inhomogeneities. Acta Mechanica, 103(1-4), 103-121.

Ju, J. W., & Chen, T. M. (1994b). Effective elastic moduli of two-phase composites containing randomly dispersed spherical inhomogeneities. Acta Mechanica, 103(1-4), 123-144.

Ju, J. W., & Chen, T. M. (1994c). Micromechanics and effective elastoplastic behavior of two-phase metal matrix composites. Journal of engineering materials and technology, 116(3), 310-318.

Ju, J. W., & Tseng, K. H. (1996). Effective elastoplastic behavior of two-phase ductile matrix composites: a micromechanical framework. International Journal of Solids and Structures, 33(29), 4267-4291.

Ju, J. W., & Tseng, K. H. (1997). Effective elastoplastic algorithms for ductile matrix composites. Journal of engineering mechanics, 123(3), 260-266.

Ju, J. W., & Sun, L. Z. (2001). Effective elastoplastic behavior of metal matrix composites containing randomly located aligned spheroidal inhomogeneities. Part I: micromechanics-based formulation. International Journal of Solids and Structures, 38(2), 183-201.

Lagoudas, D. C., Gavazzi, A. C., & Nigam, H. (1991). Elastoplastic behavior of metal matrix composites based on incremental plasticity and the Mori-Tanaka averaging scheme. Computational Mechanics, 8(3), 193-203.

Lan, J., Yang, Y., & Li, X. (2004). Microstructure and microhardness of SiC nanoparticles reinforced magnesium composites fabricated by ultrasonic method. Materials Science and Engineering: A, 386(1-2), 284-290.

Li, X., Yang, Y., & Cheng, X. (2004). Ultrasonic-assisted fabrication of metal matrix nanocomposites. Journal of Materials Science, 39(9), 3211-3212.

Luo, P. E. N. G., McDonald, D. T., Xu, W., Palanisamy, S., Dargusch, M. S., & Xia, K. E. N. O. N. G. (2012). A modified Hall–Petch relationship in ultrafine-grained titanium recycled from chips by equal channel angular pressing. Scripta Materialia, 66(10), 785-788.

Miller, R. E., & Shenoy, V. B. (2000). Size-dependent elastic properties of nanosized structural elements. Nanotechnology, 11(3), 139.

Mori, T., & Tanaka, K. (1973). Average stress in matrix and average elastic energy of materials with misfitting inclusions. Acta metallurgica, 21(5), 571-574.

Mura, T. (2013). Micromechanics of defects in solids. Springer Science & Business Media.

Qu, J., & Cherkaoui, M. (2006). Fundamentals of micromechanics of solids (pp. 226-240). Hoboken: Wiley.

Sanaty-Zadeh, A. (2012). Comparison between current models for the strength of particulate-reinforced metal matrix nanocomposites with emphasis on consideration of Hall–Petch effect. Materials Science and Engineering: A, 531, 112-118.

Sharma, P., & Dasgupta, A. (2002). Average elastic fields and scale-dependent overall properties of heterogeneous micropolar materials containing spherical and cylindrical inhomogeneities. Physical Review B, 66(22), 224110.

Shehata, F. A. R. O. U. K., Fathy, A., Abdelhameed, M., & Moustafa, S. F. (2009). Preparation and properties of Al2O3 nanoparticle reinforced copper matrix composites by in situ processing. Materials & Design, 30(7), 2756-2762.

Tandon, G. P., & Weng, G. J. (1988). A theory of particle-reinforced plasticity. Journal of Applied Mechanics, 55(1), 126-135.

Trojanová, Z., Lukáč, P., Ferkel, H., & Riehemann, W. (2004). Internal friction in microcrystalline and nanocrystalline Mg. Materials Science and Engineering: A, 370(1-2), 154-157.

Tu, J. P., Wang, N. Y., Yang, Y. Z., Qi, W. X., Liu, F., Zhang, X. B., ... & Liu, M. S. (2002). Preparation and properties of TiB2 nanoparticle reinforced copper matrix composites by in situ processing. Materials Letters, 52(6), 448-452.

Voyiadjis, G., & Ju, J. W. (Eds.). (1994). Inelasticity and micromechanics of metal matrix composites (Vol. 41). Elsevier

Weng, G. J. (1990). The overall elastoplastic stress-strain relations of dual-phase metals. Journal of the Mechanics and Physics of Solids, 38(3), 419-441.

Yue, N. L., Lu, L., & Lai, M. O. (1999). Application of thermodynamic calculation in the in-situ process of Al/TiB2. Composite structures, 47(1-4), 691-694.

Zhang, Z., & Chen, D. L. (2006). Consideration of Orowan strengthening effect in particulate-reinforced metal matrix nanocomposites: A model for predicting their yield strength. Scripta Materialia, 54(7), 1321-1326.

Zhang, Z., & Chen, D. L. (2008). Contribution of Orowan strengthening effect in particulate-reinforced metal matrix nanocomposites. Materials Science and Engineering: A, 483, 148-152.

- Chapter 6 -

EFFECTIVE ELASTOPLASTIC DAMAGE MECHANICS FOR FIBER REINFORCED NANOCOMPOSITES WITH EVOLUTIONARY INTERFACE DEBONDING

Abstract

A nanomechanical evolutionary damage framework is presented to predict the effective elastoplastic damage behavior of the two-phase continuous circular-fiber reinforced nanocomposites. Under the transverse loading uniformly distributed along the longitudinal direction, the interface debonding is considered between the randomly distributed, unidirectionally aligned circular-fibers and the surrounding matrix. By assuming uniform interface debonding along the fibers, the effective properties are investigated under the plane strain condition. Additionally, since the nanosized fibers are studied, the interface energy effect is incorporated in the present model. The fibers under three bonding modes; i.e., the perfectly bonded fibers, the partially debonded fibers and the completely debonded fibers, are considered at the same time, and the corresponding volume fractions are predicted by the Weibull's distribution function. Further, based on the debonding angle, the debonded isotropic fibers are regarded as perfectly bonded orthotropic fibers, and the *two*-phase composite with the interface debonding is equivalented into a *four*-phase composite without any interface debonding. The interface energy effect, which is

assumed to induce the interface stress in the zero-thickness membrane-type interphase, is considered on the equivalented four-phase nanocomposite, and the stress discontinuity equations through interface are formulated in accordance with the equilibrium conditions of the idealized interphase. Subsequently, the effective elastic stiffness is derived. Furthermore, to characterize the elastoplastic behavior, we assume that the reinforcement phases are elastic, and the matrix phase is elastoplastic. An effective yield function is then proposed to estimate the effective elastoplastic responses of the fiber reinforced nanocomposite. Finally, the prediction of the elastoplastic damage behavior for a two-phase continuous fiber reinforced nanocomposite under the biaxial loading is presented for illustration, where notable size effect is observed.

6.1 Introduction

Composite materials, which consist two or more different constituent phases, possess distinct properties than any of their components. Desirable properties can be obtained by combining the different phases in the composite, such as low density, high stiffness, high performance at elevated temperatures, good design flexibility, etc. The most common types of the composite materials include the particle reinforced composites, the short fiber reinforced composites and the continuous fiber reinforced composites. The continuous fiber reinforced composites are the composite materials with continuous reinforcement fibers unidirectionally aligned in the matrix. Compared with other types of the composite materials, the continuous fiber reinforced composite

is highly anisotropic and shows notably high stiffness and strength in the longitudinal direction, which are usually preferred when the directionality is considered.

The strength in the transverse directions of the continuous fiber reinforced composites is much lower than the longitudinal direction. In the transverse directions, loading is transferred from the matrix to the fibers through the interface. Hence, the bonding strength of the interface is essential in the load carrying ability of the composite when the transverse loading is applied. Further, it is well-known that, for certain types of composites; e.g., the metal matrix composites, the interface bonding strength could be relatively low. Hence, the interface tends to be easily debonded under transverse loading (Simo and Ju, 1987a,b; Aboudi, 1987; Ju, 1989a,b; Pagano and Tandon, 1990; Zhao and Weng, 1997; Zhao and Weng, 2002; Ju and Lee, 2000; Ju and Lee, 2001; Matous, 2003; Sun, Ju and Liu, 2003; Liu, Sun and Ju, 2004; Liu, Sun and Ju, 2006; Ko, 2005; Paulino, Yin and Sun, 2006; Lee and Ju, 2007; Ju and Ko, 2008; Ju, Ko and Ruan, 2006; Ju, Ko and Ruan, 2008; Ju, Ko and Zhang, 2009; Rinaldi, Krajcinovic and Mastilovic, 2007; Voyiadjis, Kattan and Taqieddin, 2007; Ju and Yanase, 2009). When the debonding initiates, the transverse strength of the composite is significantly reduced, which greatly limits the practical applications of the composite. Therefore, studying the interface debonding in the fiber reinforced composite is of great importance.

When one or more dimensions of the reinforcement phase is/are in the nanometer scale, the composite can be seen as a nanocomposite. For the continuous fiber reinforced nanocomposite, the transverse dimensions are in the nanometer scale. With the advancement in the nanotechnology,

nanocomposites have attracted more and more attentions recently. Compared with the conventional composites, nanocomposites can achieve numerous desirable properties, such as better damping capacity, better wear resistance, higher temperature creep resistance and longer fatigue, etc life (Trojanova et al., 2004; Deng et al., 2007; Shehata et al., 2009; Ferkel and Mordike, 2001). It is noted that, due to the significantly larger gross interface area in the nanocomposite, the effect of interface energy, which is totally neglected for conventional composites, needs to be considered. Here, interface energy is defined as the excess free energy at the interface due to the different local atomic environment at interface than in the bulk material (Gibbs, 1906). The interface energy changes when the interface is deformed. Consequently, the elastic fields near the interface are perturbed. To characterize the effect of interface energy during the deformation, Gurtin and Murdoch (1975) established an interface model that treats the interface as a zero-thickness interphase in between the matrix and the reinforcement. According to the membrane theory, they derived the interfacial continuity equations, which are also referred to as the *generalized* Young-Laplace equations. In the *generalized* Young-Laplace equations, a new concept 'interface stress' is introduced. Interface stress, which is defined as the force per unit length along the edge of an idealized interphase membrane element, is induced in order to simulate the perturbation on the elastic fields due to the interface energy. Even though the effect of interface energy is usually neglected for the reinforcements in larger length scale, it is essential when the effective mechanical properties of the nanocomposites is considered (Cammarata, 1997).

Research on predicting the effective mechanical properties of the composite materials are well developed in the past few decades. Originated from the celebrated Eshelby tensor and equivalence principle (Eshelby, 1957, 1961), various micromechanics theories are formulated that tackle with the problem of determining the effective properties of the composites. Among others, the Mori-Tanaka method (Mori and Tanaka, 1973; Tandon and Weng, 1984; Weng, 1990), the Hashin-Shtrikman bounds (Hashin and Shitrikman, 1963), the self-consistent method (Hill, 1965; Budiansky, 1965) and the direct interaction model (Ju and Chen, 1994a, b, c) attract the most attention. However, classical micromechanics models, which considers the dimensions of the reinforcement phases in the micrometer or larger length scale, neglected the effect of interface energy. As a consequence, they are not directly applicable to the research on the nanocomposites, where the interface energy effect has to be considered. Currently, a few researchers studied the interface energy effect on the effective elastic properties for nanocomposites (Sharma et al., 2003; Sharma and Ganti, 2004; Duan et al., 2005a, b). However, predicting the elastoplastic behavior of the fiber reinforced nanocomposites with interfacial damage is still a new topic.

This chapter is focused on predicting the elastoplastic behavior of the continuous fiber-reinforced nanocomposites with interface debonding. The interface energy effect on the overall effective elastoplastic behavior is studied, and interface is simulated by the membrane interphase with the in-plane interface stress. Following Mori and Tanaka's assumption on the effective fields, the volume-averaged elastic fields are correlated through the interface continuity equations. As the increase of the external loading, progressive interface debonding is considered by the gradually

reduced stiffness, and the Weibull's probability function is incorporated to predict the damage volume fraction evolution. At the end, an effective yield function of the composite is proposed to predict the overall elastoplastic behavior.

6.2 Interface Debonding of Nano-fiber Reinforced Composite

Now consider a two-phase continuous fiber reinforced nanocomposite with all the fibers aligned in one direction. Since the radii of the fibers are assumed to be in nanometer scale, the effect of interface energy becomes an essential factor in the determination of the mechanical properties (Cammarata R. C., 1997). When perfectly bonded, the interface can be modeled by the zero-thickness membrane, which contains the in-plane interface stress, to simulate the interface energy effect (Duan et al., 2005c). Accordingly, the stress through the interface is discontinuous, and the discontinuity conditions can be determined from the equilibrium equations of the idealized membrane, which is also referred to as the *generalized* Young-Laplace equations, taking the form

$$[\boldsymbol{\sigma}]\cdot\mathbf{n} = -\nabla_S \cdot \boldsymbol{\tau} \tag{6.1}$$

where $[\boldsymbol{\sigma}]$ is the interfacial discontinuity of stress, $\mathbf{n}$ is the unit normal to the interface, $\nabla_S \cdot$ denotes the interface divergence, and $\boldsymbol{\tau}$ represents the interface stress. In what follows, the square bracket **[.]** is employed to represent the interfacial discontinuity of the said value. For circular fiber reinforced composite, the generalized Young-Laplace equations are

$$\left[\sigma_{rr}\right] = \frac{\tau_{\theta\theta}}{a} \tag{6.2}$$

$$\left[\sigma_{r\theta}\right] = -\frac{1}{a}\frac{\partial \tau_{\theta\theta}}{\partial \theta} \tag{6.3}$$

$$\left[\sigma_{rz}\right] = -\frac{1}{a}\frac{\partial \tau_{\theta z}}{\partial \theta} \tag{6.4}$$

where a is the radius of the circular cross-section of the fibers. To determine the interface stress $\boldsymbol{\tau}$, a linear isotrpic constitutive relation is adopted here. The relation between $\boldsymbol{\tau}$ and the interface strain $\boldsymbol{\varepsilon}^{\mathrm{I}}$, which is composed of the tangential components of the total strain at interface, can be presented as (Gurtin and Murdoch, 1975; Bottomley and Ogino, 2001; Miller and Shenoy, 2000; Duan et al., 2005b)

$$\boldsymbol{\tau} = \mathbf{C}_r^{\mathrm{I}} : \boldsymbol{\varepsilon}^{\mathrm{I}} \tag{6.5}$$

where

$$\mathbf{C}_r^{\mathrm{I}} = 2K_r^{\mathrm{I}}\mathbf{L}_{ijkl}^{\mathrm{v}} + 2\mu_r^{\mathrm{I}}\mathbf{L}_{ijkl}^{\mathrm{d}} \quad \text{for } i, j, k, l = 1,2 \tag{6.6}$$

$$\mathbf{L}_{ijkl}^{\mathrm{v}} = \frac{1}{2}\delta_{ij}\delta_{kl}\mathbf{e}_i \otimes \mathbf{e}_j \otimes \mathbf{e}_k \otimes \mathbf{e}_l \tag{6.7}$$

$$\mathbf{L}_{ijkl}^{\mathrm{d}} = \frac{1}{2}\left(\delta_{ik}\delta_{jl} + \delta_{jk}\delta_{il} - \delta_{ij}\delta_{kl}\right)\mathbf{e}_i \otimes \mathbf{e}_j \otimes \mathbf{e}_k \otimes \mathbf{e}_l \tag{6.8}$$

where $\mathbf{C}_r^{\mathrm{I}}$ is the interface elastic stiffness tensor of the rth phase reinforcements and K_r^{I}, μ_r^{I} are the corresponding interface bulk modulus and the interface shear modulus, respectively. When interface debonding initiates, the local atomic environment is changed, which leads to the change of the interfacial continuity conditions and the associated interface moduli. Neglecting the interface energy effect, Zhao and Weng (1997, 2002) proposed an equivalent approach that treat partially debonded reinforcements as perfectly bonded reinforcements with reduced stiffness. In the present study, following Zhao and Weng (1997, 2002), we assume that the interface of the equivalented fibers is perfectly bonded. Further, the interface moduli are assumed to be unchanged

for the equivalented fibers. Nevertheless, the current work can also take the reduction of interface moduli into consideration through simple modifications.

Debonding initiates when the stress at the matrix-fiber interface reaches a certain value, which leads to the reduced load transferring ability of the composite from the matrix to the fibers. Therefore, the debonding criterion is especially important to determine the bonding status during loading progress. Based on the notion that the normal traction t_n at the interface governs the debonding initiation, a debonding criterion by introducing a fixed debonding critical stress σ_{cri} at the interface is suggested, and debonding initiates once $t_n \geq \sigma_{cri}$ (Ju and Ko, 2008; Ju and Yanase, 2008). When the coordinates that coincide with the directions of the principle stresses are considered, as shown in Fig. 6-1, the normal traction on the interface is

$$t_n = \sigma_1 \cos^2\theta + \sigma_2 \sin^2\theta \tag{6.9}$$

Then, the debonding criterion can be displayed as

$$\sigma_1 \cos^2\theta + \sigma_2 \sin^2\theta \geq \sigma_{cri} \tag{6.10}$$

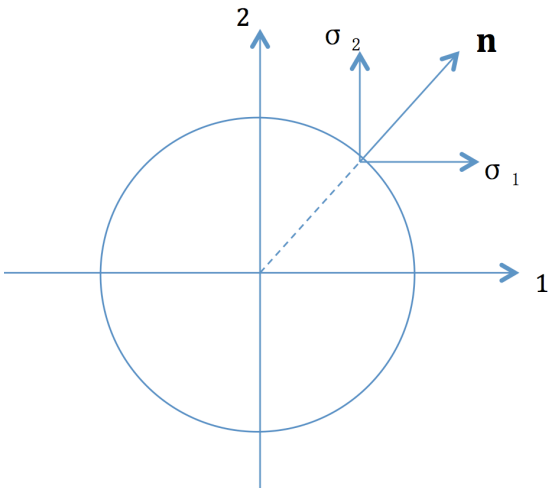

Figure 6–1 The normal direction and the principal stresses at the interface

To quantify the reduction of the stiffness during the debonding process, the concept of the equivalent damaged area is adopted, which is defined as the projected area from the debonded interface to the axis, and the ratios of the equivalent damaged area to the total cross-sectional area are selected as the damage parameters. The equivalent damaged areas in the directions that correspond to the principal stresses are presented in Fig. 6-2. Further, the damage parameter D_1 equals to the ratio of the equivalent damage area in direction 1 to the entire cross-sectional area, and the damage parameter D_2 equals to the ratio of the equivalent damage area in direction 2 to the entire cross-sectional area. Here, we assume that the transverse loading is uniform along the longitudinal direction, so that the debonding along the longitudinal direction is constant, and the damage parameter D_3 along the fibers is *zero*. Provided the principle stresses at interface, the damage parameters are given as,

$$D_1 = \frac{2\alpha + \sin 2\alpha}{\pi} \tag{6.11}$$

$$D_2 = \frac{2\alpha - \sin 2\alpha}{\pi} \tag{6.12}$$

$$D_3 = 0 \tag{6.13}$$

where $\alpha = \arcsin\sqrt{\frac{\sigma_1 - \sigma_{cri}}{\sigma_1 - \sigma_2}}$ is the debonding angle.

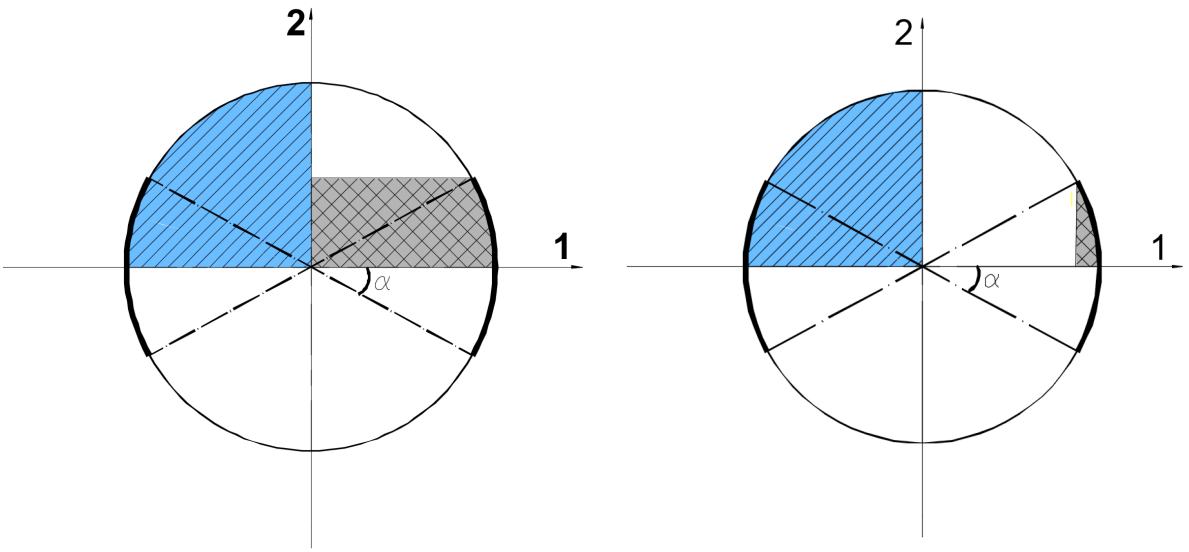

Figure 6–2 Debonding angle and the equivalent damage areas.

Following Zhao and Weng (1997, 2002), the debonded isotropic fibers can be equivalented into perfectly bonded orthotropic fibers with reduced stiffness. The stiffness tensor of the equivalented orthotropic fibers can be written as,

$$C_{ijkl} = \lambda_{IK}\delta_{ij}\delta_{kl} + \mu_{IJ}\left(\delta_{ik}\delta_{jl} + \delta_{il}\delta_{jk}\right) \text{ for } i, j, k, l, \text{ and } I, J, K = 1, 2, 3 \tag{6.14}$$

where $\lambda_{IK} = \lambda\left(1-D_I\right)\cdot\left(1-D_K\right)$ and $\mu_{IJ} = \mu\left(1-D_I\right)\cdot\left(1-D_J\right)$. Here, even though the upper-case and the lower-case indices share the same numbers, summation convention only applies to the lower-case indices.

Due to the sophisticated microstructure in the composite, including the spatial distributions of the fibers and the micro-geometries, the stress around each fiber varies. Therefore, instead of assuming that all the fibers are in the same bonding state, it is more reasonable to assume that the

fibers can have different bonding conditions. According to the bonding conditions, the fibers are generally classified into three phases: perfectly bonded fibers (phase 1), partially debonded fibers (phase 2) and completely debonded fibers (phase 3). After the debonding initiates, all of the three phases can exist in the composite at the same time, and they can be equivalented into perfectly bonded fibers with different elastic stiffness tensors, which can be described by Eq. (6.14). In addition, the phase 1 fibers have D_1=D_2=0, the phase 2 fibers are assumed to have the same debonding angle α that corresponds to the current stress state, and the damage parameters of the phase 3 fibers are equal to 1 in both transverse directions. Through the equivalence, the original two-phase nanocomposite with interface debonding is equivalented into a four-phase nanocomposite with all of the reinforcement phases perfectly bonded to the matrix, and Eqs. (6.2)–(6.4) can be solved under the equivalented properties directly. Further, the volume fraction of each phase is predicted by

$$P_d = 1 - \exp\left[-\left(\frac{\sigma_1 - \sigma_{cri}}{S_0} \right)^M \right],\ P_c = 0 \quad \text{for} \quad \sigma_1 \geq \sigma_{\text{cri}} \quad \text{and} \quad \sigma_2 < \sigma_{\text{cri}} \tag{6.15}$$

$$P_c = P_d = 1 - \exp\left[-\left(\frac{\sigma_1 - \sigma_{cri}}{S_0} \right)^M \right] \quad \text{for} \quad \sigma_1 \geq \sigma_2 \geq \sigma_{\text{cri}} \tag{6.16}$$

where P_d is the Weibull's probability function that denotes the probability of debonding (including partially debonded and completely debonded), M and S_0 are the constant parameters of the function, and P_c is the probability of being completely debonded. Therefore, the volume fractions for the reinforcement phases can be shown as

$$\phi_1 = \phi_T \left(1 - P_d \right) \tag{6.17}$$

$$\phi_2 = \phi_T \left(P_d - P_c \right) \tag{6.18}$$

$$\phi_3 = \phi_T P_c \tag{6.19}$$

where ϕ_T is the total volume fraction of fibers, and ϕ_1, ϕ_2, ϕ_3 are the volume fractions of phase 1, phase 2, phase 3 fibers, respectively.

It is noted that the linear isotropic assumption on the interface is applicable to the perfectly bonded interface and the free surface. Since the partially debonded fibers are equivalented into the perfectly bonded fibers, we assume that the interface is still linear isotropic for simplicity. However, the change of the interface elastic moduli has to be considered. Based on the debonding angle, the gradually changing interface elastic moduli of the partially debonded fibers are defined as

$$K_2^{\mathrm{I}} = \left(1 - \frac{2\alpha}{\pi} \right) K_1^{\mathrm{I}} + \frac{2\alpha}{\pi} K_3^{\mathrm{I}} \quad \text{and} \quad \mu_2^{\mathrm{I}} = \left(1 - \frac{2\alpha}{\pi} \right) \mu_1^{\mathrm{I}} + \frac{2\alpha}{\pi} \mu_3^{\mathrm{I}} \tag{6.20}$$

Eq. (6.20) presents a linear relation between the interface elastic moduli and the debonding angle. The more general relations can be applied if suitable experimental data or the results from numerical simulations become available.

6.3 Effective Elastic Stiffness

The effective elastic stiffness of the fiber-reinforced nanocomposite with interface debonding can be obtained by considering the effective elastic behavior of the equivalented four-phase fiber reinforced nanocomposite. According to Eshelby (1957, 1961), the equivalented perfectly bonded

fibers can be further equivalented into the matrix with eigenstrain in the original domain, which reads,

$$\boldsymbol{\sigma}_r = \mathbf{C}_r : \left(\boldsymbol{\varepsilon}_0 + \boldsymbol{\varepsilon}_r^{pt}\right) = \mathbf{C}_0 : (\boldsymbol{\varepsilon}_0 + \boldsymbol{\varepsilon}_r^{pt} - \boldsymbol{\varepsilon}_r^{*}) \tag{6.21}$$

where $\boldsymbol{\varepsilon}_r^{pt}$ is the perturbed strain in the reinforcement domain, $\boldsymbol{\varepsilon}_r^{*}$ is the stress-free eigenstrain originated from the Eshelby's equivalent inclusion principle, and the subscript r = 1, 2, 3 corresponds to the fibers in different bonding phases. To determine the perturbed strain $\boldsymbol{\varepsilon}_r^{pt}$, and thereby the eigenstrain $\boldsymbol{\varepsilon}_r^{*}$, classical micromechanics theories follow the Eshelby's solution (Eshelby, 1957, 1959). However, as discontinuity is induced to simulate the effect of interface energy, Eshelby's solution cannot be applied directly to the present study. Since the fibers with interface debonding is equivalented into perfectly bonded fibers with reduced stiffness, the displacement continuity conditions can be written as

$$\left[\mathbf{u}_r\right] = \mathbf{0} \tag{6.22}$$

where $\mathbf{u}_r$ is the displacement vector of the rth phase fibers. Consequently, the strain discontinuity through interface beocmes,

$$\left[\boldsymbol{\varepsilon}_r\right] = \frac{1}{2}\left(\left[\mathbf{u}_r\nabla\right] + \left[\nabla\mathbf{u}_r\right]\right) = \frac{1}{2}\left(\boldsymbol{\lambda}_r \otimes \mathbf{n} + \mathbf{n} \otimes \boldsymbol{\lambda}_r\right) \tag{6.23}$$

where $\boldsymbol{\lambda}_r$ denotes the magnitude of displacement gradient discontinuity over the interface from matrix to rth phase fibers, and $\mathbf{n}$ is the unit narmal vector to the interface. Following the assumption by Mori and Tanaka, the strain $\boldsymbol{\varepsilon}_r$ in the rth phase fibers reveals to be

$$\boldsymbol{\varepsilon}_r = \bar{\boldsymbol{\varepsilon}}_0 - \left[\boldsymbol{\varepsilon}_r\right] \tag{6.24}$$

where $\bar{\boldsymbol{\varepsilon}}_0$ is the volume-averaged strain in the effective matrix. Then, Eq. (6.21) becomes,

$$\boldsymbol{\sigma}_r = \mathbf{C}_r : \boldsymbol{\varepsilon}_r = \mathbf{C}_0 : (\bar{\boldsymbol{\varepsilon}}_0 - [\boldsymbol{\varepsilon}_r] - \boldsymbol{\varepsilon}_r^*) \tag{6.25}$$

Further, the volume-averaged stress in the matrix is

$$\bar{\boldsymbol{\sigma}}_0 = \mathbf{C}_0 : \bar{\boldsymbol{\varepsilon}}_0 \tag{6.26}$$

As a consequence, the interfacial stress discontinuity $[\boldsymbol{\sigma}_r]$ at the interface of the rth phase fibers is obtained, that is

$$[\boldsymbol{\sigma}_r] = \bar{\boldsymbol{\sigma}}_0 - \boldsymbol{\sigma}_r = \mathbf{C}_0 : ([\boldsymbol{\varepsilon}_r] + \boldsymbol{\varepsilon}_r^*) \tag{6.27}$$

Note that the eigenstrain in a single ellipsoidal inclusion is proved to be uniform when the interface energy effect is neglected (Eehslby, 1957, 1959, 1961). Here, for simplicity, we assume that the uniformity of the eigenstrain still holds when the effect of interface energy is incorporated. Substitution of Eqs. (6.5) and (6.27) into Eq. (6.1) gives,

$$\mathbf{C}_0 : ([\boldsymbol{\varepsilon}_r] + \boldsymbol{\varepsilon}_r^*) \cdot \mathbf{n} = -\nabla_S \cdot (\mathbf{C}_r^{\mathrm{I}} : \boldsymbol{\varepsilon}^{\mathrm{I}}) \tag{6.28}$$

from which $[\boldsymbol{\varepsilon}_r]$ can be solved

$$[\boldsymbol{\varepsilon}_r] = \mathbf{A}_r : \bar{\boldsymbol{\varepsilon}}_0 + \mathbf{B} : \boldsymbol{\varepsilon}_r^* \tag{6.29}$$

where $\mathbf{A}_r$ and $\mathbf{B}$ are the coefficient tensors. As the volume-averaged properties are desired, the volume-averaged strain discontinuity tensor is obtained as

$$[\bar{\boldsymbol{\varepsilon}}_r] = \bar{\mathbf{A}}_r : \bar{\boldsymbol{\varepsilon}}_0 + \bar{\mathbf{B}} : \boldsymbol{\varepsilon}_r^* \tag{6.30}$$

where $\bar{\mathbf{A}}_r$ and $\bar{\mathbf{B}}$ are the volume averaged coefficient tensors. The detailed expressions of $\bar{\mathbf{A}}_r$ and $\bar{\mathbf{B}}$ for the circular fibers are

$$(A_r)_{1111} = (A_r)_{2222} = \frac{K_r^{\mathrm{I}} + \mu_r^{\mathrm{I}}}{8a\left(K_0 + \frac{4}{3}\mu_0\right)} + \frac{K_r^{\mathrm{I}} + \mu_r^{\mathrm{I}}}{4a\mu_0} \qquad (A_r)_{1122} = (A_r)_{2211} = \frac{3\left(K_r^{\mathrm{I}} + \mu_r^{\mathrm{I}}\right)}{8a\left(K_0 + \frac{4}{3}\mu_0\right)} - \frac{K_r^{\mathrm{I}} + \mu_r^{\mathrm{I}}}{4a\mu_0}$$

$$(A_r)_{1133} = (A_r)_{2233} = \frac{K_r^{\mathrm{I}} - \mu_r^{\mathrm{I}}}{2a\left(K_0 + \frac{4}{3}\mu_0\right)} \qquad (A_r)_{1212} = \frac{1}{2}\left((A_r)_{1111} - (A_r)_{1122}\right)$$

$$(A_r)_{1313} = (A_r)_{2323} = \frac{\mu_r^{\mathrm{I}}}{2a\mu_0} \qquad (A_r)_{3333} = 0$$

$$B_{1111} = B_{2222} = -\frac{1}{4} - \frac{K_0}{2\left(K_0 + \frac{4}{3}\mu_0\right)} - \frac{5\mu_0}{12\left(K_0 + \frac{4}{3}\mu_0\right)}$$

$$B_{1122} = B_{2211} = \frac{1}{4} - \frac{K_0}{2\left(K_0 + \frac{4}{3}\mu_0\right)} + \frac{\mu_0}{12\left(K_0 + \frac{4}{3}\mu_0\right)}$$

$$B_{1133} = B_{2233} = -\frac{K_0}{2\left(K_0 + \frac{4}{3}\mu_0\right)} + \frac{\mu_0}{3\left(K_0 + \frac{4}{3}\mu_0\right)}$$

$$B_{1212} = \frac{1}{2}\left(B_{1111} - B_{1122}\right) \qquad B_{1313} = B_{2323} = -\frac{1}{2} \qquad B_{3333} = 0$$

where a is the radius of the circular fiber. It is observed from the above expressions that the tensor $\overline{\mathbf{A}}_r$ is depending upon the interface stiffness and the radius a of the circular fibers. Its components vanish when the interface elastic moduli are neglected ($K_r^{\mathrm{I}} = \mu_r^{\mathrm{I}} = 0$) or a goes to infinity. On the other hand, the tensor $\overline{\mathbf{B}}$ is identical to the negative of the Eshelby tensor for circular fibers. In addition, $\overline{\mathbf{A}}_r$ and $\overline{\mathbf{B}}$ are independent of the stiffness of the reinforcements. According to Eq. (6.30), the volume averaged strain and the volume averaged stress of the rth phase fibers are obtained,

$$\overline{\boldsymbol{\varepsilon}}_r = \overline{\boldsymbol{\varepsilon}}_0 - \left[\overline{\boldsymbol{\varepsilon}}_r\right] = \left(\mathbf{I} - \overline{\mathbf{A}}_r\right) : \overline{\boldsymbol{\varepsilon}}_0 - \overline{\mathbf{B}} : \boldsymbol{\varepsilon}_r^* \tag{6.31}$$

$$\overline{\boldsymbol{\sigma}}_r = \mathbf{C}_0 : \left(\mathbf{I} - \overline{\mathbf{A}}_r\right) : \overline{\boldsymbol{\varepsilon}}_0 - \mathbf{C}_0 : \overline{\mathbf{B}} : \boldsymbol{\varepsilon}_r^* \tag{6.32}$$

Substitution of Eq. (6.31) into Eq. (6.25) renders the eigenstrain as

$$\boldsymbol{\varepsilon}_r^* = \left(\mathbf{I} + \overline{\mathbf{B}}\right)^{-1} : \left(\mathbf{I} - \overline{\mathbf{A}}_r\right) : \overline{\boldsymbol{\varepsilon}}_0 - \left(\mathbf{I} + \overline{\mathbf{B}}\right)^{-1} : \mathbf{C}_0^{-1} : \mathbf{C}_r : \overline{\boldsymbol{\varepsilon}}_r \tag{6.33}$$

Further, Eq. (6.31) gives,

$$\overline{\boldsymbol{\varepsilon}}_r = \mathbf{G}_r : \overline{\boldsymbol{\varepsilon}}_0 \tag{6.34}$$

where $\mathbf{G}_r$ is the local strain concentration tensor, defined as

$$\mathbf{G}_r = \left[\mathbf{I} + \overline{\mathbf{B}} : \left(\mathbf{I} - \mathbf{C}_0^{-1} : \mathbf{C}_r\right)\right]^{-1} : \left(\mathbf{I} - \overline{\mathbf{A}}_r\right) \tag{6.35}$$

As a consequence, the overall volume-averaged strain becomes

$$\overline{\boldsymbol{\varepsilon}} = \phi_0 \overline{\boldsymbol{\varepsilon}}_0 + \sum_{r=1}^{3} \phi_r \overline{\boldsymbol{\varepsilon}}_r = \mathbf{N}_r^{-1} : \overline{\boldsymbol{\varepsilon}}_r \tag{6.36}$$

where $\mathbf{N}_r$ is defined as the global strain concentration tensor for the *r*th phase fibers,

$$\mathbf{N}_r = \mathbf{G}_r : \left[\phi_0 \mathbf{I} + \sum_{r=1}^{3} \phi_r \mathbf{G}_r\right]^{-1} \tag{6.37}$$

Then, the overall volume-averaged stress can be shown as

$$\overline{\boldsymbol{\sigma}} = \phi_0 \overline{\boldsymbol{\sigma}}_0 + \sum_{r=1}^{3} \phi_r \overline{\boldsymbol{\sigma}}_r = \left[\mathbf{C}_0 + \sum_{r=1}^{3} \phi_r \left(\mathbf{C}_r - \mathbf{C}_0\right) : \mathbf{N}_r\right] : \overline{\boldsymbol{\varepsilon}} \tag{6.38}$$

Consequently, the effective stiffness tensor takes the form

$$\overline{\mathbf{C}} = \mathbf{C}_0 + \sum_{r=1}^{3} \phi_r \left(\mathbf{C}_r - \mathbf{C}_0\right) : \mathbf{N}_r \tag{6.39}$$

It is observed from Eq. (6.39) that the interface energy effect is incorporated in the effective stiffness tensor for the equivalented four-phase circular fiber reinforced nanocomposite. The classical Mori-Tanaka micromechanical solutions can be obtained directly from Eq. (6.39) when the interface energy effect can be neglected; i.e., $\mathbf{C}^{\mathrm{I}} = \mathbf{0}$ or *a* is in the micrometer or larger length scale.

6.4 Effective Elastoplastic Behavior

In this section, we consider the fiber reinforced nanocomposite with the elastoplastic matrix phase and the elastic reinforcement phases. The more general case that all the phases are elastoplastic can be formulated by adding the plastic strain to the eigenstrain in the reinforcement phases. Additionally, the composite under small strain is considered for simplicity due to the fact that more sophisticated interactions could occur at the large plastic strain in the matrix. During the plastic deformation, the local stress field varies from one point to another in the matrix and depends upon the loading history and the surrounding microstructure of the position in consideration. Therefore, the overall effective plastic behavior are studied.

To describe the overall effective plastic behavior of the composite, a volume-averaged von Mises yield criterion is constructed,

$$\bar{F}\left(\bar{\sigma}_0^*, \bar{\varepsilon}_0^{p*}\right) = \bar{\sigma}_0^* - K\left(\bar{\varepsilon}_0^{p*}\right) \tag{6.40}$$

where $\bar{\sigma}_0^*$ and $\bar{\varepsilon}_0^{p*}$ are the von Mises effective stress and effective plastic strain in the matrix, respectively, defined as

$$\bar{\sigma}_0^* = \sqrt{\frac{3}{2}\bar{\boldsymbol{\sigma}}_0 : \mathbf{I}^{dev} : \bar{\boldsymbol{\sigma}}_0} \quad \text{and} \quad \bar{\varepsilon}_0^{p*} = \sqrt{\frac{2}{3}\bar{\boldsymbol{\varepsilon}}_0^{p} : \bar{\boldsymbol{\varepsilon}}_0^{p}} \tag{6.41}$$

Here, $\bar{\boldsymbol{\sigma}}_0$ and $\bar{\boldsymbol{\varepsilon}}_0^{p}$ are the volume-averaged stress and plastic strain of the matrix, respectively. $K\left(\bar{\varepsilon}_0^{p*}\right)$ represent the isotropic hardening function of the matrix material. According to Eqs. (6.33) and (6.35),

$$\bar{\boldsymbol{\varepsilon}} = \left[\phi_0 \mathbf{I} + \sum_{r=1}^{3} \phi_r \mathbf{G}_r \right] : \bar{\boldsymbol{\varepsilon}}_0 \tag{6.42}$$

Further, from Eqs. (6.37) and (6.41), we arrive at

$$\bar{\boldsymbol{\sigma}} = \bar{\mathbf{C}} : \left[\phi_0 \mathbf{I} + \sum_{r=1}^{3} \phi_r \mathbf{G}_r \right] : \bar{\boldsymbol{\varepsilon}}_0 \tag{6.43}$$

and the relation between $\bar{\sigma}_0^*$ and $\bar{\sigma}$ are obtained

$$\bar{\boldsymbol{\sigma}}_0 = \mathbf{P} : \bar{\boldsymbol{\sigma}} \tag{6.44}$$

where

$$\mathbf{P} = \left[\bar{\mathbf{C}} : \left(\phi_0 \mathbf{I} + \sum_{r=1}^{3} \phi_r \mathbf{G}_r \right) : \mathbf{C}_0^{-1} \right]^{-1} \tag{6.45}$$

It is worthy to mention that when a traction $\mathbf{t} = \bar{\boldsymbol{\sigma}} \cdot \mathbf{n}$ is applied at the far field, $\bar{\boldsymbol{\sigma}}$ is identical to the overall volume-averaged stress of the composite. Substitution of Eq. (6.44) into Eq. (6.41) renders

$$\bar{\sigma}_0^* = \sqrt{\bar{\boldsymbol{\sigma}} : \mathbf{T} : \bar{\boldsymbol{\sigma}}} \tag{6.46}$$

where $\mathbf{T} = \frac{3}{2} \mathbf{P}^{\mathrm{T}} : \mathbf{I}^{\mathrm{dev}} : \mathbf{P}$. Further, Eq. (6.40) becomes

$$\bar{F}\left(\bar{\boldsymbol{\sigma}}, \bar{\varepsilon}_0^{p*} \right) = \sqrt{\bar{\boldsymbol{\sigma}} : \mathbf{T} : \bar{\boldsymbol{\sigma}}} - K\left(\bar{\varepsilon}_0^{p*} \right) \tag{6.47}$$

Eq. (6.47) is the effective yield function of the equivalented *four*-phase nanocomposite. Furthermore, we assume associative flow rule for the composite. However, the effective yield function with non-associative flow rule can be constructed in a similar manner by considering both of the normal and tangential directions of the plastic flow.

Since the associative flow rule is considered, the volume-averaged plastic increment can be characterized as

$$\dot{\bar{\boldsymbol{\varepsilon}}}^{p} = \dot{\gamma}\frac{\partial \bar{F}}{\partial \bar{\boldsymbol{\sigma}}} = \dot{\gamma}\frac{\mathbf{T}:\bar{\boldsymbol{\sigma}}}{\sqrt{\bar{\boldsymbol{\sigma}}:\mathbf{T}:\bar{\boldsymbol{\sigma}}}} \tag{6.48}$$

where $\dot{\bar{\boldsymbol{\varepsilon}}}^{p}$ is the overall volume-averaged plastic strain, and $\dot{\gamma}$ is the plastic consistency parameter. Here, the plastic loading/unloading conditions follow the Kuhn-Tucker condtions, that is

$$\dot{\gamma} \geq 0,\ F\left(\bar{\boldsymbol{\sigma}}, \bar{\varepsilon}_0^{p^*}\right) \leq 0,\ \dot{\gamma}F\left(\bar{\boldsymbol{\sigma}}, \bar{\varepsilon}_0^{p^*}\right) = 0 \tag{6.49}$$

As the plastic strain occurs in the matrix domain, the overall volume averaged plastic increment can be demonstrated as

$$\dot{\bar{\boldsymbol{\varepsilon}}}^{p} = \phi_0 \dot{\bar{\boldsymbol{\varepsilon}}}_0^{p} \tag{6.50}$$

Therefore, the volume-averaged plastic strain increment of the matrix is obtained as

$$\dot{\bar{\boldsymbol{\varepsilon}}}_0^{p} = \dot{\gamma}\frac{\mathbf{T}:\bar{\boldsymbol{\sigma}}}{\phi_0\sqrt{\bar{\boldsymbol{\sigma}}:\mathbf{T}:\bar{\boldsymbol{\sigma}}}} \tag{6.51}$$

and the equivalent plastic increment of the matrix is determined by

$$\dot{\bar{\varepsilon}}_0^{p^*} = \sqrt{\frac{2}{3}\dot{\bar{\boldsymbol{\varepsilon}}}_0^{p}:\dot{\bar{\boldsymbol{\varepsilon}}}_0^{p}} \tag{6.52}$$

In summary, from Eqs. (6.51)–(6.52), $\dot{\bar{\boldsymbol{\varepsilon}}}_0^{p^*}$ can be expressed as the function of $\dot{\gamma}$ for a given $\bar{\boldsymbol{\sigma}}$. Substitution of $\dot{\bar{\boldsymbol{\varepsilon}}}_0^{p^*}$ into Eq. (6.47) leads to an equation of $\dot{\gamma}$, from which $\dot{\gamma}$ can be solved and the plasrtic increment is determined. Therefore, provided the hardening function $K\left(\bar{\varepsilon}_0^{p^*}\right)$ of the

matrix, the overall effective plastic behavior of the composite can be fully characterized by Eqs. (6.47), (6.51) and (6.52).

6.5 Overall Elastoplastic Damage Responses under Biaxial Tensile Loading

In this section, the elastoplastic damage responses of the fiber-reinforced nanocomposite are presented under the proposed framework. For simplicity, we assume the transverse biaxial tensile loading is applied to the composite at far-field, and the plane strain condition is followed. The applied tensile stress can be written as

$$\bar{\sigma}_{11} > 0,\ \bar{\sigma}_{22} = R\bar{\sigma}_{11} \tag{6.53}$$

where R is the ratio between the biaxial stresses. In addition, to satisfy the plane strain condition,

$$\bar{\sigma}_{33} = \eta_1\bar{\sigma}_{11} + \eta_2\bar{\sigma}_{22} \ \text{ and all other } \ \bar{\sigma}_{ij} = 0 \tag{6.54}$$

where

$$\eta_1 = \frac{\bar{C}_{1133}\bar{C}_{2222} - \bar{C}_{1122}\bar{C}_{2233}}{\bar{C}_{1111}\bar{C}_{2222} - \bar{C}_{1122}^2},\ \eta_2 = \frac{\bar{C}_{1111}\bar{C}_{2233} - \bar{C}_{1122}\bar{C}_{1133}}{\bar{C}_{1111}\bar{C}_{2222} - \bar{C}_{1122}^2} \tag{6.55}$$

Furthermore, the power-law type hardening function is employed, and the effective yield function in Eq. (6.47) becomes

$$\bar{F}\left(\bar{\sigma}_{11}, \bar{\varepsilon}_0^{p*}\right) = \Phi(R)\left|\bar{\sigma}_{11}\right| - \sqrt{\frac{2}{3}}\left[\sigma_y + h\left(\bar{\varepsilon}_0^{p*}\right)^q\right] \tag{6.56}$$

where σ_y is the initial yield stress of the matrix, h, q are the constants associated with the plastic hardening behavior of the matrix material, and

$$\Phi(R) = \sqrt{T_{1111} + R\left(T_{1122} + T_{2211}\right) + \left(\eta_1 + R\eta_2\right)\left(T_{1133} + T_{3311}\right) + \left(\eta_1 + R\eta_2\right)^2 T_{3333}} \tag{6.57}$$

Additionally, the volume-averaged plastic strain increment of the composite and the equivalent plastic strain increment of the matrix can be expressed as

$$\Delta\bar{\boldsymbol{\varepsilon}}^{p}=\frac{\Delta\gamma}{\Phi(R)}\begin{bmatrix} T_{1111}+RT_{1122}+(\eta_1+R\eta_2)T_{1133} & 0 \\ 0 & T_{2211}+RT_{2222}+(\eta_1+R\eta_2)T_{2233} \end{bmatrix} \tag{6.58}$$

$$\Delta\bar{\varepsilon}_0^{p^*}=\frac{\Delta\gamma}{\phi_0\Phi(R)}\Theta(R) \tag{6.59}$$

where

$$\Theta(R)=\sqrt{\frac{2}{3}\left\{\left[T_{1111}+RT_{1122}+(\eta_1+R\eta_2)T_{1133}\right]^2+\left[T_{2211}+RT_{2222}+(\eta_1+R\eta_2)T_{2233}\right]^2\right\}} \tag{6.60}$$

The corresponding elastic strain increment of the composite is

$$\Delta\bar{\boldsymbol{\varepsilon}}^{e}=\begin{bmatrix} \bar{D}_{1111}+R\bar{D}_{1122}+(\eta_1+R\eta_2)\bar{D}_{1133} & 0 \\ 0 & \bar{D}_{2211}+R\bar{D}_{2222}+(\eta_1+R\eta_2)\bar{D}_{2233} \end{bmatrix}\Delta\bar{\sigma}_{11} \tag{6.61}$$

where $\left[\bar{D}_{ijkl}\right]=\left[\bar{C}_{ijkl}\right]^{-1}$ is the effective compliance tensor of the composite. As a consequence, the total strain increment in the composite reveals to be

$$\begin{aligned}\Delta\bar{\boldsymbol{\varepsilon}}=&\begin{bmatrix} \bar{D}_{1111}+R\bar{D}_{1122}+(\eta_1+R\eta_2)\bar{D}_{1133} & 0 \\ 0 & \bar{D}_{2211}+R\bar{D}_{2222}+(\eta_1+R\eta_2)\bar{D}_{2233} \end{bmatrix}\Delta\bar{\sigma}_{11}\\ &+\frac{\Delta\gamma}{\Phi(R)}\begin{bmatrix} T_{1111}+RT_{1122}+(\eta_1+R\eta_2)T_{1133} & 0 \\ 0 & T_{2211}+RT_{2222}+(\eta_1+R\eta_2)T_{2233} \end{bmatrix}\end{aligned} \tag{6.62}$$

According to the Kuhn-Tucker conditions, $\Delta\gamma>0$ and $\bar{F}\left(\bar{\sigma}_{11},\bar{\varepsilon}_0^{p^*}\right)=0$ during the plastic loading process, which renders

$$\Phi(R)\left(\bar{\sigma}_{11}\right)_{n+1}=\sqrt{\frac{2}{3}}\left[\sigma_y+h\left(\left(\bar{\varepsilon}_0^{p*}\right)_n+\frac{\Theta(R)}{\Phi(R)}\Delta\gamma\right)^q\right] \tag{6.63}$$

where $\Delta\gamma$ can be solvd as

$$\Delta\gamma=\left[\left(\frac{\sqrt{\frac{3}{2}}\Phi(R)\left(\bar{\sigma}_{11}\right)_{n+1}-\sigma_y}{h}\right)^{1/q}-\left(\bar{\varepsilon}_0^{p*}\right)_n\right]\frac{\Phi(R)}{\Theta(R)} \tag{6.64}$$

6.6 Numerical Simulations and Discussions

In this section, numerical simulations are demonstrated to illustrate the predictions of the present model. The results under the proposed model are compared with the classical micromechanical solutions, in which the interface energy effect is neglected. However, due to the lack of available experimental data, experimental validation is not implemented. The experimental validation will be performed in the future once suitable experiment data become availivable.

Let us consider a *two*-phase continuous circular fiber reinforced nanocomposite. We assume that the nanocomposite consists the Ti-6Al-4V matrix (K_0 = 94.8 GPa, μ_0 = 43.7 GPa) and randomly distributed continuous SiC fibers (K_1 = 345 GPa, μ_1 = 159.2 GPa) (Nimmer et al., 1991). Further, the plastic parameters of the matrix material are $\sigma_y=500\text{MPa}$, $h=700\text{MPa}$ and $q=0.1$ (Ju and Lee, 2000, 2001), and the parameters of the Weibull's distribution function are $S_0=180\text{MPa}$, $M=3$, and $\sigma_{\text{cri}}=170\text{MPa}$ (Ju and Ko, 2008). In term of the interface properties, we choose two sets of interface moduli, which are $K_1^{\text{I}}=100$ N/m, $\mu_1^{\text{I}}=50$ N/m for the perfectly bonded interface and $K_3^{\text{I}}=-50$ N/m, $\mu_3^{\text{I}}=-25$ N/m for the free surface. Note that the interface

moduli are related to the microstructures at the interface. The aforementioned sets of interface moduli are chosen for illustration purpose, and the actual interface moduli for the current nanocomposite can be obtained by different methods such as the molecular dynamics simulation (Miller and Shenoy, 2000), first principles and atomistic potential calculations.

The stress-strain relation of the nanocomposite under the transverse tensile biaxial loading (R = 0.4) is displayed in Fig. 6–3. Comparisons are made between the solutions with and without considering the interface energy effect; i.e., the nanomechanical solution and the micromechanical solution. Both solutions present two 'knees' on the figure. The first 'knee' corresponds to the evolution of the interface debonding. Due to the progressive debonding of the interface and the evolution of the corresponding volume fractions, the slope of the curve decrease gradually. Before the first 'knee', all the fibers are in phase 1, which are the perfectly bonded fibers. During the first 'knee', interface debonding inititates in the composite, and all the bonding phases may exist at the same time. At the end of the first 'knee', we consider that all the fibers are completely debonded and the composite can be treated as the matrix with nanovoids in the transverse directions. Therefore, the decreasing of the slope is suspended. At a higher stress level, the matrix yields and the plastic deformation appears in the matrix, which forms the second 'knee' on the figure. Moreover, the interface energy effect is noticed on the stress-strain curve. Based on the currently adopted interface elastic moduli of the bonded interface and the free surface, the interface energy shows consistent effect on the stiffness of the composite during the elastoplastic damage process. Before the first 'knee', the interface energy effect is goverened by the interface elastic moduli of

the prefectly bonded interface. In the region of the first 'knee', the interface elastic moduli transites from K_1^{I}, μ_1^{I} to K_3^{I}, μ_3^{I}. After the first 'knee', the interface elastic moduli are constant.

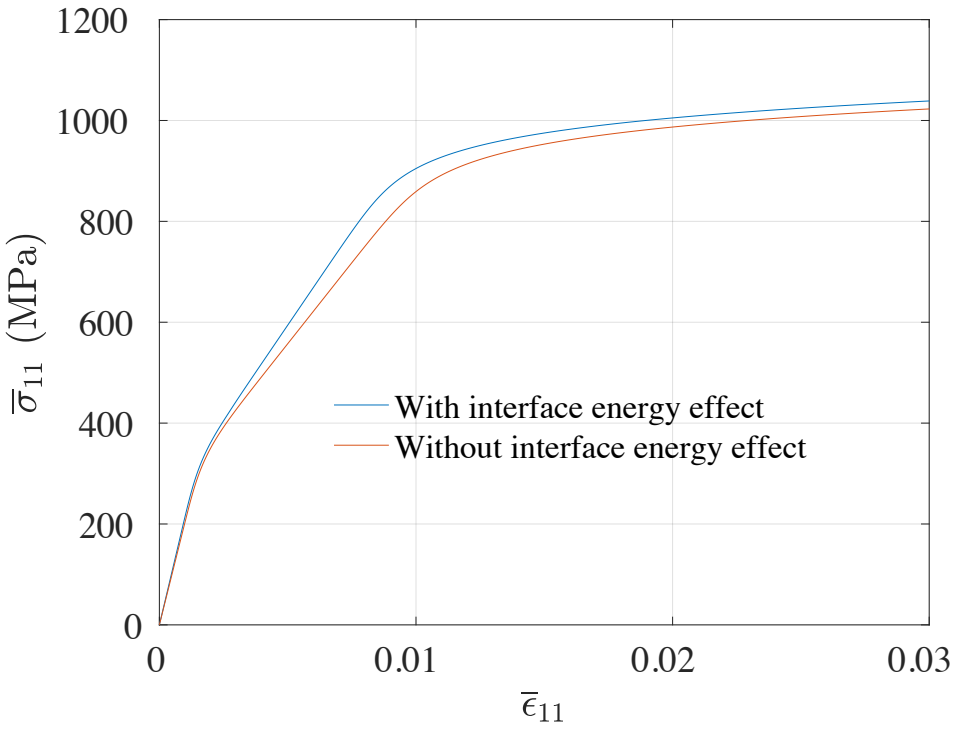

Figure 6–3 The comparison between the nanomechanical prediction and the micromechanical prediction.

The effect of interface energy on the evolution of the debonding angle and the volume fractions are presented in Fig. 6–4 and Fig. 6–5, respectively. When the interface energy effect is considered, the debonding initiates at a lower strain due to the higher initial stiffness. The change of the debonding angles with respect to the strain $\overline{\varepsilon}_{11}$ are also displayed in Fig. 6–4, and the debonding angle reaches $\pi/2$ at the end, which corresponds to the complete debonding. The change

of the volume fractions of the equivalented reinforcement phases are exhibited in Fig. 6–5. The volume fraction of phase 1 fibers decraeses gradually with the increase of the external loading. However, when the debonding angle reaches π/2, the phase 2 partially debonded fibers become completely debonded fibers, which corresponds to the abrupt changes on the figure. It is also noticed that different bonding phases can exist in the composite at the same time.

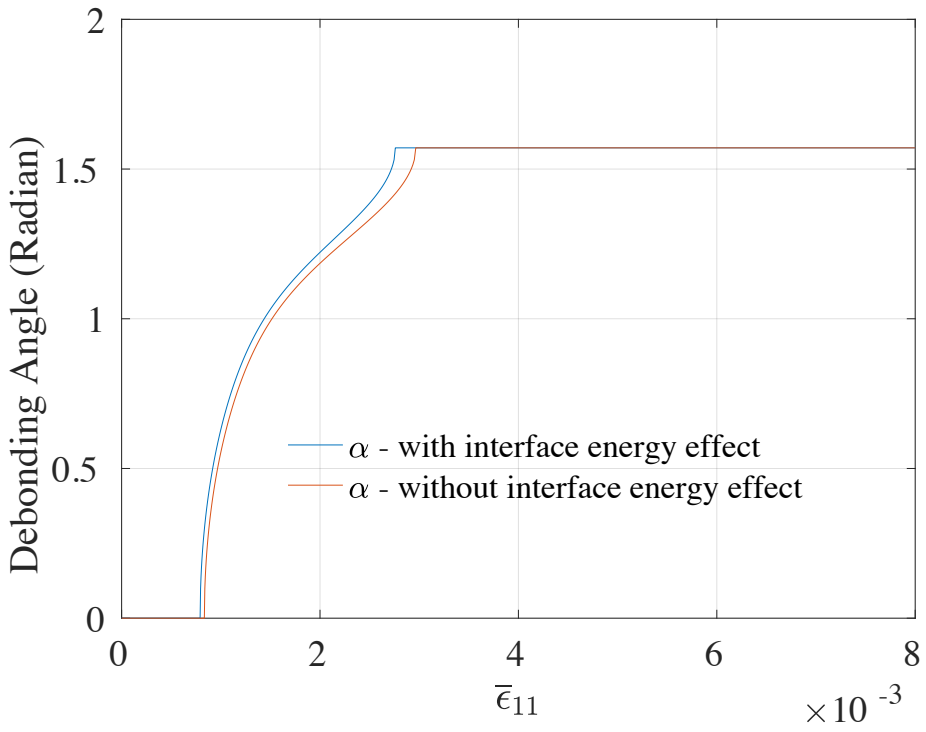

Figure 6–4 Debonding angle α vs. $\bar{\varepsilon}_{11}$.

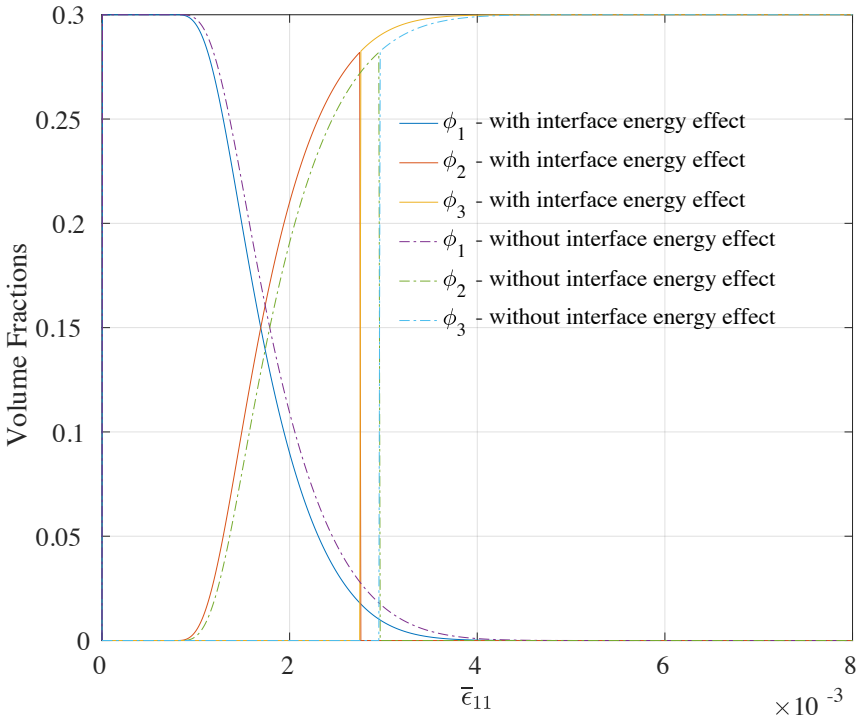

Figure 6–5 The evolution of volume fractions vs. $\overline{\varepsilon}_{11}$.

In Fig. 6–6, comparisons are made for the nanocomposites with different radius of the circular fibers. Larger interface energy effect is noticed for composites with smaller fibers. As the radius increases, the interface energy effect decreases, and the nanomechanical prediction approach to the micromechanical solution.

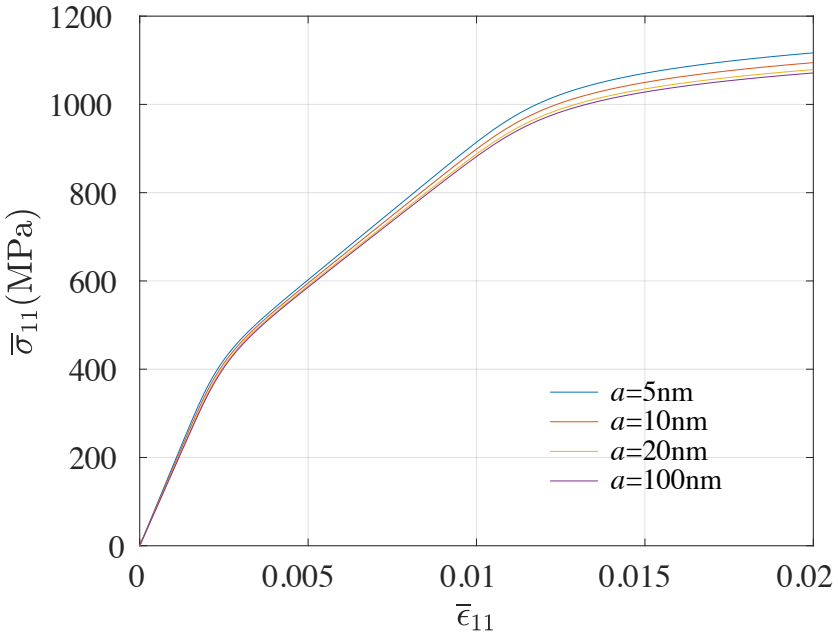

Figure 6–6 The size effect on the stress-strain relation of the composites reinforced by the circular fibers with different radius.

The nanomechanical predictions on the nanocomposites having different reinforcement volume fractions are displayed in Fig. 6-7. Since the reinforcements are stronger than the matrix, the composite with higher volume fraction presents higher initial elastic stiffness (before the debonding initiates). However, after the debonding initiates, the load transferring ability gradually decreases in the transverse directions, and the effective stiffness of the composite with higher volume fraction tends to decrease faster. When the interfaces are completely debonded, higher volume fraction leads to lower effective stiffness.

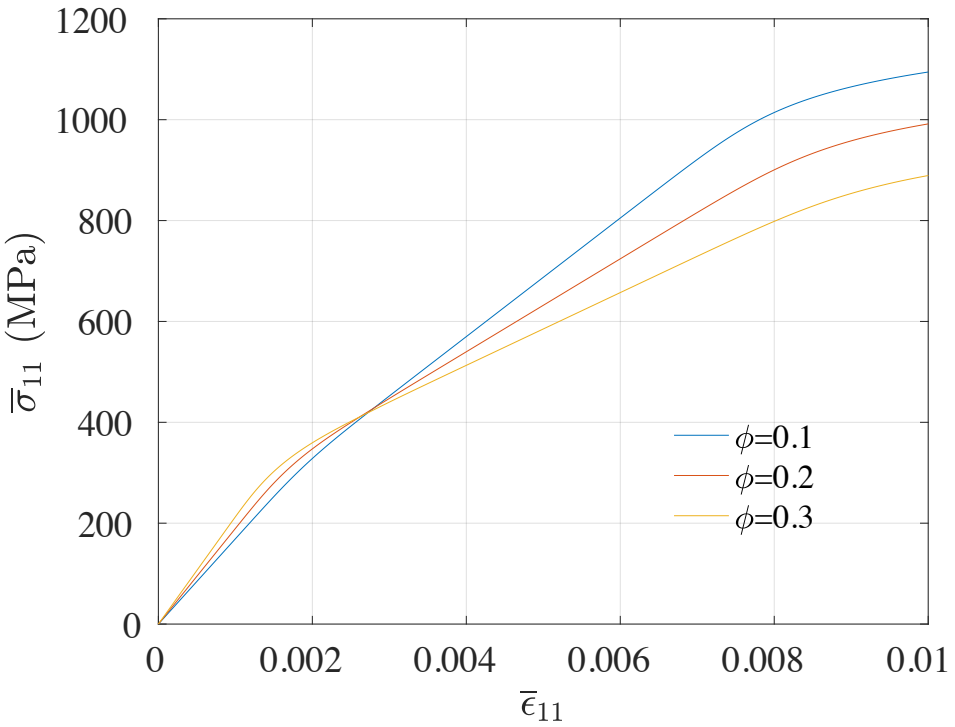

Figure 6–7 The comparison among composites with different volume fractions of the fibers

6.7 Conclusions

The interface energy effect on the effective elastoplastic behavior is studied for the continuous fiber reinforced nanocomposite with interface debonding. The debonding initiates when the tensile normal traction reaches the critical debonding stress at the interfce. The debonding angle that describes the extent of the debonded region can be solved according to the stress at the interface. Based on the debonding angle, the damage parameters are defined along two perpendicular directions that corresponds to the principle stresses in the transverse directions. Since the stress field around each fiber differs, we adopt the Weibull's distribution function to predict the

possibilities of the interface debonding. Therefore, the three bonding conditions (perfect bonding, partial debonding, complete debonding) can exist at the same time. Further, the debonded fibers are equivalented into the perfectly bonded fibers with reduced elastic stiffness. As a consequence, the original *two*-phase composite is equivalented into a *four*-phase compoiste.

The interface energy effect is considered on the equivalented composite. The effect of interface energy is simulated by a zero-thickness membrane interphase between the matrix and the fiber, and the interface stress is intorduced in the membrane interphase, which leads to the discontinuous stress through the matrix-fiber interface. The change of the interface energy effect during the debonding evolution is considered by adopting the gradually changing interface elastic moduli for the equivalented fibers. Following the Mori and Tanaka's assumption on the effective matrix and solving the interfacial stress discontinity equations, the elastic stiffness tensor of the equivalented *four*-phase composite is determined.

To predict the plastic behavior, we assume that the matrix is elastoplastic, while the fibers are elastic. An effective yield function of the composite is proposed in Section 6.4, in which the associative flow rule and the isotropic hardening law are adopted. The yield function, the elastic strain incremental and the plastic strain incremental are presented for the composite under the biaxial tensile transverse loading in Section 6.5.

Numerical simulations are presented in Section 6.6 for the composite under bixial tensile transverse loading. The progressive interface debonding and the evolution of the volume fractions are demonstrated. Comparisons are made between the nanomechanical and the micromechanical

predictions of the growth of the debonding angle, the development of the volume fractions and the stress-strain curve. The dependence of the effect of interface energy upon the size and the volume fractions of the fibers is also investigated. The results reveal that when the interface energy effect is considered, the mechanical behaivors of the composite exhibit size dependence and are related to the total interface area. The effect of interface energy increases with the increasing of the total interface area, and become negligible when the size of reinforcements in the composite are in micrometer scale. However, due to the lack of available experimental data, experimental validations are not performed in the present chapter. Comparisons between the current prediction and the experimental data are warranted once suitable and reliable experimental data become available in the future.

6.8 References

Aboudi, J. (1987). Damage in composites—modeling of imperfect bonding. *Composites Science and Technology*, *28*(2), 103-128.

Bottomley, D. J., & Ogino, T. (2001). Alternative to the Shuttleworth formulation of solid surface stress. Physical Review B, 63(16), 165412.

Budiansky, B. (1965). On the elastic moduli of some heterogeneous materials. Journal of the Mechanics and Physics of Solids, 13(4), 223-227.

Cammarata, R. C. (1997). Surface and interface stress effects on interfacial and nanostructured materials. Materials Science and Engineering: A, 237(2), 180-184.

Deng, S., Ye, L., & Friedrich, K. (2007). Fracture behaviours of epoxy nanocomposites with nano-silica at low and elevated temperatures. Journal of materials science, 42(8), 2766-2774.

Duan, H. L., Wang, J. X., Huang, Z. P., & Karihaloo, B. L. (2005a). Size-dependent effective elastic constants of solids containing nano-inhomogeneities with interface stress. Journal of the Mechanics and Physics of Solids, 53(7), 1574-1596.

Duan, H. L., Wang, J., Huang, Z. P., & Karihaloo, B. L. (2005b). Eshelby formalism for nano-inhomogeneities. Proceedings of the Royal Society A: Mathematical, Physical and Engineering Sciences, 461(2062), 3335-3353.

Duan, H. L., Wang, J., Huang, Z. P., & Luo, Z. Y. (2005c). Stress concentration tensors of inhomogeneities with interface effects. Mechanics of Materials, 37(7), 723-736.

Eshelby, J. D. (1957). The determination of the elastic field of an ellipsoidal inclusion, and related problems. Proceedings of the Royal Society of London. Series A. Mathematical and Physical Sciences, 241(1226), 376-396.

Eshelby, J. D. (1959). The elastic field outside an ellipsoidal inclusion. Proceedings of the Royal Society of London. Series A. Mathematical and Physical Sciences, 252(1271), 561-569.

Ferkel, H., & Mordike, B. L. (2001). Magnesium strengthened by SiC nanoparticles. Materials Science and Engineering: A, 298(1-2), 193-199.

Gibbs, J. W. (1906). The scientific papers of J. Willard Gibbs(Vol. 1). Longmans, Green and Company.

Gurtin, M. E., & Murdoch, A. I. (1975). A continuum theory of elastic material surfaces. Archive for Rational Mechanics and Analysis, 57(4), 291-323.

Hashin, Z., & Shtrikman, S. (1963). A variational approach to the theory of the elastic behaviour of multiphase materials. Journal of the Mechanics and Physics of Solids, 11(2), 127-140.

Hill, R. (1965). A self-consistent mechanics of composite materials. Journal of the Mechanics and Physics of Solids, 13(4), 213-222.

Ju, J. W. (1989a). On energy-based coupled elastoplastic damage theories: constitutive modeling and computational aspects. International Journal of Solids and structures, 25(7), 803-833.

Ju, J. W. (1989b). Energy-based coupled elastoplastic damage models at finite strains. Journal of Engineering Mechanics, 115(11), 2507-2525.

Ju, J. W., & Chen, T. M. (1994a). Micromechanics and effective moduli of elastic composites containing randomly dispersed ellipsoidal inhomogeneities. Acta Mechanica, 103(1-4), 103-121.

Ju, J. W., & Chen, T. M. (1994b). Effective elastic moduli of two-phase composites containing randomly dispersed spherical inhomogeneities. Acta Mechanica, 103(1-4), 123-144.

Ju, J. W., & Chen, T. M. (1994). Micromechanics and effective elastoplastic behavior of two-phase metal matrix composites.

Ju, J. W., & Lee, H. K. (2000). A micromechanical damage model for effective elastoplastic behavior of ductile matrix composites considering evolutionary complete particle debonding. Computer Methods in Applied Mechanics and Engineering, 183(3-4), 201-222.

Ju, J. W., & Lee, H. K. (2001). A micromechanical damage model for effective elastoplastic behavior of partially debonded ductile matrix composites. International Journal of Solids and Structures, 38(36-37), 6307-6332.

Ju, J. W., & Ko, Y. F. (2008). Micromechanical elastoplastic damage modeling of progressive interfacial arc debonding for fiber reinforced composites. International Journal of Damage Mechanics, 17(4), 307-356.

Ju, J. W., Ko, Y. F., & Ruan, H. N. (2006). Effective elastoplastic damage mechanics for fiber-reinforced composites with evolutionary complete fiber debonding. International Journal of Damage Mechanics, 15(3), 237-265.

Ju, J. W., Ko, Y. F., & Ruan, H. N. (2008). Effective elastoplastic damage mechanics for fiber reinforced composites with evolutionary partial fiber debonding. International Journal of Damage Mechanics, 17(6), 493-537.

Ju, J. W., Ko, Y. F., & Zhang, X. D. (2009). Multi-level elastoplastic damage mechanics for elliptical fiber-reinforced composites with evolutionary fiber debonding. International Journal of Damage Mechanics, 18(5), 419-460.

Ju, J. W., & Yanase, K. (2009). Micromechanical elastoplastic damage mechanics for elliptical fiber-reinforced composites with progressive partial fiber debonding. International Journal of Damage Mechanics, 18(7), 639-668.

Ju, J. W., & Yanase, K. (2008). Elastoplastic damage micromechanics for elliptical fiber composites with progressive partial fiber debonding and thermal residual stresses. Theor. Appl. Mech, 35(1-3), 137-170.

Ko, Yu-Fu. (2005), "Effective elastoplastic-damage model for fiber-reinforced metal matrix composites with evolutionary fibers debonding", Ph.D. Thesis, University of California, Los Angeles, CA.

Lee, H.K., and Ju, J.W. (2007). "A three-dimensional stress analysis of a pennyshaped crack interacting with a spherical inclusion", Int. J. of Damage Meek, 16: 331-359.

Liu, H. T., Sun, L. Z., & Ju, J. W. (2004). An interfacial debonding model for particle-reinforced composites. International Journal of Damage Mechanics, 13(2), 163-185.

Liu, H. T., Sun, L. Z., & Ju, J. W. (2006). Elastoplastic modeling of progressive interfacial debonding for particle-reinforced metal-matrix composites. Acta Mechanica, 181(1-2), 1-17.

Matouš, K. (2003). Damage evolution in particulate composite materials. International Journal of Solids and Structures, 40(6), 1489-1503.

Miller, R. E., & Shenoy, V. B. (2000). Size-dependent elastic properties of nanosized structural elements. Nanotechnology, 11(3), 139.

Mori, T., & Tanaka, K. (1973). Average stress in matrix and average elastic energy of materials with misfitting inclusions. Acta metallurgica, 21(5), 571-574.

Nimmer, R. P., Bankert, R. J., Russell, E. S., Smith, G. A., & Wright, P. K. (1991). Micromechanical modeling of fiber/matrix interface effects in transversely loaded SiC/Ti-6-4 metal matrix composites. Journal of Composites, Technology and Research, 13(1), 3-13.

Pagano, N. J., & Tandon, G. P. (1990). Modeling of imperfect bonding in fiber reinforced brittle matrix composites. Mechanics of Materials, 9(1), 49-64.

Paulino, G. H., Yin, H. M., & Sun, L. Z. (2006). Micromechanics-based interfacial debonding model for damage of functionally graded materials with particle interactions. International Journal of Damage Mechanics, 15(3), 267-288.

Rinaldi, A., Krajcinovic, D., & Mastilovic, S. (2007). Statistical damage mechanics and extreme value theory. International Journal of Damage Mechanics, 16(1), 57-76.

Sharma, P., & Ganti, S. (2004). Size-dependent Eshelby's tensor for embedded nano-inclusions incorporating surface/interface energies. J. Appl. Mech., 71(5), 663-671.

Sharma, P., Ganti, S., & Bhate, N. (2003). Effect of surfaces on the size-dependent elastic state of nano-inhomogeneities. Applied Physics Letters, 82(4), 535-537.

Shehata, F. A. R. O. U. K., Fathy, A., Abdelhameed, M., & Moustafa, S. F. (2009). Preparation and properties of Al2O3 nanoparticle reinforced copper matrix composites by in situ processing. Materials & Design, 30(7), 2756-2762.

Simo, J. C., & Ju, J. W. (1987a). Strain-and stress-based continuum damage models—I. Formulation. International journal of solids and structures, 23(7), 821-840.

Simo, J. C., & Ju, J. W. (1987b). Strain-and stress-based continuum damage models—II. Computational aspects. International journal of solids and structures, 23(7), 841-869.

Sun, L. Z., Ju, J. W., & Liu, H. T. (2003). Elastoplastic modeling of metal matrix composites with evolutionary particle debonding. Mechanics of Materials, 35(3-6), 559-569.

Tandon, G. P., & Weng, G. J. (1984). The effect of aspect ratio of inclusions on the elastic properties of unidirectionally aligned composites. Polymer composites, 5(4), 327-333.

Trojanová, Z., Lukáč, P., Ferkel, H., & Riehemann, W. (2004). Internal friction in microcrystalline and nanocrystalline Mg. Materials Science and Engineering: A, 370(1-2), 154-157.

Voyiadjis, G. Z., Kattan, P. I., & Taqieddin, Z. N. (2007). Continuum approach to damage mechanics of composite materials with fabric tensors. International Journal of Damage Mechanics, 16(3), 301-329.

Zhao, Y. H., & Weng, G. J. (1997). Transversely isotropic moduli of two partially debonded composites. International Journal of Solids and Structures, 34(4), 493-507.

Zhao, Y. H., & Weng, G. J. (2002). The effect of debonding angle on the reduction of effective moduli of particle and fiber-reinforced composites. J. Appl. Mech., 69(3), 292-302.

- Chapter 7 -

SUMMARY AND FUTURE WORK

7.1 Summary

In this research, the overall effective mechanical behavior of particle reinforced and continuous fiber reinforced nanocomposites are investigated by considering the interface energy effect.

In Chapter 3, the interface energy effect on the spherical particle reinforced nanocomposite is investigated. To account for the interface energy effect, the interface is simulated by the zero-thickness membrane interphase, which leads to the stress and strain discontinuities between the matrix and the particles. By solving the equilibrium equations of the idealized interphase, the effective elastic fields in the matrix and the particles are related and isotropic interface energy effect is noticed on the effective fields. Furthermore, the effective elastic moduli of the spherical fiber reinforced nanocomposite are derived based on the homogenization procedures of the direct Eshelby method and the Mori-Tanaka method. It is recognized that the effective moduli, which considers the interface energy effect, exhibit the dependence upon the particle sizes and the particulate volume fractions. In addition, the illustrative figures, which are developed based on the analytical expressions, depict that the interface energy effect decreases with the increasing of the

particle size and the volume fractions. Moreover, when the size of the particles is in micrometer or larger scale, the interface energy effect becomes negligible, and the predictions are equal to the corresponding classical micromechanics solutions.

Based on the formulation in Chapter 3, a nanomechanical framework is developed in Chapter 4 to predict the effective elastic moduli of the spheroidal particle reinforced nanocomposites. Compared with Chapter 3, the framework is able to address the more sophisticated particle shapes, which range from spherical particles to the continuous fibers. The interface energy effect is averaged over the interface area, and the anisotropic effect is noticed on the effective elastic fields. Following the Mori-Tanaka method, the effective moduli are determined for the spheroidal particle reinforced nanocomposite. Further, the particle size dependence and the particulate volume fraction dependence are observed on the effective moduli.

In Chapter 5, a nanomechanical framework is formulated to predict the effective elastoplastic behavior of the spherical particle reinforced metal matrix nanocomposites. The matrix is assumed to be elastoplastic and the particles are elastic. The decreasing constraint power of the matrix during the plastic deformation is considered by adopting the secant moduli of the matrix under the Mori-Tanaka mean-field theory. Additionally, the effective secant moduli are obtained for the metal matrix nanocomposite.

Chapter 6 is devoted to predicting the overall effective elastoplastic behavior of the continuous fiber reinforced two-phase nanocomposites under interface debonding. Similar to Chapter 5, the matrix is assumed to be elastoplastic and the fibers are elastic. The interface debonding initiates

when the normal traction at the interface reaches the critical debonding stress. Progressive debonding is considered, the extent of debonding is related to the stress state at the interface. Moreover, the damage volume fraction evolution is accounted by the Weibull's distribution function. The fibers with different bonding conditions can exit in the matrix at the same time. Further, the isotropic debonded fibers are equivalented into perfectly bonded orthotropic fibers, and the two-phase composite with interface debonding is equivalented into a four-phase composite without interface debonding. Based on the equivalented composite, the elastic moduli are determined following the Mori-Tanaka mean-field theory, and an effective yield function of the composite is proposed to predict the plastic behavior.

7.2 Future Work

The main objective of the present research is to develop the simple and analytical nanomechanical frameworks for the nanocomposites, where the effect of interface energy is considered. Unlike the perfect interface conditions in the micromechanical formulations, the stress and strain are discontinuous through the interface, and the discontinuities are shown in the *generalized* Young-Laplace equations. Solving the *generalized* Young-Laplace equations renders the direct relation of the strain in the matrix and the strain in the reinforcement at the interface. Although the *generalized* Young-Laplace equations can be solved exactly at the interface, it is very difficult to determine the point-wise stress and strain fields in the reinforcements. Therefore, the effective medium approaches are employed, and the effective elastic fields are considered for the

matrix and the reinforcements. It is well known that the micromechanical effective medium approaches neglect the near-field interactions and are only applicable for the composites with low to moderate volume fractions of the reinforcement phases; e.g., the volume fraction at approximately 0.1 for the direct Eshelby method and 0.2 for the Mori-Tanaka method. The direct particle interaction model with the higher order pair-wise particle interaction solution present much better predictions on the elastic moduli of the spherical particle reinforced composites with higher reinforcement volume fractions. If the nanocomposites with moderate to moderate high particle concentrations are under consideration, the direct particle interaction model can be adopted in the determination of the elastic properties. However, the calculation cost is significantly increased. Moreover, the pair-wise solution is presented for spherical particles only. For the ellipsoidal/spheroidal particles, the pair-wise solution can be more difficult to be obtained. As a consequence, the present study employs the Mori-Tanaka mean-field theory to investigate the mechanical properties of the nanocomposites with moderate reinforcement concentrations, and future work can be done to apply the direct particle interaction model to consider the interface energy effect.

The prolate spheroidal particles in Chapter 4 are assumed to be unidirectionally aligned for simplicity. At two limiting conditions, the unidirectionally aligned prolate spheroids become the spheres or the unidirectionally aligned long fibers. However, the composites with randomly oriented particles attract more attention currently. Therefore, an orientation average procedure can be performed on the framework in Chapter 4 to consider the randomly oriented particles. Further,

the research on the spheroidal particles can be extended to the ellipsoidal particles. Although the *generalized* Young-Laplace are more complicated for ellipsoids, the framework for the composites with ellipsoidal particles can be applied in a more general condition.

The elastic moduli of the idealized interphase are assumed to be constant during the plastic deformation in the matrix. However, the local atomic environment at the interface changes with the development of the plastic strain in the matrix, which may lead to the non-negligible change in the interface properties. Therefore, the change of the interface properties with the increasing of the plastic strain can be studied. Further, the interface is considered as linear isotropic for the partially debonded fibers, which are equivalented into perfectly bonded fibers with reduced stiffness in Chapter 6. Since the bonded interface and the free surface have distinct interface properties, future work is needed to validate the proposed estimation on the interface elastic moduli for the partially debonded interface, which combines the bonded interface and the free surface. Additionally, it is recognized that the local interfacial shear stress could affect the interface debonding process. An energy-based interface debonding criterion can be introduced to accommodate the effect of the local radial normal and shear stresses on the interface debonding.

Experimental validations are the key parameters in the calibration of the proposed frameworks. However, due to the difficulty in the production, nanocomposites are not widely used in the industry, and the experiments on the investigation of the mechanical properties of the nanocomposites are very limited. Further experimental validations will be performed once the suitable and reliable experiment data become available.

Last but not least, the present frameworks are able to be applied in the customized optimal design of the nanocomposites, which allow us to select different constituent phases, interface properties, volume fractions and particle sizes to achieve optimal properties. Additionally, extensions of the current mechanical frameworks to consider other physical problems, such as the problems on the electrical and thermal conductivity, magnetism, electromagnetism and other couple-field and multi-field problems, can be done in the future.

Appendix I. Interfacial Strain Discontinuity Tensor of Spherical Particle Reinforced Composites

Since the *generalized* Young-Laplace equations for spherical particles are expressed under the spherical coordinate system, we start by transforming the effective strain tensor in the matrix under the Cartesian coordinate system to the spherical coordinate system,

$$\left(\hat{\boldsymbol{\varepsilon}}^0\right)^{spherical} = \mathbf{L}\hat{\boldsymbol{\varepsilon}}^0\mathbf{L}^{\mathrm{T}} \tag{I.1}$$

where $\mathbf{L}$ is the transformation matrix

$$\mathbf{L} = \begin{bmatrix} \sin\theta\cos\phi & \sin\theta\sin\phi & \cos\theta \\ \cos\theta\cos\phi & \cos\theta\sin\phi & -\sin\theta \\ -\sin\phi & \cos\phi & 0 \end{bmatrix} \tag{I.2}$$

The tangential components of $\left(\hat{\boldsymbol{\varepsilon}}^0\right)^{spherical}$ can be presented as

$$\begin{aligned} \hat{\varepsilon}^0_{\theta\theta} = {} & (\cos^2\theta\cos^2\phi)\hat{\varepsilon}^0_{xx} + (\cos^2\theta\sin^2\phi)\hat{\varepsilon}^0_{yy} + (\sin^2\theta)\hat{\varepsilon}^0_{zz} \\ & + (\cos^2\theta\sin 2\phi)\hat{\varepsilon}^0_{xy} + (-\sin 2\theta\cos\phi)\hat{\varepsilon}^0_{xz} + (-\sin 2\theta\sin\phi)\hat{\varepsilon}^0_{yz} \end{aligned} \tag{I.3}$$

$$\hat{\varepsilon}^0_{\phi\phi} = (\sin^2\phi)\hat{\varepsilon}^0_{xx} + (\cos^2\phi)\hat{\varepsilon}^0_{yy} + (-\sin 2\phi)\hat{\varepsilon}^0_{xy} \tag{I.4}$$

$$\begin{aligned} \hat{\varepsilon}^0_{\theta\phi} = {} & (-\frac{1}{2}\cos\theta\sin 2\phi)\hat{\varepsilon}^0_{xx} + (\frac{1}{2}\cos\theta\sin 2\phi)\hat{\varepsilon}^0_{yy} \\ & + (\cos\theta\cos 2\phi)\hat{\varepsilon}^0_{xy} + (\sin\theta\sin\phi)\hat{\varepsilon}^0_{xz} + (-\sin\theta\cos\phi)\hat{\varepsilon}^0_{yz} \end{aligned} \tag{I.5}$$

Therefore, the interface strain tensor $\boldsymbol{\varepsilon}^S$, which is a *two*-dimensional tensor, can be expressed as

$$\boldsymbol{\varepsilon}^S = \begin{bmatrix} \hat{\varepsilon}^0_{\theta\theta} & \hat{\varepsilon}^0_{\theta\phi} \\ \hat{\varepsilon}^0_{\theta\phi} & \hat{\varepsilon}^0_{\phi\phi} \end{bmatrix} \tag{I.6}$$

For calculation simplicity, the interface strain tensor is divided into the volumetric interface strain

tensor and the deviatoric interface strain tensor as

$$(\boldsymbol{\varepsilon}^S)^{vol} = \begin{bmatrix} \frac{1}{2}(\hat{\varepsilon}^0_{\theta\theta} + \hat{\varepsilon}^0_{\phi\phi}) & 0 \\ 0 & \frac{1}{2}(\hat{\varepsilon}^0_{\phi\phi} + \hat{\varepsilon}^0_{\theta\theta}) \end{bmatrix} \tag{I.7}$$

$$(\boldsymbol{\varepsilon}^S)^{dev} = \begin{bmatrix} \frac{1}{2}\hat{\varepsilon}^0_{\theta\theta} - \frac{1}{2}\hat{\varepsilon}^0_{\phi\phi} & \hat{\varepsilon}^0_{\theta\phi} \\ \hat{\varepsilon}^0_{\theta\phi} & \frac{1}{2}\hat{\varepsilon}^0_{\phi\phi} - \frac{1}{2}\hat{\varepsilon}^0_{\theta\theta} \end{bmatrix} \tag{I.8}$$

According to Eqs. (3.21)–(3.22), the interface stress $\boldsymbol{\tau}$ becomes

$$\boldsymbol{\tau} = 2K_S \cdot (\boldsymbol{\varepsilon}^S)^{vol} + 2\mu_S \cdot (\boldsymbol{\varepsilon}^S)^{dev} \tag{I.9}$$

and the components of interface stress is given as

$$\begin{aligned}
\tau_{\theta\theta} = {} & \hat{\varepsilon}^0_{xx}\left[2K_S(\tfrac{1}{2}\cos^2\theta\cos^2\phi + \tfrac{1}{2}\sin^2\phi) + 2\mu_S(\tfrac{1}{2}\cos^2\theta\cos^2\phi - \tfrac{1}{2}\sin^2\phi)\right] \\
& + \hat{\varepsilon}^0_{yy}\left[2K_S(\tfrac{1}{2}\cos^2\theta\sin^2\phi + \tfrac{1}{2}\cos^2\phi) + 2\mu_S(\tfrac{1}{2}\cos^2\theta\sin^2\phi - \tfrac{1}{2}\cos^2\phi)\right] \\
& + \hat{\varepsilon}^0_{zz}\left[2K_S(\tfrac{1}{2}\sin^2\theta) + 2\mu_S(\tfrac{1}{2}\sin^2\theta)\right] \\
& + \hat{\varepsilon}^0_{xy}\left[2K_S(\tfrac{1}{2}\cos^2\theta\sin 2\phi - \tfrac{1}{2}\sin 2\phi) + 2\mu_S(\tfrac{1}{2}\cos^2\theta\sin 2\phi + \tfrac{1}{2}\sin 2\phi)\right] \\
& + \hat{\varepsilon}^0_{xz}\left[2K_S(-\tfrac{1}{2}\sin 2\theta\cos\phi) + 2\mu_S(-\tfrac{1}{2}\sin 2\theta\cos\phi)\right] \\
& + \hat{\varepsilon}^0_{yz}\left[2K_S(-\tfrac{1}{2}\sin 2\theta\sin\phi) + 2\mu_S(-\tfrac{1}{2}\sin 2\theta\sin\phi)\right]
\end{aligned} \tag{I.10}$$

$$\begin{aligned}
\tau_{\phi\phi} = {} & \hat{\varepsilon}^0_{xx}\left[2K_S(\tfrac{1}{2}\cos^2\theta\cos^2\phi + \tfrac{1}{2}\sin^2\phi) + 2\mu_S(-\tfrac{1}{2}\cos^2\theta\cos^2\phi + \tfrac{1}{2}\sin^2\phi)\right] \\
& + \hat{\varepsilon}^0_{yy}\left[2K_S(\tfrac{1}{2}\cos^2\theta\sin^2\phi + \tfrac{1}{2}\cos^2\phi) + 2\mu_S(-\tfrac{1}{2}\cos^2\theta\sin^2\phi + \tfrac{1}{2}\cos^2\phi)\right] \\
& + \hat{\varepsilon}^0_{zz}\left[2K_S(\tfrac{1}{2}\sin^2\theta) + 2\mu_S(-\tfrac{1}{2}\sin^2\theta)\right] \\
& + \hat{\varepsilon}^0_{xy}\left[2K_S(\tfrac{1}{2}\cos^2\theta\sin 2\phi - \tfrac{1}{2}\sin 2\phi) + 2\mu_S(-\tfrac{1}{2}\cos^2\theta\sin 2\phi - \tfrac{1}{2}\sin 2\phi)\right] \\
& + \hat{\varepsilon}^0_{xz}\left[2K_S(-\tfrac{1}{2}\sin 2\theta\cos\phi) + 2\mu_S(\tfrac{1}{2}\sin 2\theta\cos\phi)\right] \\
& + \hat{\varepsilon}^0_{yz}\left[2K_S(-\tfrac{1}{2}\sin 2\theta\sin\phi) + 2\mu_S(\tfrac{1}{2}\sin 2\theta\sin\phi)\right]
\end{aligned} \tag{I.11}$$

$$
\begin{aligned}
\tau_{\theta\phi} = {} & \hat{\varepsilon}^0_{xx}\left[2\mu_S(-\tfrac{1}{2}\cos\theta\sin 2\phi)\right] \\
& + \hat{\varepsilon}^0_{yy}\left[2\mu_S(\tfrac{1}{2}\cos\theta\sin 2\phi)\right] \\
& + \hat{\varepsilon}^0_{xy}\left[2\mu_S(\cos\theta\cos 2\phi)\right] \\
& + \hat{\varepsilon}^0_{xz}\left[2\mu_S(\sin\theta\sin\phi)\right] \\
& + \hat{\varepsilon}^0_{yz}\left[2\mu_S(-\sin\theta\cos\phi)\right]
\end{aligned}
\tag{I.12}
$$

The interfacial strain discontinuity is along the normal direction of the interface. For a spherical particle, the normal direction is along the *r*-axis in the spherical coordinate system. Consequently, the unit normal vector takes the form

$$
\mathbf{n} = \begin{bmatrix} \sin\theta\cos\phi \\ \sin\theta\sin\phi \\ \cos\theta \end{bmatrix}
\tag{I.13}
$$

According to Eq. (3.13), the interfacial strain discontinuity can be written as

$$
\begin{aligned}
\boldsymbol{\varepsilon}^{\lambda} &= \frac{1}{2}(\boldsymbol{\lambda}\otimes\mathbf{n} + \mathbf{n}\otimes\boldsymbol{\lambda}) \\
&= \begin{bmatrix}
\lambda_1\sin\theta\cos\phi & \tfrac{1}{2}\lambda_1\sin\theta\sin\phi + \tfrac{1}{2}\lambda_2\sin\theta\cos\phi & \tfrac{1}{2}\lambda_1\cos\theta + \tfrac{1}{2}\lambda_3\sin\theta\cos\phi \\
\tfrac{1}{2}\lambda_1\sin\theta\sin\phi + \tfrac{1}{2}\lambda_2\sin\theta\cos\phi & \lambda_2\sin\theta\sin\phi & \tfrac{1}{2}\lambda_2\cos\theta + \tfrac{1}{2}\lambda_3\sin\theta\sin\phi \\
\tfrac{1}{2}\lambda_1\cos\theta + \tfrac{1}{2}\lambda_3\sin\theta\cos\phi & \tfrac{1}{2}\lambda_2\cos\theta + \tfrac{1}{2}\lambda_3\sin\theta\sin\phi & \lambda_3\cos\theta
\end{bmatrix}
\end{aligned}
\tag{I.14}
$$

Transformation of $\boldsymbol{\varepsilon}^{\lambda}$ into the spherical coordinate system gives

$$
\begin{aligned}
(\boldsymbol{\varepsilon}^{\lambda})^{Spherical} &= \mathbf{L}\cdot\boldsymbol{\varepsilon}^{\lambda}\cdot\mathbf{L}^{\mathrm{T}} \\
&= \begin{bmatrix}
\lambda_1\sin\theta\cos\phi + \lambda_2\sin\theta\sin\phi + \lambda_3\cos\theta & sym & sym \\
\tfrac{1}{2}\lambda_1\cos\theta\cos\phi + \tfrac{1}{2}\lambda_2\cos\theta\sin\phi - \tfrac{1}{2}\lambda_3\sin\theta & 0 & sym \\
-\tfrac{1}{2}\lambda_1\sin\phi + \tfrac{1}{2}\lambda_2\cos\phi & 0 & 0
\end{bmatrix}
\end{aligned}
\tag{I.15}
$$

where

$$
\varepsilon^{\lambda}_{rr} = \lambda_1\sin\theta\cos\phi + \lambda_2\sin\theta\sin\phi + \lambda_3\cos\theta
\tag{I.16}
$$

$$\varepsilon_{r\theta}^{\lambda} = \tfrac{1}{2}\lambda_1 \cos\theta\cos\phi + \tfrac{1}{2}\lambda_2 \cos\theta\sin\phi - \tfrac{1}{2}\lambda_3 \sin\theta \tag{I.17}$$

$$\varepsilon_{r\phi}^{\lambda} = -\tfrac{1}{2}\lambda_1 \sin\phi + \tfrac{1}{2}\lambda_2 \cos\phi \tag{I.18}$$

Transformation of the eigenstrain from the Cartesian coordinate to the spherical coordinate gives,

$$(\boldsymbol{\varepsilon}^*)^{Spherical} = \mathbf{L}\cdot\boldsymbol{\varepsilon}^*\cdot\mathbf{L}^{\mathrm{T}} \tag{I.19}$$

where

$$\begin{aligned}\varepsilon_{rr}^* = {} & (\sin^2\theta\cos^2\phi)\varepsilon_{xx}^* + (\sin^2\theta\sin^2\phi)\varepsilon_{yy}^* + (\cos^2\theta)\varepsilon_{zz}^* \\ & + (\sin^2\theta\sin 2\phi)\varepsilon_{xy}^* + (\sin 2\theta\cos\phi)\varepsilon_{xz}^* + (\sin 2\theta\sin\phi)\varepsilon_{yz}^*\end{aligned} \tag{I.20}$$

$$\begin{aligned}\varepsilon_{\theta\theta}^* = {} & (\cos^2\theta\cos^2\phi)\varepsilon_{xx}^* + (\cos^2\theta\sin^2\phi)\varepsilon_{yy}^* + (\sin^2\theta)\varepsilon_{zz}^* \\ & + (\cos^2\theta\sin 2\phi)\varepsilon_{xy}^* + (-\sin 2\theta\cos\phi)\varepsilon_{xz}^* + (-\sin 2\theta\sin\phi)\varepsilon_{yz}^*\end{aligned} \tag{I.21}$$

$$\varepsilon_{\phi\phi}^* = (\sin^2\phi)\varepsilon_{xx}^* + (\cos^2\phi)\varepsilon_{yy}^* + (-\sin 2\phi)\varepsilon_{xy}^* \tag{I.22}$$

$$\begin{aligned}\varepsilon_{r\theta}^* = {} & (\sin\theta\cos\theta\cos^2\phi)\varepsilon_{xx}^* + (\sin\theta\cos\theta\sin^2\phi)\varepsilon_{yy}^* + (-\sin\theta\cos\theta)\varepsilon_{zz}^* \\ & + (\sin\theta\cos\theta\sin 2\phi)\varepsilon_{xy}^* + (\cos 2\theta\cos\phi)\varepsilon_{xz}^* + (\cos 2\theta\sin\phi)\varepsilon_{yz}^*\end{aligned} \tag{I.23}$$

$$\begin{aligned}\varepsilon_{r\phi}^* = {} & (-\sin\theta\sin\phi\cos\phi)\varepsilon_{xx}^* + (\sin\theta\sin\phi\cos\phi)\varepsilon_{yy}^* \\ & + (\sin\theta\cos 2\phi)\varepsilon_{xy}^* + (-\cos\theta\sin\phi)\varepsilon_{xz}^* + (\cos\theta\cos\phi)\varepsilon_{yz}^*\end{aligned} \tag{I.24}$$

Similarly, divide the eigenstrain tensor and the interfacial strain discontinuity tensor into the volumetric part and the deviatoric part in the spherical coordinate system,

$$\boldsymbol{\varepsilon}^* = \begin{bmatrix} \varepsilon_{rr}^* & \varepsilon_{r\theta}^* & \varepsilon_{r\phi}^* \\ \varepsilon_{r\theta}^* & \varepsilon_{\theta\theta}^* & \varepsilon_{\theta\phi}^* \\ \varepsilon_{r\phi}^* & \varepsilon_{\theta\phi}^* & \varepsilon_{\phi\phi}^* \end{bmatrix} \tag{I.25}$$

$$(\boldsymbol{\varepsilon}^*)^{dev} = \begin{bmatrix} \tfrac{2}{3}\varepsilon_{rr}^* - \tfrac{1}{3}(\varepsilon_{\theta\theta}^* + \varepsilon_{\phi\phi}^*) & \varepsilon_{r\theta}^* & \varepsilon_{r\phi}^* \\ \varepsilon_{r\theta}^* & \tfrac{2}{3}\varepsilon_{\theta\theta}^* - \tfrac{1}{3}(\varepsilon_{rr}^* + \varepsilon_{\phi\phi}^*) & \varepsilon_{\theta\phi}^* \\ \varepsilon_{r\phi}^* & \varepsilon_{\theta\phi}^* & \tfrac{2}{3}\varepsilon_{\phi\phi}^* - \tfrac{1}{3}(\varepsilon_{rr}^* + \varepsilon_{\theta\theta}^*) \end{bmatrix} \tag{I.26}$$

$$(\boldsymbol{\varepsilon}^{*})^{vol}=\begin{bmatrix} \frac{1}{3}(\varepsilon_{rr}^{*}+\varepsilon_{\theta\theta}^{*}+\varepsilon_{\phi\phi}^{*}) & 0 & 0 \\ 0 & \frac{1}{3}(\varepsilon_{rr}^{*}+\varepsilon_{\theta\theta}^{*}+\varepsilon_{\phi\phi}^{*}) & 0 \\ 0 & 0 & \frac{1}{3}(\varepsilon_{rr}^{*}+\varepsilon_{\theta\theta}^{*}+\varepsilon_{\phi\phi}^{*}) \end{bmatrix} \tag{I.27}$$

$$(\boldsymbol{\varepsilon}^{\lambda})^{vol}=\begin{bmatrix} \frac{1}{3}(\varepsilon_{rr}^{\lambda}+\varepsilon_{\theta\theta}^{\lambda}+\varepsilon_{\phi\phi}^{\lambda}) & 0 & 0 \\ 0 & \frac{1}{3}(\varepsilon_{rr}^{\lambda}+\varepsilon_{\theta\theta}^{\lambda}+\varepsilon_{\phi\phi}^{\lambda}) & 0 \\ 0 & 0 & \frac{1}{3}(\varepsilon_{rr}^{\lambda}+\varepsilon_{\theta\theta}^{\lambda}+\varepsilon_{\phi\phi}^{\lambda}) \end{bmatrix} \tag{I.28}$$

$$(\boldsymbol{\varepsilon}^{\lambda})^{dev}=\begin{bmatrix} \frac{2}{3}\varepsilon_{rr}^{\lambda}-\frac{1}{3}(\varepsilon_{\theta\theta}^{\lambda}+\varepsilon_{\phi\phi}^{\lambda}) & \varepsilon_{r\theta}^{\lambda} & \varepsilon_{r\phi}^{\lambda} \\ \varepsilon_{r\theta}^{\lambda} & \frac{2}{3}\varepsilon_{\theta\theta}^{\lambda}-\frac{1}{3}(\varepsilon_{rr}^{\lambda}+\varepsilon_{\phi\phi}^{\lambda}) & \varepsilon_{\theta\phi}^{\lambda} \\ \varepsilon_{r\phi}^{\lambda} & \varepsilon_{\theta\phi}^{\lambda} & \frac{2}{3}\varepsilon_{\phi\phi}^{\lambda}-\frac{1}{3}(\varepsilon_{rr}^{\lambda}+\varepsilon_{\theta\theta}^{\lambda}) \end{bmatrix} \tag{I.29}$$

According to Eq. (3.18), interfacial stress discontinuity is obtained

$$[\boldsymbol{\sigma}]=3\hat{K}_0\left((\boldsymbol{\varepsilon}^{\lambda})^{vol}+(\boldsymbol{\varepsilon}^{*})^{vol}\right)+2\hat{\mu}_0\left((\boldsymbol{\varepsilon}^{\lambda})^{dev}+(\boldsymbol{\varepsilon}^{*})^{dev}\right), \tag{I.30}$$

and the detailed expressions are as follows,

$$\begin{aligned}[\sigma_{rr}] &= 3\hat{K}_0\left((\varepsilon_{rr}^{\lambda})^{vol}+(\varepsilon_{rr}^{*})^{vol}\right)+2\hat{\mu}_0\left((\varepsilon_{rr}^{\lambda})^{dev}+(\varepsilon_{rr}^{*})^{dev}\right) \\ &= (\hat{K}_0+\tfrac{4}{3}\hat{\mu}_0)(\lambda_1\sin\theta\cos\phi+\lambda_2\sin\theta\sin\phi+\lambda_3\cos\theta) \\ &+ \hat{K}_0(\varepsilon_{xx}^{*}+\varepsilon_{yy}^{*}+\varepsilon_{zz}^{*}) \\ &+ \hat{\mu}_0[(2\sin^2\theta\cos^2\phi-\tfrac{2}{3})\varepsilon_{xx}^{*}+(2\sin^2\theta\sin^2\phi-\tfrac{2}{3})\varepsilon_{yy}^{*}+(2\cos^2\theta-\tfrac{2}{3})\varepsilon_{zz}^{*} \\ &+ (2\sin^2\theta\sin 2\phi)\varepsilon_{xy}^{*}+(2\sin 2\theta\cos\phi)\varepsilon_{xz}^{*}+(2\sin 2\theta\sin\phi)\varepsilon_{yz}^{*}]\end{aligned} \tag{I.31}$$

$$\begin{aligned}[\sigma_{r\theta}] &= 2\hat{\mu}_0\left((\varepsilon_{r\theta}^{\lambda})^{dev}+(\varepsilon_{r\theta}^{*})^{dev}\right) \\ &= \hat{\mu}_0(\lambda_1\cos\theta\cos\phi+\lambda_2\cos\theta\sin\phi-\lambda_3\sin\theta) \\ &+ \hat{\mu}_0[(\sin 2\theta\cos^2\phi)\varepsilon_{xx}^{*}+(\sin 2\theta\sin^2\phi)\varepsilon_{yy}^{*}+(-\sin 2\theta)\varepsilon_{zz}^{*} \\ &+ (\sin 2\theta\sin 2\phi)\varepsilon_{xy}^{*}+(2\cos 2\theta\cos\phi)\varepsilon_{xz}^{*}+(2\cos 2\theta\sin\phi)\varepsilon_{yz}^{*}]\end{aligned} \tag{I.32}$$

$$\begin{aligned}[\sigma_{r\phi}] &= 2\hat{\mu}_0\left((\varepsilon_{r\phi}^{\lambda})^{dev}+(\varepsilon_{r\phi}^{*})^{dev}\right) \\ &= \hat{\mu}_0(-\lambda_1\sin\phi+\lambda_2\cos\phi) \\ &+ \hat{\mu}_0[(-\sin\theta\sin 2\phi)\varepsilon_{xx}^{*}+(\sin\theta\sin 2\phi)\varepsilon_{yy}^{*} \\ &+ (2\sin\theta\cos 2\phi)\varepsilon_{xy}^{*}+(-2\cos\theta\sin\phi)\varepsilon_{xz}^{*}+(2\cos\theta\cos\phi)\varepsilon_{yz}^{*}]\end{aligned} \tag{I.33}$$

Eqs. (3.55)–(3.57) are the left-hand side the *generalized* Young-Laplace equations in Eqs. (3.8)–(3.10), and the right-hand side of the *generalized* Young-Laplace equations can be presented as follows,

$$\begin{aligned}\tfrac{1}{a}(\tau_{\theta\theta}+\tau_{\phi\phi}) = \tfrac{1}{a}\{&\hat{\varepsilon}^0_{xx}[2K_S(1-\sin^2\theta\cos^2\phi)]\\ &+\hat{\varepsilon}^0_{yy}[2K_S(1-\sin^2\theta\sin^2\phi)]\\ &+\hat{\varepsilon}^0_{zz}[2K_S(1-\cos^2\theta)]\\ &+\hat{\varepsilon}^0_{xy}[2K_S(-\sin^2\theta\sin 2\phi)]\\ &+\hat{\varepsilon}^0_{xz}[2K_S(-\sin 2\theta\cos\phi)]\\ &+\hat{\varepsilon}^0_{yz}[2K_S(-\sin 2\theta\sin\phi)]\}\end{aligned} \tag{I.34}$$

$$\begin{aligned}&-\frac{1}{a}[\frac{\partial\tau_{\theta\theta}}{\partial\theta}+\frac{1}{\sin\theta}\frac{\partial\tau_{\theta\phi}}{\partial\phi}+(\tau_{\theta\theta}-\tau_{\phi\phi})\cot\theta]\\ &=-\tfrac{1}{a}\{\hat{\varepsilon}^0_{xx}[2K_S(-\sin\theta\cos\theta\cos^2\phi)\\ &\qquad+2\mu_S(-\sin\theta\cos\theta\cos^2\phi-\tfrac{\cos\theta}{\sin\theta}\cos 2\phi+\tfrac{\cos^3\theta}{\sin\theta}\cos^2\phi-\tfrac{\cos\theta}{\sin\theta}\sin^2\phi)]\\ &\quad+\hat{\varepsilon}^0_{yy}[2K_S(-\sin\theta\cos\theta\sin^2\phi)\\ &\qquad+2\mu_S(-\sin\theta\cos\theta\sin^2\phi+\tfrac{\cos\theta}{\sin\theta}\cos 2\phi+\tfrac{\cos^3\theta}{\sin\theta}\sin^2\phi-\tfrac{\cos\theta}{\sin\theta}\cos^2\phi)]\\ &\quad+\hat{\varepsilon}^0_{zz}[2K_S(\sin\theta\cos\theta)+2\mu_S(2\sin\theta\cos\theta)]\\ &\quad+\hat{\varepsilon}^0_{xy}[2K_S(-\sin\theta\cos\theta\sin 2\phi)+2\mu_S(-2\sin\theta\cos\theta\sin 2\phi)]\\ &\quad+\hat{\varepsilon}^0_{xz}[2K_S(-\cos 2\theta\cos\phi)+2\mu_S(-2\cos 2\theta\cos\phi)]\\ &\quad+\hat{\varepsilon}^0_{yz}[2K_S(-\cos 2\theta\sin\phi)+2\mu_S(-2\cos 2\theta\sin\phi)]\end{aligned} \tag{I.35}$$

$$
\begin{aligned}
&-\frac{1}{a}\left(\frac{\partial \tau_{\theta\phi}}{\partial\theta}+\frac{1}{\sin\theta}\frac{\partial \tau_{\phi\phi}}{\partial\phi}+2\tau_{\theta\phi}\cot\theta\right)\\
&=-\tfrac{1}{a}\{\hat{\varepsilon}^0_{xx}[2K_S(\sin\theta\sin\phi\cos\phi)+2\mu_S(2\sin\theta\sin\phi\cos\phi)]\\
&\quad+\hat{\varepsilon}^0_{yy}[2K_S(-\sin\theta\sin\phi\cos\phi)+2\mu_S(-2\sin\phi\cos\phi)]\\
&\quad+\hat{\varepsilon}^0_{xy}[2K_S(-\sin\theta\cos 2\phi)+2\mu_S(-2\sin\theta\cos 2\phi)]\\
&\quad+\hat{\varepsilon}^0_{xz}[2K_S(\cos\theta\sin\phi)+2\mu_S(2\cos\theta\sin\phi)]\\
&\quad+\hat{\varepsilon}^0_{yz}[2K_S(-\cos\theta\cos\phi)+2\mu_S(-2\cos\theta\cos\phi)]
\end{aligned}
\qquad \text{(I.36)}
$$

Further, the detailed expressions of the *generalized* Young-Laplace equations are obtained from Eqs. (I.31)–(I.36),

$$
\begin{aligned}
&(\hat{K}_0+\tfrac{4}{3}\hat{\mu}_0)(\lambda_1\sin\theta\cos\phi+\lambda_2\sin\theta\sin\phi+\lambda_3\cos\theta)\\
&+\varepsilon^*_{xx}[\hat{K}_0+\hat{\mu}_0(2\sin^2\theta\cos^2\phi-\tfrac{2}{3})]\\
&+\varepsilon^*_{yy}[\hat{K}_0+\hat{\mu}_0(2\sin^2\theta\sin^2\phi-\tfrac{2}{3})]\\
&+\varepsilon^*_{zz}[\hat{K}_0+\hat{\mu}_0(2\cos^2\theta-\tfrac{2}{3})]\\
&+\varepsilon^*_{xy}[\hat{\mu}_0(2\sin^2\theta\sin 2\phi)]\\
&+\varepsilon^*_{xz}[\hat{\mu}_0(2\sin 2\theta\cos\phi)]\\
&+\varepsilon^*_{yz}[\hat{\mu}_0(2\sin 2\theta\sin\phi)]\\
&=\tfrac{1}{a}\{\hat{\varepsilon}^0_{xx}[2K_S(1-\sin^2\theta\cos^2\phi)]\\
&\quad+\hat{\varepsilon}^0_{yy}[2K_S(1-\sin^2\theta\sin^2\phi)]\\
&\quad+\hat{\varepsilon}^0_{zz}[2K_S(1-\cos^2\theta)]\\
&\quad+\hat{\varepsilon}^0_{xy}[2K_S(-\sin^2\theta\sin 2\phi)]\\
&\quad+\hat{\varepsilon}^0_{xz}[2K_S(-\sin 2\theta\cos\phi)]\\
&\quad+\hat{\varepsilon}^0_{yz}[2K_S(-\sin 2\theta\sin\phi)]\}
\end{aligned}
\tag{I.37}
$$

$$
\begin{aligned}
&\hat{\mu}_0(\lambda_1\cos\theta\cos\phi+\lambda_2\cos\theta\sin\phi-\lambda_3\sin\theta)\\
&+\varepsilon^*_{xx}[\hat{\mu}_0[(\sin 2\theta\cos^2\phi)]+\varepsilon^*_{yy}[\hat{\mu}_0(\sin 2\theta\sin^2\phi)]+\varepsilon^*_{zz}[\hat{\mu}_0(-\sin 2\theta)]\\
&+\varepsilon^*_{xy}[\hat{\mu}_0(\sin 2\theta\sin 2\phi)]+\varepsilon^*_{xz}[\hat{\mu}_0(2\cos 2\theta\cos\phi)]+\varepsilon^*_{yz}[\hat{\mu}_0(2\cos 2\theta\sin\phi)]\\
&=-\tfrac{1}{a}\{\hat{\varepsilon}^0_{xx}[2K_S(-\sin\theta\cos\theta\cos^2\phi)\\
&\qquad+2\mu_S(-\sin\theta\cos\theta\cos^2\phi-\tfrac{\cos\theta}{\sin\theta}\cos 2\phi+\tfrac{\cos^3\theta}{\sin\theta}\cos^2\phi-\tfrac{\cos\theta}{\sin\theta}\sin^2\phi)]\\
&\quad+\hat{\varepsilon}^0_{yy}[2K_S(-\sin\theta\cos\theta\sin^2\phi)\\
&\qquad+2\mu_S(-\sin\theta\cos\theta\sin^2\phi+\tfrac{\cos\theta}{\sin\theta}\cos 2\phi+\tfrac{\cos^3\theta}{\sin\theta}\sin^2\phi-\tfrac{\cos\theta}{\sin\theta}\cos^2\phi)]\\
&\quad+\hat{\varepsilon}^0_{zz}[2K_S(\sin\theta\cos\theta)+2\mu_S(2\sin\theta\cos\theta)]\\
&\quad+\hat{\varepsilon}^0_{xy}[2K_S(-\sin\theta\cos\theta\sin 2\phi)+2\mu_S(-2\sin\theta\cos\theta\sin 2\phi)]\\
&\quad+\hat{\varepsilon}^0_{xz}[2K_S(-\cos 2\theta\cos\phi)+2\mu_S(-2\cos 2\theta\cos\phi)]\\
&\quad+\hat{\varepsilon}^0_{yz}[2K_S(-\cos 2\theta\sin\phi)+2\mu_S(-2\cos 2\theta\sin\phi)]
\end{aligned}
\tag{I.38}
$$

$$
\begin{aligned}
&\hat{\mu}_0(-\lambda_1 \sin\phi + \lambda_2 \cos\phi) \\
&+\varepsilon^*_{xx}[\hat{\mu}_0[(-\sin\theta \sin 2\phi)] + \varepsilon^*_{yy}[\hat{\mu}_0(\sin\theta \sin 2\phi)] \\
&+\varepsilon^*_{xy}[\hat{\mu}_0(2\sin\theta \cos 2\phi)] + \varepsilon^*_{xz}[\hat{\mu}_0(-2\cos\theta \sin\phi)] + \varepsilon^*_{yz}[\hat{\mu}_0(2\cos\theta \cos\phi)] \\
&= -\tfrac{1}{a}\{\hat{\varepsilon}^0_{xx}[2K_S(\sin\theta \sin\phi \cos\phi) + 2\mu_S(2\sin\theta \sin\phi \cos\phi)] \\
&\quad + \hat{\varepsilon}^0_{yy}[2K_S(-\sin\theta \sin\phi \cos\phi) + 2\mu_S(-2\sin\phi \cos\phi)] \\
&\quad + \hat{\varepsilon}^0_{xy}[2K_S(-\sin\theta \cos 2\phi) + 2\mu_S(-2\sin\theta \cos 2\phi)] \\
&\quad + \hat{\varepsilon}^0_{xz}[2K_S(\cos\theta \sin\phi) + 2\mu_S(2\cos\theta \sin\phi)] \\
&\quad + \hat{\varepsilon}^0_{yz}[2K_S(-\cos\theta \cos\phi) + 2\mu_S(-2\cos\theta \cos\phi)]
\end{aligned}
\tag{I.39}
$$

As a consequence, the amplitude of the interfacial strain discontinuity, λ_1, λ_2 and λ_3, can be expressed by the effective strain $\hat{\boldsymbol{\varepsilon}}^0$ in matrix and the eigenstrain $\boldsymbol{\varepsilon}^*$ in the inclusion.

Solving Eqs. (I.37)–(I.39), we have

$$
\begin{aligned}
\lambda_3 = \frac{1}{a}\{\hat{\varepsilon}^0_{xx}[&\frac{2K_S}{\hat{K}_0+\frac{4}{3}\hat{\mu}_0}\left(\cos\theta-\sin^2\theta\cos\theta\cos^2\phi\right)+\frac{2K_S}{\hat{\mu}_0}\left(-\sin^2\theta\cos\theta\cos^2\phi\right)\\
&+\frac{2\mu_S}{\hat{\mu}_0}\left(-\sin^2\theta\cos\theta\cos^2\phi-\cos\theta\cos 2\phi+\cos^3\theta\cos^2\phi-\cos\theta\sin^2\phi\right)]\\
+\hat{\varepsilon}^0_{yy}[&\frac{2K_S}{\hat{K}_0+\frac{4}{3}\hat{\mu}_0}\left(\cos\theta-\sin^2\theta\cos\theta\sin^2\phi\right)+\frac{2K_S}{\hat{\mu}_0}\left(-\sin^2\theta\cos\theta\sin^2\phi\right)\\
&+\frac{2\mu_S}{\hat{\mu}_0}\left(-\sin^2\theta\cos\theta\sin^2\phi+\cos\theta\cos 2\phi+\cos^3\theta\sin^2\phi-\cos\theta\cos^2\phi\right)]\\
+\hat{\varepsilon}^0_{zz}[&\frac{2K_S}{\hat{K}_0+\frac{4}{3}\hat{\mu}_0}\left(\sin^2\theta\cos\theta\right)+\frac{2K_S}{\hat{\mu}_0}\left(\sin^2\theta\cos\theta\right)+\frac{2\mu_S}{\hat{\mu}_0}\left(2\sin^2\theta\cos\theta\right)]\\
+\hat{\varepsilon}^0_{xy}[&\frac{2K_S}{\hat{K}_0+\frac{4}{3}\hat{\mu}_0}\left(-\sin^2\theta\cos\theta\sin 2\phi\right)+\frac{2K_S}{\hat{\mu}_0}\left(-\sin^2\theta\cos\theta\sin 2\phi\right)+\frac{2\mu_S}{\hat{\mu}_0}\left(-2\sin^2\theta\cos\theta\sin 2\phi\right)]\\
+\hat{\varepsilon}^0_{xz}[&\frac{2K_S}{\hat{K}_0+\frac{4}{3}\hat{\mu}_0}\left(-\sin 2\theta\cos\theta\cos\phi\right)+\frac{2K_S}{\hat{\mu}_0}\left(-\sin\theta\cos 2\theta\cos\phi\right)+\frac{2\mu_S}{\hat{\mu}_0}\left(-2\sin\theta\cos 2\theta\cos\phi\right)]\\
+\hat{\varepsilon}^0_{yz}[&\frac{2K_S}{\hat{K}_0+\frac{4}{3}\hat{\mu}_0}\left(-\sin 2\theta\cos\theta\sin\phi\right)+\frac{2K_S}{\hat{\mu}_0}\left(-\sin\theta\cos 2\theta\sin\phi\right)+\frac{2\mu_S}{\hat{\mu}_0}\left(-2\sin\theta\cos 2\theta\sin\phi\right)]\}\\
+\varepsilon^*_{xx}[&\frac{\hat{K}_0}{\hat{K}_0+\frac{4}{3}\hat{\mu}_0}\left(-\cos\theta\right)+\frac{\hat{\mu}_0}{\hat{K}_0+\frac{4}{3}\hat{\mu}_0}\left(\frac{2}{3}\cos\theta-2\sin^2\theta\cos\theta\cos^2\phi\right)+2\sin^2\theta\cos\theta\cos^2\phi]\\
+\varepsilon^*_{yy}[&\frac{\hat{K}_0}{\hat{K}_0+\frac{4}{3}\hat{\mu}_0}\left(-\cos\theta\right)+\frac{\hat{\mu}_0}{\hat{K}_0+\frac{4}{3}\hat{\mu}_0}\left(\frac{2}{3}\cos\theta-2\sin^2\theta\cos\theta\sin^2\phi\right)+2\sin^2\theta\cos\theta\sin^2\phi]\\
+\varepsilon^*_{zz}[&\frac{\hat{K}_0}{\hat{K}_0+\frac{4}{3}\hat{\mu}_0}\left(-\cos\theta\right)+\frac{\hat{\mu}_0}{\hat{K}_0+\frac{4}{3}\hat{\mu}_0}\left(\frac{2}{3}\cos\theta-2\cos^3\theta\right)-2\sin^2\theta\cos\theta]\\
+\varepsilon^*_{xy}[&\frac{\hat{\mu}_0}{\hat{K}_0+\frac{4}{3}\hat{\mu}_0}\left(-2\sin^2\theta\cos\theta\sin 2\phi\right)+4\sin^2\theta\cos\theta\sin\phi\cos\phi]\\
+\varepsilon^*_{xz}[&\frac{\hat{\mu}_0}{\hat{K}_0+\frac{4}{3}\hat{\mu}_0}\left(-2\sin 2\theta\cos\theta\cos\phi\right)+2\sin\theta\cos 2\theta\cos\phi]\\
+\varepsilon^*_{yz}[&\frac{\hat{\mu}_0}{\hat{K}_0+\frac{4}{3}\hat{\mu}_0}\left(-2\sin 2\theta\cos\theta\sin\phi\right)+2\sin\theta\cos 2\theta\sin\phi]
\end{aligned}
\tag{I.40}
$$

$$
\begin{aligned}
\lambda_2 = \frac{1}{a}\{\hat{\varepsilon}^0_{xx}[&\frac{2K_S}{\hat{K}_0+\frac{4}{3}\hat{\mu}_0}\left(\sin\theta\sin\phi-\sin^3\theta\sin\phi\cos^2\phi\right)+\frac{2K_S}{\hat{\mu}_0}\left(\sin\theta\cos^2\theta\sin\phi\cos^2\phi-\sin\theta\sin\phi\cos^2\phi\right)\\
&+\frac{2\mu_S}{\hat{\mu}_0}\left(-2\sin^3\theta\sin\phi\cos^2\phi\right)]\\
+\hat{\varepsilon}^0_{yy}[&\frac{2K_S}{\hat{K}_0+\frac{4}{3}\hat{\mu}_0}\left(\sin\theta\sin\phi-\sin^3\theta\sin^3\phi\right)+\frac{2K_S}{\hat{\mu}_0}\left(\sin\theta\cos^2\theta\sin^3\phi+\sin\theta\sin\phi\cos^2\phi\right)\\
&+\frac{2\mu_S}{\hat{\mu}_0}\left(2\sin\theta\cos^2\theta\sin^3\phi+\sin\theta\sin 2\phi\cos\phi\right)]\\
+\hat{\varepsilon}^0_{zz}[&\frac{2K_S}{\hat{K}_0+\frac{4}{3}\hat{\mu}_0}\left(\sin^3\theta\sin\phi\right)+\frac{2K_S}{\hat{\mu}_0}\left(-\sin\theta\cos^2\theta\sin\phi\right)+\frac{2\mu_S}{\hat{\mu}_0}\left(-2\sin\theta\cos^2\theta\sin\phi\right)]\\
+\hat{\varepsilon}^0_{xy}[&\frac{2K_S}{\hat{K}_0+\frac{4}{3}\hat{\mu}_0}\left(-\sin^3\theta\sin\phi\sin 2\phi\right)+\frac{2K_S}{\hat{\mu}_0}\left(\sin\theta\cos^2\theta\sin\phi\sin 2\phi+\sin\theta\cos\phi\cos 2\phi\right)\\
&+\frac{2\mu_S}{\hat{\mu}_0}\left(2\sin\theta\cos^2\theta\sin\phi\sin 2\phi+2\sin\theta\cos\phi\cos 2\phi\right)]\\
+\hat{\varepsilon}^0_{xz}[&\frac{2K_S}{\hat{K}_0+\frac{4}{3}\hat{\mu}_0}\left(-\sin\theta\sin 2\theta\sin\phi\cos\phi\right)+\frac{2K_S}{\hat{\mu}_0}\left(\cos\theta\cos 2\theta\sin\phi\cos\phi-\cos\theta\sin\phi\cos\phi\right)\\
&+\frac{2\mu_S}{\hat{\mu}_0}\left(2\cos\theta\cos 2\theta\sin\phi\cos\phi-2\cos\theta\sin\phi\cos\phi\right)]\\
+\hat{\varepsilon}^0_{yz}[&\frac{2K_S}{\hat{K}_0+\frac{4}{3}\hat{\mu}_0}\left(-\sin\theta\sin 2\theta\sin^2\phi\right)+\frac{2K_S}{\hat{\mu}_0}\left(\cos\theta\cos 2\theta\sin^2\phi+\cos\theta\cos^2\phi\right)\\
&+\frac{2\mu_S}{\hat{\mu}_0}\left(2\cos\theta\cos 2\theta\sin^2\phi+2\cos\theta\cos^2\phi\right)]\}\\
+\varepsilon^*_{xx}[&\frac{\hat{K}_0}{\hat{K}_0+\frac{4}{3}\hat{\mu}_0}\left(-\sin\theta\sin\phi\right)+\frac{\hat{\mu}_0}{\hat{K}_0+\frac{4}{3}\hat{\mu}_0}\left(\frac{2}{3}\sin\theta\sin\phi-2\sin^3\theta\sin\phi\cos^2\phi\right)\\
&-2\sin\theta\cos^2\theta\sin\phi\cos^2\phi+2\sin\theta\sin\phi\cos^2\phi]\\
+\varepsilon^*_{yy}[&\frac{\hat{K}_0}{\hat{K}_0+\frac{4}{3}\hat{\mu}_0}\left(-\sin\theta\sin\phi\right)+\frac{\hat{\mu}_0}{\hat{K}_0+\frac{4}{3}\hat{\mu}_0}\left(\frac{2}{3}\sin\theta\sin\phi-2\sin^3\theta\sin^3\phi\right)\\
&-2\sin\theta\cos^2\theta\sin^3\phi-2\sin\theta\sin\phi\cos^2\phi]\\
+\varepsilon^*_{zz}[&\frac{\hat{K}_0}{\hat{K}_0+\frac{4}{3}\hat{\mu}_0}\left(-\sin\theta\sin\phi\right)+\frac{\hat{\mu}_0}{\hat{K}_0+\frac{4}{3}\hat{\mu}_0}\left(\frac{2}{3}\sin\theta\sin\phi-2\sin\theta\cos^2\theta\sin\phi\right)\\
&+2\sin\theta\cos^2\theta\sin\phi]\\
+\varepsilon^*_{xy}[&\frac{\hat{\mu}_0}{\hat{K}_0+\frac{4}{3}\hat{\mu}_0}\left(-2\sin^3\theta\sin\phi\sin 2\phi\right)-4\sin\theta\cos^2\theta\sin^2\phi\cos\phi-2\sin\theta\cos\phi\cos 2\phi]\\
+\varepsilon^*_{xz}[&\frac{\hat{\mu}_0}{\hat{K}_0+\frac{4}{3}\hat{\mu}_0}\left(-\sin\theta\sin 2\theta\sin 2\phi\right)-\cos\theta\cos 2\theta\sin 2\phi+\cos\theta\sin 2\phi]\\
+\varepsilon^*_{yz}[&\frac{\hat{\mu}_0}{\hat{K}_0+\frac{4}{3}\hat{\mu}_0}\left(-2\sin\theta\sin 2\theta\sin^2\phi\right)-2\cos\theta\cos 2\theta\sin^2\phi-2\cos\theta\cos^2\phi]
\end{aligned}
\tag{I.41}
$$

$$
\begin{aligned}
\lambda_1 = \frac{1}{a}\{\hat{\varepsilon}^0_{xx}[&\frac{2K_S}{\hat{K}_0+\frac{4}{3}\hat{\mu}_0}\left(\sin\theta\cos\phi-\sin^3\theta\cos^3\phi\right)+\frac{2K_S}{\hat{\mu}_0}\left(\sin\theta\cos^2\theta\cos^3\phi+\sin\theta\sin^2\phi\cos\phi\right)\\
&+\frac{2\mu_S}{\hat{\mu}_0}\left(2\sin\theta\cos^2\theta\cos^3\phi+\sin\theta\sin\phi\sin 2\phi\right)]\\
+\hat{\varepsilon}^0_{yy}[&\frac{2K_S}{\hat{K}_0+\frac{4}{3}\hat{\mu}_0}\left(\sin\theta\cos\phi-\sin^3\theta\sin^2\phi\cos\phi\right)+\frac{2K_S}{\hat{\mu}_0}\left(\sin\theta\cos^2\theta\sin^2\phi\cos\phi-\sin\theta\sin^2\phi\cos\phi\right)\\
&+\frac{2\mu_S}{\hat{\mu}_0}\left(-2\sin^3\theta\sin^2\phi\cos\phi\right)]\\
+\hat{\varepsilon}^0_{zz}[&\frac{2K_S}{\hat{K}_0+\frac{4}{3}\hat{\mu}_0}\left(\sin^3\theta\cos\phi\right)+\frac{2K_S}{\hat{\mu}_0}\left(-\sin\theta\cos^2\theta\cos\phi\right)+\frac{2\mu_S}{\hat{\mu}_0}\left(-2\sin\theta\cos^2\theta\cos\phi\right)]\\
+\hat{\varepsilon}^0_{xy}[&\frac{2K_S}{\hat{K}_0+\frac{4}{3}\hat{\mu}_0}\left(-\sin^3\theta\sin 2\phi\cos\phi\right)+\frac{2K_S}{\hat{\mu}_0}\left(\sin\theta\cos^2\theta\sin 2\phi\cos\phi-\sin\theta\sin\phi\cos 2\phi\right)\\
&+\frac{2\mu_S}{\hat{\mu}_0}\left(2\sin\theta\cos^2\theta\sin 2\phi\cos\phi-2\sin\theta\sin\phi\cos 2\phi\right)]\\
+\hat{\varepsilon}^0_{xz}[&\frac{2K_S}{\hat{K}_0+\frac{4}{3}\hat{\mu}_0}\left(-\sin\theta\sin 2\theta\cos^2\phi\right)+\frac{2K_S}{\hat{\mu}_0}\left(\cos\theta\cos 2\theta\cos^2\phi+\cos\theta\sin^2\phi\right)\\
&+\frac{2\mu_S}{\hat{\mu}_0}\left(2\cos\theta\cos 2\theta\cos^2\phi+2\cos\theta\sin^2\phi\right)]\\
+\hat{\varepsilon}^0_{yz}[&\frac{2K_S}{\hat{K}_0+\frac{4}{3}\hat{\mu}_0}\left(-\sin\theta\sin 2\theta\sin\phi\cos\phi\right)+\frac{2K_S}{\hat{\mu}_0}\left(\cos\theta\cos 2\theta\sin\phi\cos\phi-\cos\theta\sin\phi\cos\phi\right)\\
&+\frac{2\mu_S}{\hat{\mu}_0}\left(2\cos\theta\cos 2\theta\sin\phi\cos\phi-2\cos\theta\sin\phi\cos\phi\right)]\}\\
+\varepsilon^*_{xx}[&\frac{\hat{K}_0}{\hat{K}_0+\frac{4}{3}\hat{\mu}_0}\left(-\sin\theta\cos\phi\right)+\frac{\hat{\mu}_0}{\hat{K}_0+\frac{4}{3}\hat{\mu}_0}\left(\frac{2}{3}\sin\theta\cos\phi-2\sin^3\theta\cos^3\phi\right)\\
&-2\sin\theta\cos^2\theta\cos^3\phi-2\sin\theta\sin^2\phi\cos\phi]\\
+\varepsilon^*_{yy}[&\frac{\hat{K}_0}{\hat{K}_0+\frac{4}{3}\hat{\mu}_0}\left(-\sin\theta\cos\phi\right)+\frac{\hat{\mu}_0}{\hat{K}_0+\frac{4}{3}\hat{\mu}_0}\left(\frac{2}{3}\sin\theta\cos\phi-2\sin^3\theta\sin^2\phi\cos\phi\right)\\
&-2\sin\theta\cos^2\theta\sin^2\phi\cos\phi+2\sin\theta\sin^2\phi\cos\phi]\\
+\varepsilon^*_{zz}[&\frac{\hat{K}_0}{\hat{K}_0+\frac{4}{3}\hat{\mu}_0}\left(-\sin\theta\cos\phi\right)+\frac{\hat{\mu}_0}{\hat{K}_0+\frac{4}{3}\hat{\mu}_0}\left(\frac{2}{3}\sin\theta\cos\phi-2\sin\theta\cos^2\theta\cos\phi\right)\\
&+2\sin\theta\cos^2\theta\cos\phi]\\
+\varepsilon^*_{xy}[&\frac{\hat{\mu}_0}{\hat{K}_0+\frac{4}{3}\hat{\mu}_0}\left(-2\sin^3\theta\sin 2\phi\cos\phi\right)-4\sin\theta\cos^2\theta\sin\phi\cos^2\phi+2\sin\theta\sin\phi\cos 2\phi]\\
+\varepsilon^*_{xz}[&\frac{\hat{\mu}_0}{\hat{K}_0+\frac{4}{3}\hat{\mu}_0}\left(-\sin\theta\sin 2\theta\cos^2\phi\right)-2\cos\theta\cos 2\theta\cos^2\phi-2\cos\theta\sin^2\phi]\\
+\varepsilon^*_{yz}[&\frac{\hat{\mu}_0}{\hat{K}_0+\frac{4}{3}\hat{\mu}_0}\left(-2\sin\theta\sin 2\theta\sin\phi\cos\phi\right)-2\cos\theta\cos 2\theta\sin\phi\cos\phi+2\cos\theta\sin\phi\cos\phi]
\end{aligned}
$$

(I.42)

Since the volume averaged strain field is desired, the interfacial strain discontinuity tensor is averaged over the entire interface area, which gives

$$
\begin{aligned}
&\frac{1}{4\pi}\int_0^{2\pi}\int_0^{\pi}(\lambda_1\sin\theta\cos\phi)\sin\theta\,\mathrm{d}\theta\,\mathrm{d}\phi \\
&=\varepsilon^*_{xx}\left[\frac{\hat{K}_0}{\hat{K}_0+\frac{4}{3}\hat{\mu}_0}\left(-\frac{1}{3}\right)+\frac{\hat{\mu}_0}{\hat{K}_0+\frac{4}{3}\hat{\mu}_0}\left(-\frac{8}{45}\right)-\frac{4}{15}\right] \\
&+\varepsilon^*_{yy}\left[\frac{\hat{K}_0}{\hat{K}_0+\frac{4}{3}\hat{\mu}_0}\left(-\frac{1}{3}\right)+\frac{\hat{\mu}_0}{\hat{K}_0+\frac{4}{3}\hat{\mu}_0}\left(\frac{4}{45}\right)+\frac{2}{15}\right] \\
&+\varepsilon^*_{zz}\left[\frac{\hat{K}_0}{\hat{K}_0+\frac{4}{3}\hat{\mu}_0}\left(-\frac{1}{3}\right)+\frac{\hat{\mu}_0}{\hat{K}_0+\frac{4}{3}\hat{\mu}_0}\left(\frac{4}{45}\right)+\frac{2}{15}\right] \\
&+\hat{\varepsilon}^0_{xx}\left[\frac{K_S}{a\left(\hat{K}_0+\frac{4}{3}\hat{\mu}_0\right)}\left(\frac{4}{15}\right)+\frac{K_S}{a\hat{\mu}_0}\left(\frac{4}{15}\right)+\frac{\mu_S}{a\hat{\mu}_0}\left(\frac{8}{15}\right)\right] \\
&+\hat{\varepsilon}^0_{yy}\left[\frac{K_S}{a\left(\hat{K}_0+\frac{4}{3}\hat{\mu}_0\right)}\left(\frac{8}{15}\right)+\frac{K_S}{a\hat{\mu}_0}\left(-\frac{2}{15}\right)+\frac{\mu_S}{a\hat{\mu}_0}\left(-\frac{4}{15}\right)\right] \\
&+\hat{\varepsilon}^0_{zz}\left[\frac{K_S}{a\left(\hat{K}_0+\frac{4}{3}\hat{\mu}_0\right)}\left(\frac{8}{15}\right)+\frac{K_S}{a\hat{\mu}_0}\left(-\frac{2}{15}\right)+\frac{\mu_S}{a\hat{\mu}_0}\left(-\frac{4}{15}\right)\right]
\end{aligned}
\tag{I.43}
$$

$$
\begin{aligned}
&\frac{1}{4\pi}\int_0^{2\pi}\int_0^{\pi}(\lambda_1\sin\theta\sin\phi)\sin\theta\,\mathrm{d}\theta\,\mathrm{d}\phi \\
&=\varepsilon^*_{xy}\left[\frac{\hat{\mu}_0}{\hat{K}_0+\frac{4}{3}\hat{\mu}_0}\left(-\frac{4}{15}\right)-\frac{2}{5}\right] \\
&+\hat{\varepsilon}^0_{xy}\left[\frac{K_S}{a\left(\hat{K}_0+\frac{4}{3}\hat{\mu}_0\right)}\left(-\frac{4}{15}\right)+\frac{K_S}{a\hat{\mu}_0}\left(\frac{2}{5}\right)+\frac{\mu_S}{a\hat{\mu}_0}\left(\frac{4}{5}\right)\right]
\end{aligned}
\tag{I.44}
$$

$$
\begin{aligned}
&\frac{1}{4\pi}\int_0^{2\pi}\int_0^{\pi}(\lambda_1\cos\theta)\sin\theta\,\mathrm{d}\theta\,\mathrm{d}\phi \\
&=\varepsilon^*_{xz}\left[\frac{\hat{\mu}_0}{\hat{K}_0+\frac{4}{3}\hat{\mu}_0}\left(-\frac{4}{15}\right)-\frac{2}{5}\right] \\
&+\hat{\varepsilon}^0_{xz}\left[\frac{K_S}{a\left(\hat{K}_0+\frac{4}{3}\hat{\mu}_0\right)}\left(-\frac{4}{15}\right)+\frac{K_S}{a\hat{\mu}_0}\left(\frac{2}{5}\right)+\frac{\mu_S}{a\hat{\mu}_0}\left(\frac{4}{5}\right)\right]
\end{aligned}
\tag{I.45}
$$

$$\frac{1}{4\pi}\int_0^{2\pi}\int_0^{\pi}(\lambda_2\sin\theta\cos\phi)\sin\theta\,\mathrm{d}\theta\,\mathrm{d}\phi$$
$$=\varepsilon_{xy}^{*}\left[\frac{\hat{\mu}_0}{\hat{K}_0+\frac{4}{3}\hat{\mu}_0}\left(-\frac{4}{15}\right)-\frac{2}{5}\right]$$
$$+\hat{\varepsilon}_{xy}^{0}\left[\frac{K_S}{a\left(\hat{K}_0+\frac{4}{3}\hat{\mu}_0\right)}\left(-\frac{4}{15}\right)+\frac{K_S}{a\hat{\mu}_0}\left(\frac{2}{5}\right)+\frac{\mu_S}{a\hat{\mu}_0}\left(\frac{4}{5}\right)\right] \tag{I.46}$$

$$\frac{1}{4\pi}\int_0^{2\pi}\int_0^{\pi}(\lambda_2\sin\theta\sin\phi)\sin\theta\,\mathrm{d}\theta\,\mathrm{d}\phi$$
$$=\varepsilon_{xx}^{*}\left[\frac{\hat{K}_0}{\hat{K}_0+\frac{4}{3}\hat{\mu}_0}\left(-\frac{1}{3}\right)+\frac{\hat{\mu}_0}{\hat{K}_0+\frac{4}{3}\hat{\mu}_0}\left(\frac{4}{45}\right)+\frac{2}{15}\right]$$
$$+\varepsilon_{yy}^{*}\left[\frac{\hat{K}_0}{\hat{K}_0+\frac{4}{3}\hat{\mu}_0}\left(-\frac{1}{3}\right)+\frac{\hat{\mu}_0}{\hat{K}_0+\frac{4}{3}\hat{\mu}_0}\left(-\frac{8}{45}\right)-\frac{4}{15}\right]$$
$$+\varepsilon_{zz}^{*}\left[\frac{\hat{K}_0}{\hat{K}_0+\frac{4}{3}\hat{\mu}_0}\left(-\frac{1}{3}\right)+\frac{\hat{\mu}_0}{\hat{K}_0+\frac{4}{3}\hat{\mu}_0}\left(\frac{4}{45}\right)+\frac{2}{15}\right] \tag{I.47}$$
$$+\hat{\varepsilon}_{xx}^{0}\left[\frac{K_S}{a\left(\hat{K}_0+\frac{4}{3}\hat{\mu}_0\right)}\left(\frac{8}{15}\right)+\frac{K_S}{a\hat{\mu}_0}\left(-\frac{2}{15}\right)+\frac{\mu_S}{a\hat{\mu}_0}\left(-\frac{4}{15}\right)\right]$$
$$+\hat{\varepsilon}_{yy}^{0}\left[\frac{K_S}{a\left(\hat{K}_0+\frac{4}{3}\hat{\mu}_0\right)}\left(\frac{4}{15}\right)+\frac{K_S}{a\hat{\mu}_0}\left(\frac{4}{15}\right)+\frac{\mu_S}{a\hat{\mu}_0}\left(\frac{8}{15}\right)\right]$$
$$+\hat{\varepsilon}_{zz}^{0}\left[\frac{K_S}{a\left(\hat{K}_0+\frac{4}{3}\hat{\mu}_0\right)}\left(\frac{8}{15}\right)+\frac{K_S}{a\hat{\mu}_0}\left(-\frac{2}{15}\right)+\frac{\mu_S}{a\hat{\mu}_0}\left(-\frac{4}{15}\right)\right]$$

$$\frac{1}{4\pi}\int_0^{2\pi}\int_0^{\pi}(\lambda_2\cos\theta)\sin\theta\,\mathrm{d}\theta\,\mathrm{d}\phi$$
$$=\varepsilon_{yz}^{*}\left[\frac{\hat{\mu}_0}{\hat{K}_0+\frac{4}{3}\hat{\mu}_0}\left(-\frac{4}{15}\right)-\frac{2}{5}\right]$$
$$+\hat{\varepsilon}_{yz}^{0}\left[\frac{K_S}{a\left(\hat{K}_0+\frac{4}{3}\hat{\mu}_0\right)}\left(-\frac{4}{15}\right)+\frac{K_S}{a\hat{\mu}_0}\left(\frac{2}{5}\right)+\frac{\mu_S}{a\hat{\mu}_0}\left(\frac{4}{5}\right)\right] \tag{I.48}$$

$$\frac{1}{4\pi}\int_0^{2\pi}\int_0^{\pi}(\lambda_3\sin\theta\cos\phi)\sin\theta\,\mathrm{d}\theta\,\mathrm{d}\phi$$
$$=\varepsilon_{xz}^{*}\left[\frac{\hat{\mu}_0}{\hat{K}_0+\frac{4}{3}\hat{\mu}_0}\left(-\frac{4}{15}\right)-\frac{2}{5}\right]$$
$$+\hat{\varepsilon}_{xz}^{0}\left[\frac{K_S}{a\left(\hat{K}_0+\frac{4}{3}\hat{\mu}_0\right)}\left(-\frac{4}{15}\right)+\frac{K_S}{a\hat{\mu}_0}\left(\frac{2}{5}\right)+\frac{\mu_S}{a\hat{\mu}_0}\left(\frac{4}{5}\right)\right] \tag{I.49}$$

$$\frac{1}{4\pi}\int_0^{2\pi}\int_0^{\pi}(\lambda_3\sin\theta\sin\phi)\sin\theta\,\mathrm{d}\theta\,\mathrm{d}\phi$$
$$=\varepsilon_{yz}^{*}\left[\frac{\hat{\mu}_0}{\hat{K}_0+\frac{4}{3}\hat{\mu}_0}\left(-\frac{4}{15}\right)-\frac{2}{5}\right]$$
$$+\hat{\varepsilon}_{yz}^{0}\left[\frac{K_S}{a\left(\hat{K}_0+\frac{4}{3}\hat{\mu}_0\right)}\left(-\frac{4}{15}\right)+\frac{K_S}{a\hat{\mu}_0}\left(\frac{2}{5}\right)+\frac{\mu_S}{a\hat{\mu}_0}\left(\frac{4}{5}\right)\right] \tag{I.50}$$

$$\frac{1}{4\pi}\int_0^{2\pi}\int_0^{\pi}(\lambda_3\cos\theta)\sin\theta\,\mathrm{d}\theta\,\mathrm{d}\phi$$
$$=\varepsilon_{xx}^{*}\left[\frac{\hat{K}_0}{\hat{K}_0+\frac{4}{3}\hat{\mu}_0}\left(-\frac{1}{3}\right)+\frac{\hat{\mu}_0}{\hat{K}_0+\frac{4}{3}\hat{\mu}_0}\left(\frac{4}{45}\right)+\frac{2}{15}\right]$$
$$+\varepsilon_{yy}^{*}\left[\frac{\hat{K}_0}{\hat{K}_0+\frac{4}{3}\hat{\mu}_0}\left(-\frac{1}{3}\right)+\frac{\hat{\mu}_0}{\hat{K}_0+\frac{4}{3}\hat{\mu}_0}\left(\frac{4}{45}\right)+\frac{2}{15}\right]$$
$$+\varepsilon_{zz}^{*}\left[\frac{\hat{K}_0}{\hat{K}_0+\frac{4}{3}\hat{\mu}_0}\left(-\frac{1}{3}\right)+\frac{\hat{\mu}_0}{\hat{K}_0+\frac{4}{3}\hat{\mu}_0}\left(-\frac{8}{45}\right)-\frac{4}{15}\right] \tag{I.51}$$
$$+\hat{\varepsilon}_{xx}^{0}\left[\frac{K_S}{a\left(\hat{K}_0+\frac{4}{3}\hat{\mu}_0\right)}\left(\frac{8}{15}\right)+\frac{K_S}{a\hat{\mu}_0}\left(-\frac{2}{15}\right)+\frac{\mu_S}{a\hat{\mu}_0}\left(-\frac{4}{15}\right)\right]$$
$$+\hat{\varepsilon}_{yy}^{0}\left[\frac{K_S}{a\left(\hat{K}_0+\frac{4}{3}\hat{\mu}_0\right)}\left(\frac{8}{15}\right)+\frac{K_S}{a\hat{\mu}_0}\left(-\frac{2}{15}\right)+\frac{\mu_S}{a\hat{\mu}_0}\left(-\frac{4}{15}\right)\right]$$
$$+\hat{\varepsilon}_{zz}^{0}\left[\frac{K_S}{a\left(\hat{K}_0+\frac{4}{3}\hat{\mu}_0\right)}\left(\frac{4}{15}\right)+\frac{K_S}{a\hat{\mu}_0}\left(\frac{4}{15}\right)+\frac{\mu_S}{a\hat{\mu}_0}\left(\frac{8}{15}\right)\right]$$

Consequently, the interface averaged $\overline{\boldsymbol{\varepsilon}}^{\lambda}$ can be written as follows

$$\overline{\boldsymbol{\varepsilon}}^{\lambda}=\hat{\mathbf{A}}:\hat{\boldsymbol{\varepsilon}}^{0}+\hat{\mathbf{B}}:\boldsymbol{\varepsilon}^{*} \tag{I.52}$$

where $\hat{\mathbf{A}}$ and $\hat{\mathbf{B}}$ are isotropic tensors ,

$$
\begin{aligned}
&\hat{\mathbf{A}} = \left(3\hat{A}_b, 2\hat{A}_s\right) \\
&\hat{A}_b = \frac{4}{9}\frac{K_S}{a\left(\hat{K}_0 + \frac{4}{3}\hat{\mu}_0\right)} \\
&\hat{A}_s = -\frac{2}{15}\frac{K_S}{a\left(\hat{K}_0 + \frac{4}{3}\hat{\mu}_0\right)} + \frac{1}{5}\frac{K_S}{a\hat{\mu}_0} + \frac{2}{5}\frac{\mu_S}{a\hat{\mu}_0} \\
&\hat{\mathbf{B}} = \left(3\hat{B}_b, 2\hat{B}_s\right) \\
&\hat{B}_b = -\frac{1}{3}\frac{\hat{K}_0}{\hat{K}_0 + \frac{4}{3}\hat{\mu}_0} \\
&\hat{B}_s = -\frac{2}{15}\frac{\hat{\mu}_0}{\hat{K}_0 + \frac{4}{3}\hat{\mu}_0} - \frac{1}{5}
\end{aligned}
\tag{I.53}
$$

Appendix II. The coefficient tensor "A"

The components of the coefficient tensor **A** for the prolate spheroid in Eq. (4.2) are

$$A_{1111} = \frac{1}{8}\frac{K_S}{\mu_0}J_1 + \frac{1}{8}\frac{\mu_S}{\mu_0}J_2 + \frac{1}{16}\frac{K_S}{M_0}J_2 + \frac{1}{16}\frac{\mu_S}{M_0}\left(2J_1 - J_2\right) \tag{II.1}$$

$$A_{1122} = \frac{1}{8}\frac{K_S}{\mu_0}J_3 - \frac{1}{8}\frac{\mu_S}{\mu_0}J_1 + \frac{1}{16}\frac{K_S}{M_0}\left(2J_1 + J_2\right) - \frac{1}{16}\frac{\mu_S}{M_0}\left(J_2 + 4J_3\right) \tag{II.2}$$

$$A_{1133} = -\frac{1}{8}\frac{K_S}{\mu_0}\left(J_1 + J_3\right) - \frac{1}{8}\frac{\mu_S}{\mu_0}\left(J_2 - J_1\right) + \frac{1}{4}\frac{K_S}{M_0}J_1 + \frac{1}{8}\frac{\mu_S}{M_0}\left(J_2 + 2J_3 - J_1\right) \tag{II.3}$$

$$A_{1212} = \frac{1}{8}\frac{K_S}{\mu_0}\left(J_1 - J_3\right) + \frac{1}{8}\frac{\mu_S}{\mu_0}\left(J_1 + J_2\right) - \frac{1}{8}\frac{K_S}{M_0}J_1 + \frac{1}{8}\frac{\mu_S}{M_0}\left(J_1 + 2J_3\right) \tag{II.4}$$

$$A_{1313} = \frac{1}{4}\frac{K_S}{\mu_0}J_4 + \frac{1}{16}\frac{\mu_S}{\mu_0}\left(11J_1 - 3J_2 + 4J_3 + 4J_4\right) - \frac{1}{8}\frac{K_S}{M_0}\left(J_2 - J_1\right) + \frac{1}{2}\frac{\mu_S}{M_0}J_5 \tag{II.5}$$

$$A_{3311} = -\frac{1}{8}\frac{K_S}{\mu_0}\left(J_1 + J_3\right) - \frac{1}{8}\frac{\mu_S}{\mu_0}\left(J_2 - J_1\right) + \frac{1}{16}\frac{K_S}{M_0}\left(5J_1 - J_2 + 4J_3 + 4J_4\right) - \frac{1}{16}\frac{\mu_S}{M_0}\left(3J_1 + J_2 + 4J_3 - 4J_4\right)$$

(II.6)

$$A_{3333} = \frac{1}{4}\frac{K_S}{\mu_0}\left(J_1 + J_3\right) + \frac{1}{4}\frac{\mu_S}{\mu_0}\left(J_2 - J_1\right) + \frac{1}{8}\frac{K_S}{M_0}\left(J_2 - J_1\right) - \frac{1}{2}\frac{\mu_S}{M_0}J_5 \tag{II.7}$$

where

$$J_1 = \frac{\pi\left[a\left(8a^4 - 2a^2b^2 + 3b^4\right)\sqrt{a^2 - b^2} + b^2\left(-8a^4 - 4a^2b^2 + 3b^4\right)\tanh^{-1}e\right]}{S\left(a^2 - b^2\right)^{5/2}} \tag{II.8}$$

$$J_2 = \frac{\pi\left[a\left(8a^4 - 42a^2b^2 + 7b^4\right)\sqrt{a^2 - b^2} + b^2\left(24a^4 - 4a^2b^2 + 7b^4\right)\tanh^{-1}e\right]}{S\left(a^2 - b^2\right)^{5/2}} \tag{II.9}$$

$$J_3 = \frac{\pi\left[a\left(-8a^4+10a^2b^2+b^4\right)\sqrt{a^2-b^2}+b^2\left(8a^4-12a^2b^2+b^4\right)\tanh^{-1}e\right]}{S\left(a^2-b^2\right)^{5/2}} \tag{II.10}$$

$$J_4 = \frac{\pi\left[4ab^2\left(-4a^2+b^2\right)\sqrt{a^2-b^2}+b^2\left(16a^4-11a^2b^2+4b^4\right)\tanh^{-1}e\right]}{S\left(a^2-b^2\right)^{5/2}} \tag{II.11}$$

$$J_5 = \frac{\pi\left[ab^2\left(-14a^2-b^2\right)\sqrt{a^2-b^2}+b^2\left(8a^4+8a^2b^2-b^4\right)\tanh^{-1}e\right]}{S\left(a^2-b^2\right)^{5/2}} \tag{II.12}$$

Further, $e=\sqrt{1-\frac{b^2}{a^2}}$ is the eccentricity, and $S=2\pi b^2\left(1+\frac{a}{be}\arcsin e\right)$ is the surface area of the prolate spheroid.

Appendix III. The coefficient tensor "B"

The components of the coefficient tensor **B** for the prolate spheroids in Eq. (4.2) are

$$B_{1111} = -\frac{1}{2} I_1 - \frac{K_0}{M_0} I_2 - \frac{1}{6} \frac{\mu_0}{M_0} \left(8 I_2 - 3 I_1 \right) \tag{III.1}$$

$$B_{1122} = \frac{1}{6} \left(4 I_2 - I_1 \right) - \frac{K_0}{M_0} I_2 + \frac{1}{6} \frac{\mu_0}{M_0} I_1 \tag{III.2}$$

$$B_{1133} = -\frac{2}{3} \left(I_2 - I_1 \right) - \frac{K_0}{M_0} I_2 - \frac{2}{3} \frac{\mu_0}{M_0} \left(2 I_2 - I_1 \right) \tag{III.3}$$

$$B_{1212} = -\frac{1}{3} \left(I_1 + 2 I_2 \right) - \frac{1}{3} \frac{\mu_0}{M_0} \left(4 I_2 - I_1 \right) \tag{III.4}$$

$$B_{1313} = -\left(I_1 + I_3 \right) + \frac{4}{3} \frac{\mu_0}{M_0} \left(I_2 - I_1 \right) \tag{III.5}$$

$$B_{3311} = -\frac{2}{3} \left(I_2 - I_1 \right) - \frac{K_0}{M_0} \left(I_1 - I_2 + I_3 \right) + \frac{2}{3} \frac{\mu_0}{M_0} I_3 \tag{III.6}$$

$$B_{3333} = \frac{4}{3} \left(I_2 - I_1 \right) - \frac{K_0}{M_0} \left(I_1 - I_2 + I_3 \right) - \frac{4}{3} \frac{\mu_0}{M_0} I_3 \tag{III.7}$$

where

$$I_1 = \frac{\pi a^2 b \left[b \left(a^2 - 10 b^2 \right) \sqrt{a^2 - b^2} + \left(25 a^4 - 24 a^2 b^2 + 8 b^4 \right) \tan^{-1} \dfrac{\sqrt{a^2 - b^2}}{b} \right]}{S \left(a^2 - b^2 \right)^{5/2}} \tag{III.8}$$

$$I_2 = \frac{\pi a^2 b \left[b \sqrt{a^2 - b^2} + \left(a^2 - 2 b^2 \right) \tan^{-1} \dfrac{\sqrt{a^2 - b^2}}{b} \right]}{S \left(a^2 - b^2 \right)^{3/2}} \tag{III.9}$$

$$I_3 = \frac{\pi b\left[b^3\left(7a^2+2b^2\right)\sqrt{a^2-b^2} + a^2\left(-24a^4+23a^2b^2-8b^4\right)\tan^{-1}\dfrac{\sqrt{a^2-b^2}}{b} \right]}{S\left(a^2-b^2\right)^{5/2}} \qquad \text{(III.10)}$$